

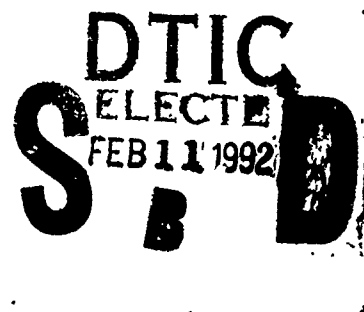
AD-A245 966



NAVAL POSTGRADUATE SCHOOL

Monterey, California

2



THESIS

Applications of Passive Microwave Satellite Data for Arctic Sea Ice Studies

by

William Archer Wright

December 1991

Thesis Co-advisors:

Jeffery A. Nystuen
Robert H. Bourke

Approved for public release; distribution is unlimited.

92-03263



92 2 10 11 1

Unclassified

SECURITY CLASSIFICATION OF THIS PAGE

REPORT DOCUMENTATION PAGE

1a. REPORT SECURITY CLASSIFICATION Unclassified			1b. RESTRICTIVE MARKINGS		
2a. SECURITY CLASSIFICATION AUTHORITY			3. DISTRIBUTION/AVAILABILITY OF REPORT Approved for public release; distribution is unlimited.		
2b. DCLASSIFICATION/DOWNGRADING SCHEDULE					
4. PERFORMING ORGANIZATION REPORT NUMBER(S)			5. MONITORING ORGANIZATION REPORT NUMBER(S)		
6a. NAME OF PERFORMING ORGANIZATION Naval Postgraduate School		6b. OFFICE SYMBOL (If Applicable) 35	7a. NAME OF MONITORING ORGANIZATION Naval Postgraduate School		
6c. ADDRESS (city, state, and ZIP code) Monterey, CA 93943-5000			7b. ADDRESS (city, state, and ZIP code) Monterey, CA 93943-5000		
8a. NAME OF FUNDING/SPONSORING ORGANIZATION		8b. OFFICE SYMBOL (If Applicable)	9. PROCUREMENT INSTRUMENT IDENTIFICATION NUMBER		
8c. ADDRESS (city, state, and ZIP code)			10. SOURCE OF FUNDING NUMBERS		
			PROGRAM ELEMENT NO.	PROJECT NO.	TASK NO.
			WORK UNIT ACCESSION NO.		
11. TITLE (Include Security Classification) Applications of Passive Microwave Satellite Data for Arctic Sea Ice Studies					
12. PERSONAL AUTHOR(S) Wright, William Archer					
13a. TYPE OF REPORT Master's Thesis		13b. TIME COVERED FROM TO		14. DATE OF REPORT (year, month, day) December 1991	
				15. PAGE COUNT 127	
16. SUPPLEMENTARY NOTATION The views expressed in this thesis are those of the author and do not reflect the official policy or position of the Department of Defence or the U.S. Government.					
17. COSATI CODES			18. SUBJECT TERMS (continue on reverse if necessary and identify by block number)		
FIELD	GROUP	SUBGROUP	Passive Microwave, Arctic Sea Ice, SSM/I, Yermak Plateau, Diurnal Tidal Currents, Ice Drift, Feature Tracking		
19. ABSTRACT (Continue on reverse if necessary and identify by block number)					
<p>Passive microwave satellite data provides all-weather, continuous observations of the polar ice cover. Multichannel radiometer data sets extending back to 1978 are readily available and distributed on CD-ROM media. Current algorithms can extract information on ice cover, concentration and type. Two applications of these data sets for polar studies are explored: 1) the possible detection of altered ice morphology due to anomalous tidal currents in the Yermak Plateau region; and 2) the tracking of multiyear ice features to infer ice motion.</p> <p>No evidence of altered ice morphology in the Yermak Plateau region was detected. Either the reported anomalous currents do not affect ice morphology or the limitations inherent to passive microwave imagery (poor spatial resolution) prevent detection. On the other hand, distinct multiyear ice features are observed to move in the direction of mean ice flow and are well correlated with the motion of nearby data buoys. Short term ice motion vectors are unreliable because of the low spatial resolution of the passive microwave data. However, long term averages are indicative of ice flow trajectories and can be used, for example, to increase our knowledge of the interannual variability of heat and salinity budgets in specific regions, including Fram Strait, the principal outflow region of the arctic basin.</p>					
20. DISTRIBUTION/AVAILABILITY OF ABSTRACT <input checked="" type="checkbox"/> UNCLASSIFIED/UNLIMITED <input type="checkbox"/> SAME AS RPT. <input type="checkbox"/> DTIC USERS			21. ABSTRACT SECURITY CLASSIFICATION Unclassified		
22a. NAME OF RESPONSIBLE INDIVIDUAL Jeffery A. Nystuen			22b. TELEPHONE (Include Area Code) (408) 646-2917		22c. OFFICE SYMBOL OC/Ny

DD FORM 1473, 84 MAR

83 APR edition may be used until exhausted

SECURITY CLASSIFICATION OF THIS PAGE

All other editions are obsolete

Unclassified

Approved for public release; distribution is unlimited.

Applications of Passive Microwave Satellite Data to Arctic Sea Ice Studies

by

William A. Wright, III
Lieutenant, United States Navy
B.S., U. S. Naval Academy, 1982

Submitted in partial fulfillment of the requirements for
the degree of

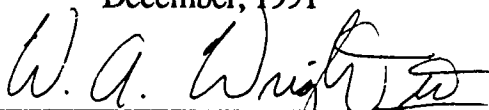
MASTER OF SCIENCE IN METEOROLOGY AND PHYSICAL
OCEANOGRAPHY

from the

NAVAL POSTGRADUATE SCHOOL

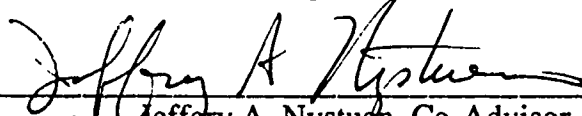
December, 1991

Author:

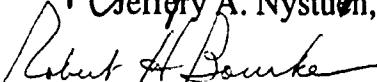


William A. Wright, III

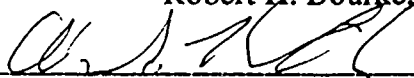
Approved by:



Jeffery A. Nystuen, Co-Advisor



Robert H. Bourke, Co-Advisor



Alan S. Thorndike, Second Reader

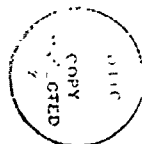


Curtis A. Collins, Chairman, Department of Oceanography

ABSTRACT

Passive microwave satellite data provides all-weather, continuous observations of the polar ice cover. Multichannel radiometer data sets extending back to 1978 are readily available and distributed on CD-ROM media. Current algorithms can extract information on ice cover, concentration and type. Two applications of these data sets for polar studies are explored: 1) the possible detection of altered ice morphology due to anomalous tidal currents in the Yermak Plateau region; and 2) the tracking of multiyear ice features to infer ice motion.

No evidence of altered ice morphology in the Yermak Plateau region was detected. Either the reported anomalous currents do not affect ice morphology or the limitations inherent to passive microwave imagery (poor spatial resolution) prevent detection. On the other hand, distinct multiyear ice features are observed to move in the direction of mean ice flow and are well correlated with the motion of nearby data buoys. Short term ice motion vectors are unreliable because of the low spatial resolution of the passive microwave data. However, long term averages are indicative of ice flow trajectories and can be used, for example, to increase our knowledge of the interannual variability of heat and salinity budgets in specific regions, including Fram Strait, the principal outflow region of the arctic basin.



Accession For	
NTIS GRA&I	<input checked="checked" type="checkbox"/>
DTIC TAB	<input type="checkbox"/>
Unannounced	<input type="checkbox"/>
Justification	
By	
Distribution/	
Availability Codes	
Dist	Avail and/or Special
A-1	

TABLE OF CONTENTS

I	INTRODUCTION	1
II	BACKGROUND	3
	A. THE SSM/I	3
	B. SEA ICE RADIATION CHARACTERISTICS.....	5
	1. Physical Properties	5
	2. Radiative Properties.....	6
	3. Atmospheric Effects.....	9
	C. SEA ICE CONCENTRATION ALGORITHM	9
	1. Physical Model	9
	2. Multichannel Algorithm.....	11
	D. DATA SOURCES.....	14
	1. NSIDC CD-ROMs.....	14
	2. Ice Buoy Tracks	15
III	CASE STUDY: ANOMALOUS DIURNAL CURRENTS ON THE YERMAK PLATEAU	21
	A. BACKGROUND	21
	1. The Yermak Plateau	21
	2. Regional Tides.....	21
	3. Observations.....	22
	4. Analysis	23
	5. Effects on Sea Ice Characteristics.....	24
	B. METHODOLOGY.....	25
	C. RESULTS.....	26
	a. Ice Concentration	26
	b. Gradient Ratio	27
	D. CONCLUSIONS.....	28
IV.	CASE STUDY: ICE MOTION ANALYSIS.....	46
	A. BACKGROUND	46

1. General Ice Flow	46
2. Feature Tracking	47
B. METHODOLOGY.....	49
1. Satellite Images	49
2. Feature Tracking	50
3. Feature Selection.....	52
4. Errors.....	54
C. RESULTS.....	60
1. Ice Trajectories.....	60
2. Velocity Comparisons.....	61
3. Position Error	53
D. DISCUSSION.....	65
E. CONCLUSIONS.....	67
V. CONCLUSIONS AND RECOMMENDATIONS.....	85
APPENDIX A	88
REFERENCES.....	113
INITIAL DISTRIBUTION LIST	117

LIST OF FIGURES

Figure 1	Schematic illustration of differences between (a) first year ice and (b) multiyear ice (after Comiso, 1983).....	16
Figure 2	Emissivities of calm seawater, multiyear ice and first year ice as a function of frequency for horizontal and vertical polarizations (modified from Svendsen et al., 1983).	17
Figure 3	Illustration of the four terms in the radiation model.	18
Figure 4	Multispectral analysis of brightness temperatures (from Comiso, 1983).	19
Figure 5	SSM/I north polar grid (from NSIDC, 1990).	20
Figure 6	Bathymetric chart of the Yermak Plateau (from Hoffman, 1990).	30
Figure 7	Leading semi-diurnal (M2) ocean tide (from Schwiderski, 1986).	31
Figure 8	Leading diurnal (K1) ocean tide (from Schwiderski, 1986).....	32
Figure 9	Absolute current velocities along the FRAM IV track at 104 m (from Hunkins, 1986).	33
Figure 10	Kinetic energy spectra for the cross slope velocity component from FRAM IV at 303 m (from Hunkins, 1986).....	34
Figure 11	Peak amplitudes of kinetic energy for the K1 and M2 frequencies as a function of current axis orientation for FRAM IV at 303 m (from Hunkins, 1986).	35
Figure 12	Diurnal looping of ARCTEMIZ 86 drifter buoys (from Hoffman, 1990).	36
Figure 13	Yermak Plateau test and control areas.	37
Figure 14	Total ice concentrations, 1 May - 15 October 1988: (a) North control, (b) Slope and (c) South control.....	38
Figure 15	Yermak slope ice concentrations, 1 May - 15 October 1988.	39
Figure 16	Percent concentration differences (1 May - 15 October 1988): (a) North control minus Slope, (b) South control minus Slope.....	40
Figure 17	Autocorrelation of slope region ice concentrations.....	41
Figure 18	Ice concentration spectra (1 May - 15 October 1988): (a) North Control, (b) Slope, and (c) South control.....	43
Figure 19	Ice concentration spectra (1 May - 15 October 1988): (a) North - Slope difference and (b) Slope - South difference.....	43

Figure 20	Gradient ratios for Slope and Control areas, 13 January - 30 April 1988.....	44
Figure 21	Slope - Upstream gradient ratio difference, 1 February - 30 April 1988.....	45
Figure 22	Field of mean ice motion (from Colony and Thorndike, 1984).....	69
Figure 23	Average sea ice drift showing the two components of the Transpolar Drift Stream (from Polarstern Scientific Party. 1988).	70
Figure 24a	Contour plots showing advection of multiyear ice feature along the east Greenland coast. Images from 2 and 5 March, 1988.	71
Figure 24b	Same as Figure 24a except images are from 8 and 11 March, 1988..	72
Figure 24c	Same as Figure 24a except images are from 14 and 17 March, 1988.....	73
Figure 25a	Pixel values for multiyear ice contour plot shown in Figure 24a. Circled value is tiepoint registration location.....	74
Figure 25b	Pixel values for multiyear ice contour plot shown in Figure 24b. Circled value is tiepoint registration location.....	75
Figure 25c	Pixel values for multiyear ice contour plot shown in Figure 24c. Circled value is tiepoint registration location.....	76
Figure 26	Ice velocities for Fram Strait feature (1 February - 22 April, 1988). ...	77
Figure 27	Ice trajectories: Fram Strait feature and Buoy 7001 (1 February - 22 April, 1988).	78
Figure 28	Ice trajectories: Franz Josef Land feature and Buoy 1790 (1 February. - 14 March, 1988).	79
Figure 29	Ice trajectories: East Siberia Sea feature and Buoy 1896 (1 - 25 April, 1988).	80
Figure 30	Ice trajectories: Severnaya Zemlya feature and Buoy 7048 (1 February - 28 April, 1988).	81
Figure 31	Ice trajectories: Central Arctic feature and Buoy 3288 (1 January - 31 March, 1988).	82
Figure 32	Franz Josef Land and Buoy 1790 velocity comparison.....	83
Figure 33	East Siberian Sea and Buoy 1896 velocity comparison.....	83
Figure 34	Severnaya Zemlya and Buoy 7048 velocity comparison.	84
Figure 35	Central Arctic and Buoy 3288 velocity comparison.	84

LIST OF TABLES

TABLE 1	SSM/I FREQUENCIES.....	4
TABLE 2	EMISSIONS AT 19.35 AND 37 GHZ	13
TABLE 3	CORRELATION MATRIX FOR YERMAK SLOPE PIXELS.....	27
TABLE 4	MYI FEATURE - BUOY DATA.....	54
TABLE 5	SUMMARY OF MAXIMUM ERRORS.....	57
TABLE 6	MYI FEATURE - BUOY CORRELATIONS.....	62

I. INTRODUCTION

All-weather, continuous observations of the arctic ice cover are important for commercial and naval operations and for scientific studies such as global climate change. However, such observations are generally difficult to obtain. In-situ measurements from ice camps and ships are expensive to acquire and spatially limited. Aircraft measurements can expand the areal coverage, but asset and resource limitations prevent continuous large-scale monitoring of the ice pack. Satellite platforms are the only practical means of providing continuous coverage. Of the passive sensing methods, only microwave emissions penetrate the clouds and darkness that shield much of the arctic ice from visual and infrared observations. Passive satellite microwave data are operationally available from Special Sensor Microwave/Imager (SSM/I) sensors on the Defense Meteorological Satellite Program (DMSP) series satellites (Hollinger et al., 1987). Historical data are also available to researchers on CD-ROM distributed by the National Snow and Ice Data Center (NSIDC).

The objectives of this study are to explore the use of passive microwave satellite measurements for arctic sea ice studies. Two applications are examined:

- The detection of altered ice morphology due to anomalous diurnal tidal currents observed over the Yermak Plateau. If successful, this technique can be applied in other polar regions to expand our knowledge of the local tidal structure and its effect on sea ice cover.
- Determination of ice flow by tracking the movement of floes exhibiting different morphologies from the surrounding ice field.

This can augment the Arctic Buoy Program and increase our understanding of ice dynamics.

Chapter II presents background material on the SSM/I, data sources and sea ice microwave radiation characteristics. Determination of sea ice concentrations from passive microwave data are also discussed. Chapter III examines the anomalous diurnal currents observed over the Yermak Plateau. Previous observations and models prove the existence and explain the physics behind these currents. The effect of these currents on the ice cover is examined through passive microwave emissions. Chapter IV shows how ice features can be tracked to infer general ice drift patterns in the arctic. When combined with other data, this technique can help researchers understand ice and salinity budgets in the polar region. Chapter V summarizes the results and closes with a discussion of further research that could be attempted using these data.

II. BACKGROUND

A. THE SSM/I

The SSM/I is flown on the Defense Meteorological Satellite Program (DMSP) block 5D-2 F8 satellite, launched on June 19, 1987. It is in circular sun-synchronous near-polar orbit at an altitude of approximately 833 km, an inclination of 98.8° and a period of 102 minutes. This produces 14.1 full orbit revolutions per day with a 0613 local ascending node equatorial crossing. The SSM/I's conical scan covers a 1400 km swath which provides 24 hour near-global coverage. The orbit inclination precludes coverage of a 280 km radius region centered on each pole extending to about 87.5°N . Equatorial regions require 72 hours for full coverage, however overlapping orbits provide full daily coverage poleward of 45°N . Hollinger et al. (1990) provide a good discussion of SSM/I operating characteristics.

The SSM/I uses four frequencies to measure seven channels of linearly polarized radiation as shown in Table 1. Footprint resolution increases with increasing frequency. Unfortunately, the high resolution 85 GHz vertically polarized (85V) channel was damaged when the satellite overheated in the winter of 1987. The channel was useless by the end of January 1989 (Hollinger et al., 1990). The National Snow and Ice Data Center (NSIDC) recently reported that the 85 GHz horizontally polarized (85H) channel is becoming increasingly unreliable and is basically useless (Taylor, 1990). Poe and Conway (1990) reported the current SSM/I geo-location error to be approximately 10-15 km.

NSIDC applies a correction algorithm that reduces this error to 8 km (NSIDC, 1990).

TABLE 1: SSM/I FREQUENCIES

Channel	Frequency (GHz)	Wavelength (cm)	Polarization	Resolution (km)
1	19.35	1.55	Vertical	56
2	19.35	1.55	Horizontal	56
3	22.235	1.35	Vertical	45
4	37.0	0.81	Vertical	33
5	37.0	0.81	Horizontal	33
6	85.5	0.35	Vertical	14
7	85.5	0.35	Horizontal	14

SSM/I data are transmitted to Telemetry and Data Relay Stations on each orbit. These data are then relayed via satellite to Navy and Air Force processing centers which produce near real time global maps of sea ice location, age, type and other environmental parameters. Raw data are also continually broadcast to Air Force and Navy tactical units positioned within the orbital swath of the satellite that are equipped with SMQ-11 satellite receivers.

Data record files are created from raw radiometer measurements. Temperature data records (TDRs) are antenna temperatures which are calibrated each scan using a 300° K black-body radiator and the 3° K cosmic radiation as reference temperatures. An antenna pattern correction is applied to the TDRs to correct for energy received in the sidelobes, cross-polarization coupling and feedhorn spillover loss (NSIDC, 1990). These main beam brightness temperatures are placed in sensor data record (SDR) files. Environmental parameters are determined by applying appropriate algorithms to the SDRs and are stored in environmental data records (EDRs). The primary archiver of SSM/I data in orbital format is the NOAA/National Environmental Satellite, Data, and Information Service, Satellite Data Services Division (NOAA/NESDIS/SDSD). TDRs, SDRs and EDRs are also forwarded to the Naval Research Laboratory for archival.

B. SEA ICE RADIATION CHARACTERISTICS

Sea ice is a complex material. A good comprehensive overview of both its physical and microwave radiation characteristics can be found in Parkinson et al. (1987). The following is a general discussion of these properties.

1. Physical Properties

Sea ice covers approximately seven percent of the world's oceans. It is inhomogeneous, anisotropic and never in equilibrium. Sea ice can simultaneously contain all three phases of matter: solid ice, liquid brine pockets and air cavities. The fractions of the constituent phases change over time. New ice is thinner and saltier than first year ice, which transforms after a melt cycle (summer season) into fresher, thicker and less dense multiyear ice containing numerous air pockets. Ice can be covered with a layer of dry or wet snow of varying thickness; summer

melting forms ponds of liquid water over the ice sheet. Figure 1 shows the different physical characteristics of first and multiyear ice.

The ice composition is initially determined by environmental factors at the time it is formed. These factors include air temperature, wind speed, ocean currents, near surface salinity and weather (Weeks, 1981). The ice composition changes continuously due to weather, ice advection and fracturing or ridging effects. Warmer summer temperatures are especially important as melt water percolates through the ice and brine pockets are flushed.

2. Radiative Properties

The radiative properties of sea ice are determined by the emissivity differences between ice and water. Emissivity is the ratio of emittance ($\text{J m}^{-2} \text{s}^{-1}$) per unit wavelength to that of a blackbody at the same temperature. The Rayleigh-Jeans approximation (linear relationship between emittance and temperature) applies at microwave wavelengths. The emissivity (ϵ) of a substance can be expressed as:

$$\epsilon = \frac{T_e}{T_{\text{sfc}}} \quad (1)$$

where T_e is the radiated microwave brightness temperature, proportional to the emittance, and T_{sfc} is the physical temperature of the substance. The SSM/I radiometer senses T_B , the brightness temperature at the satellite which is related to T_e after attenuation and contamination by atmospheric effects are considered.

Brightness temperatures can be used to calculate ice concentrations and differentiate between open water, first year ice and multiyear ice based on emissivity variations of the substances. To a lesser extent, snow and water-

covered ice can also be observed. Figure 2 summarizes the emissivity differences between sea water, first year ice and multiyear ice as a function of polarized frequency.

The ice composition controls the dielectric properties that influence the emissivity of the ice. Following Comiso (1983), the principal difference between sea ice and freshwater ice are brine inclusions in the former. These brine pockets are small, typically 3-5 mm by 0.25 mm (Vant et al., 1978). The brine content of sea ice depends on freezing conditions and subsequent temperature changes and varies from 16 psu for first year ice to less than 1 psu for multiyear ice. The liquid brine effects the dielectric property that determines emissivity and the skin depth, which is the depth from which most of the observed radiation emanates. In saline ice the skin depth is on the order of the radiation wavelength. For desalinated ice this depth can be many wavelengths (Gloersen et al., 1973).

The fundamental difference between first year and multiyear ice is the presence of brine pockets in the former and their replacement in the freeboard layer by air in the latter. Because of the small skin depth, microwave emissions from the more saline first year ice emanate from the snow/ice interface; emissions from fresher multiyear ice emanate from a thicker ice layer and are subject to scattering by the air pockets. This scattering reduces the net radiation from the ice surface thus lowering the brightness temperature (Comiso, 1983).

Snow cover also effects microwave radiation. Snow insulates the ice from the atmosphere, leading to warmer ice from oceanic heat conduction and therefore slightly higher brightness temperatures. This may be compensated by the scattering effect of snow ice crystals, especially at higher frequencies. Emissions from the crystals are negligible (Comiso et al., 1982). During the

summer melt season, however, each crystal is surrounded by a thin layer of water. This wet snow cover becomes the primary radiation source, significantly lowering brightness temperatures due to water's low emissivity. This effect makes it nearly impossible to discriminate wet snow-covered multiyear ice from first year ice in the summer.

Ice thickness also influences brightness temperatures. At microwave frequencies, thin ice (radiation wavelength or less) is contaminated by the coldly radiating water below, lowering the brightness temperature. This may be compensated by the higher salinity and warmer physical temperature of the thin ice versus the relatively fresher and colder thick ice.

Melt ponds are formed by solar heating of the ice cover and are characterized by thin layers of water scattered among solid ice regions. The size and depth of the ponds depend on the incident solar flux, ice salinity and ice roughness (Goroch and Fett, 1990). If the thin water layer is thicker than the skin depth of the radiation (typically a few mm to one cm), the radiation is emitted primarily by the liquid and has a much colder brightness temperature than the ice. For thinner layers the underlying ice will contribute some radiation, raising the brightness temperature. The variation of brightness temperature depends on the layer depth and the emission frequency. For depths on the order of a few millimeters the 19 and 22 GHz channels will be unaffected (Goroch and Fett, 1990). As the frequency increases, contamination by the water layer also increases. The total effect on brightness temperature is a function of areal extent within the radiometer footprint and melt pond depth.

Other factors affecting microwave emissivities include the physical temperature of ice and undulations caused by ridging and refreezing of melt

ponds. As with liquid melt ponds, these conditions vary spatially and temporally and could cause observable changes in ice emissivity.

3. Atmospheric Effects

Important atmospheric constituents which affect microwave radiation are water vapor, oxygen and liquid water content. Seasonal climatological constants developed from physical models or observations are generally used in algorithms to quantify their cumulative effect on brightness temperatures.

Interaction with non-precipitating clouds in the arctic region is negligible due to the small size of the droplets compared with the microwave wavelengths (Comiso, 1983). Liquid precipitation, however, can contaminate brightness temperatures. Operational algorithms usually flag rain-contaminated radiances for rejection.

Although the arctic regions have low humidities, absorption by water vapor can effect remotely sensed emissions. For the SSM/I only the 22 and 85.5 GHz channels are significantly effected by water vapor absorption (Hollinger et al, 1987). Neither channel is currently used in ice studies, although the higher resolution offered by operational 85.5 GHz channels in future DMSP satellites will be tempting.

The atmospheric oxygen distribution is well known and constant. Absorption effects are included in seasonal climatological constants used in ice concentration algorithms.

C. SEA ICE CONCENTRATION ALGORITHM

1. Physical Model

A simple radiative model expressing the radiation sensed at satellite height (T_B) is presented in Svendsen et al. (1983). Surface and atmospheric

effects are included, plus a minor free space contribution. The model is composed of four terms (see Figure 3): radiation from the surface as seen through the atmosphere (A); upwelled radiation from the atmosphere (B); downwelled atmospheric radiation reflected at the surface (C); and free space radiation reflected by the surface (D).

$$T_B = \underset{(A)}{\epsilon_{sfc} T_{sfc} (1 - \tau_a)} + \underset{(B)}{\delta T_a \tau_a} + \underset{(C)}{(1 - \epsilon_{sfc}) \delta T_a \tau_a (1 - \tau_a)} + \underset{(D)}{(1 - \epsilon_{sfc}) T_{sp}} \quad (2)$$

τ_a is the optical depth, T_{sp} is the free space temperature and δT_a is the weighted average atmospheric temperature in the lower troposphere. Since the optical depth is small, the extinction exponential ($e^{-\tau_a}$) is approximated by $1 - \tau_a$. Atmospheric absorption of free space radiation is neglected.

From equation (1) the emitted brightness temperature (T_e) is dependent only on the physical temperature of the emitter (T_{sfc}) and its emissivity (ϵ_{sfc}). By substituting T_e/T_{sfc} for ϵ_{sfc} in equation (2), T_e can be computed if τ_a and δT_a are known, and if T_{sfc} is inferred from δT_a .

Three components contribute to T_e : sea water, first year ice and multiyear ice. The sum of the fractional components of each (C_w , C_f and C_m , respectively) add up to 1:

$$1 = C_m + C_f + C_w \quad (3)$$

The emitted brightness temperature is the sum of the individual components, weighted by the concentrations:

$$T_e = \epsilon_{sfc} T_{sfc} = C_m \epsilon_m T_{ice} + C_f \epsilon_f T_{ice} + C_w \epsilon_w (272) \quad (4)$$

where water temperature is assumed to be 272° K and ϵ_f , ϵ_m and ϵ_w are the emissivities of first year ice, multiyear ice and seawater, respectively. T_{ice} in equation (4) is determined by assuming a linear relationship between the atmospheric surface temperature (T_a) and the water temperature:

$$T_{ice} = \alpha T_a + (1-\alpha)(272) \quad (5)$$

where α is an observationally determined constant (≈ 0.4 from Svendsen et al., 1983).

Fractional concentrations can be computed from equations (1) - (5) using two radiometer channels. Sources of error include approximations of optical depth, ice temperature, atmospheric temperature weighting factor, atmospheric surface temperatures and assuming constant emissivities for first and multiyear ice. Svendsen et al. (1983) compared aircraft radiometric measurements with Nimbus 7 radiometer measurements using this technique with in-situ temperature observations and determined accuracies to be $\pm 3\%$ of total ice concentration and $\pm 10\%$ for multiyear ice concentration with a spatial resolution of 90 km.

2. Multichannel Algorithm

a. *Multispectral Analysis*

Comiso (1983) applied a multi-spectral technique that exploits the variation of emissivity with frequency for sea water and various ice types to

distinguish between various first and multiyear ice and open water. Figure 4 shows three distinct brightness temperature clusters that, when geo-located, correspond to first year ice, a first/multiyear ice mixture and open ocean conditions. The line that connects the first year cluster with the open ocean is interpreted as varying ice concentrations. Because the skin depth is frequency dependent, the grouping beneath the first year ice is theorized to be thin ice, where cold contamination from sea water is observed in the lower (deeper penetrating) frequency. The larger spread of emissivities and brightness temperatures in the 37V channel reflects the greater sensitivity of 37 GHz radiation to near-surface effects due to its smaller skin depth.

b. Polarization/Gradient Ratios

Cavelieri et al. (1984) used polarization ratios (PR) for a single frequency and spectral gradient ratios (GR) between two frequencies to estimate ice concentrations and fractions. PR and GR are defined as follows:

$$PR = \frac{T_{Bv}(f_1) - T_{Bh}(f_1)}{T_{Bv}(f_1) + T_{Bh}(f_1)} \quad (6)$$

$$GR = \frac{T_{Bv}(f_1) - T_{Bv}(f_2)}{T_{Bv}(f_1) + T_{Bv}(f_2)} \quad (7)$$

where T_{Bv} and T_{Bh} are brightness temperatures for vertical and horizontal polarizations respectively and f_1 and f_2 are separate frequencies. Table 2 shows PRs and GRs for sea ice and water emissivities at the two SSM/I frequencies (37.0 and 19.35 GHz) used to calculate ice concentrations and fractions. Note that PR is much greater over the open ocean than over sea ice. Thus PR is a good

water/ice discriminator and can be used to estimate ice concentrations. GR depends on ice type and is affected by season. Ice types are determined by the sign of GR: positive over the open ocean, negative over multiyear ice and near zero over first year ice (Parkinson and Cavalieri, 1989).

TABLE 2: EMISSIVITIES AT 19.35 AND 37 GHZ

Ice Type	First Year Thin Ice		First Year Ice		Multiyear Ice		Calm Sea Water	
	V	H	V	H	V	H	V	H
Frequency (GHz)								
19.35	0.96	0.78	0.97	0.84	0.86	0.73	0.60	0.33
37.0	0.96	0.87	0.97	0.95	0.69	0.64	0.70	0.40
Polarization Ratio (37V - 37H)	0.09		0.02		0.05		0.30	
Gradient Ratio (37V - 19V)	0.00		0.00		-0.17		0.10	

Cavalieri et al. (1984) describe how these ratios are used to calculate total and multiyear ice concentrations and the physical temperature of the sea surface. They conclude that the precision of the calculated concentrations ranges from 5 - 9 % and the precision of the calculated multiyear ice fractions vary from 13 - 25 %. A caveat on the ice fraction calculation is that

first and multiyear ice can not be discriminated during the summer season because the general surface melt conditions mask the distinguishing properties of the two ice types. A non-iterative version of this method has been adopted by the NASA Sea Ice Algorithm Working Group and is used by the NSIDC (NSIDC, 1990).

D. DATA SOURCES

1. NSIDC CD-ROMs

NSIDC distributes SSM/I brightness temperatures on CD-ROM disks for both arctic and antarctic regions. A continuous record is currently available from 9 July 1987 - 31 December 1989. Earlier SMMR data are available in the same format from 1978-1987. Subsequent SSM/I data are in production for CD-ROM distribution. The data include all SSM/I channels with 85 GHz data gridded at 12.5 km resolution and 19, 22 and 37 GHz data gridded at 25 km resolution. Added features are land masks and coast outlines that provide geographic reference points on the imagery. The data are obtained from NOAA/NESDIS/SDSD. Fleet Numerical Oceanography Center produces the original TDR files from the raw satellite data as part of their operational data processing. The TDRs are transferred to NOAA/NESDIS/SDSD and then to NSIDC. At NSIDC the TDRs are examined for bad data values and a geolocation correction is applied. The antenna temperatures are then converted to brightness temperatures.

Swath data from each channel are mapped onto the appropriate grid by converting the geodetic latitudes and longitudes at the center of each observation footprint into map grid coordinates. Brightness temperatures are summed in each grid cell over a 24 hour period and then divided by the number

of observations. The resulting data fields are daily averaged mosaics of each polar region.

The data are mapped onto polar stereographic projections with the grid tangent to the earth at 70° latitude rather than at the poles. This increases the distortion at the poles by 3% but is offset by nearly true projections in the marginal ice zones. Figure 5 shows the area of coverage for the Northern Hemisphere.

2. Ice Buoy Tracks

The Arctic Buoy Program has been operating since 1979. Objectives of the program are to provide surface atmospheric pressure measurements over the arctic basin and to define the large scale field of sea ice motion (Thorndike and Colony, 1980). Buoys are parachuted from C-130 aircraft at designated locations. Each buoy transmits pressure and air temperature information to a satellite at one minute intervals. This information is only received when the satellite is within the radio field of view. The data are retransmitted to a ground station, decoded and filtered, and forwarded to the Polar Science Center at the University of Washington. Thorndike and Colony (1980) examined the locational record of one buoy and reported the positional accuracy, as measured through the Doppler shift of the buoy signal received by the satellite, to be within 300 m for two thirds of the reported positions. Very few fixes were reported with errors greater than 10 km and these can be easily removed from the record by careful editing.

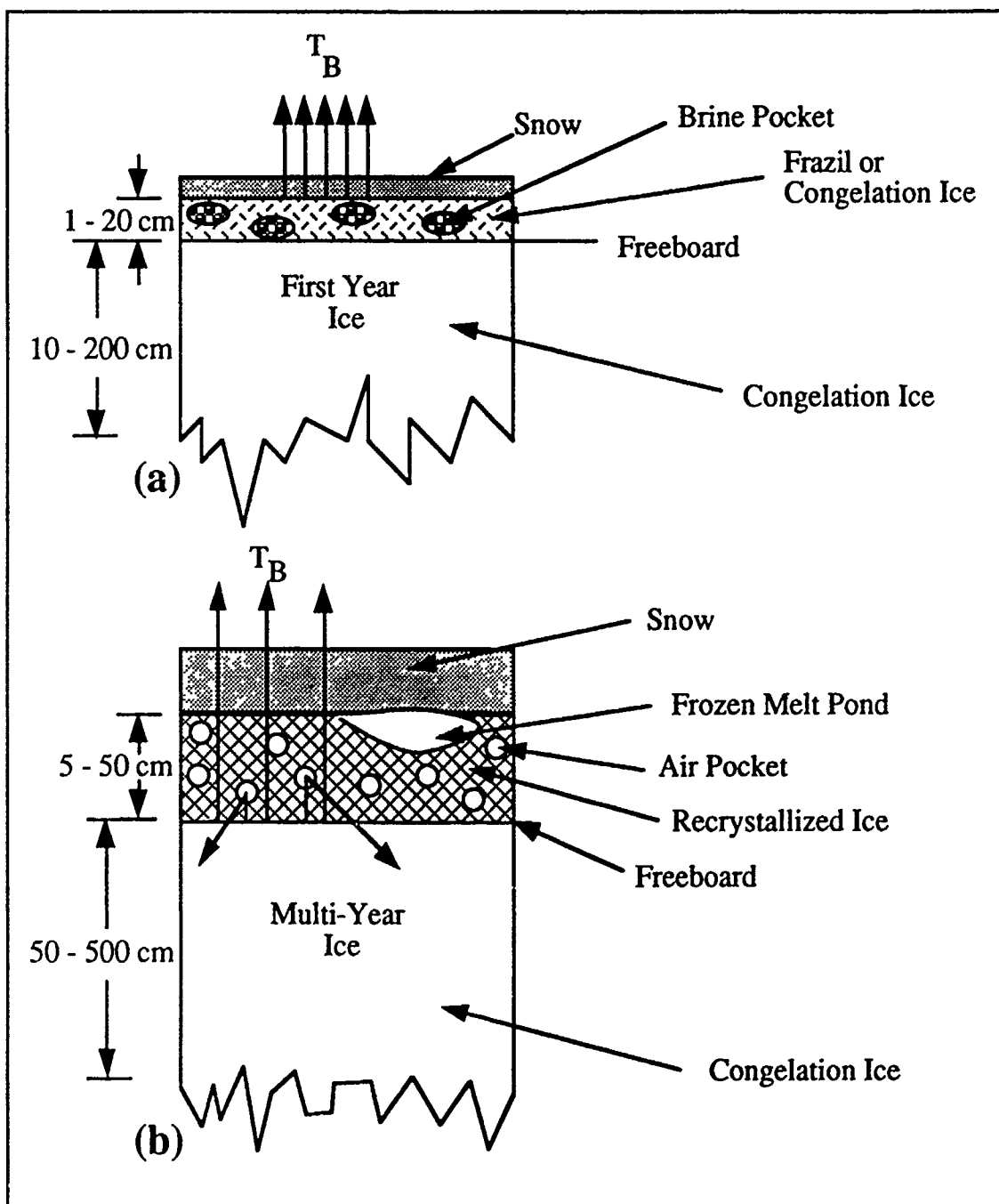


Figure 1 Schematic illustration of differences between (a) first year ice and (b) multiyear ice (after Comiso, 1983).

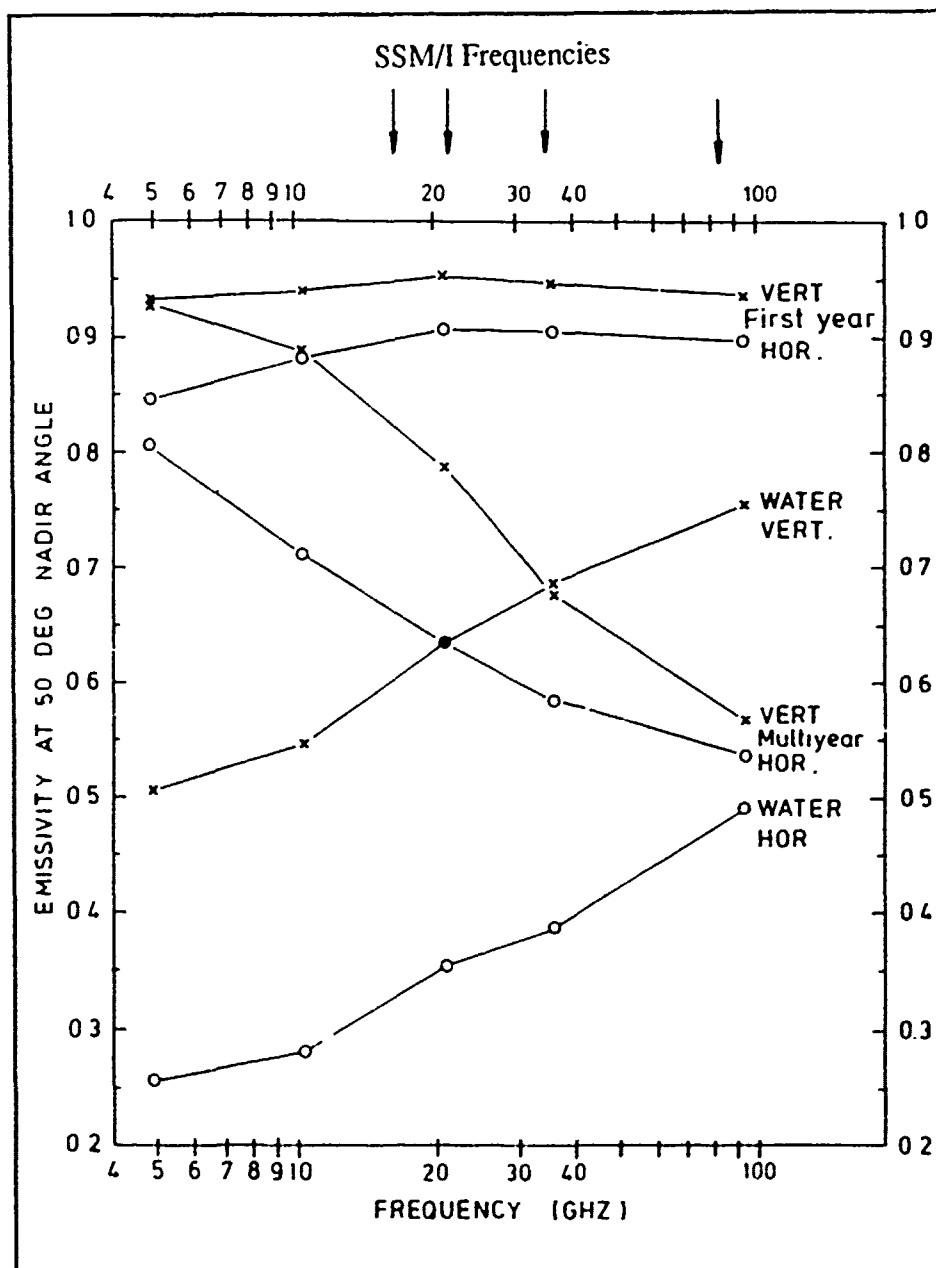


Figure 2 Emissivities of calm seawater, multiyear ice and first year ice as a function of frequency for horizontal and vertical polarizations (modified from Svendsen et al., 1983).

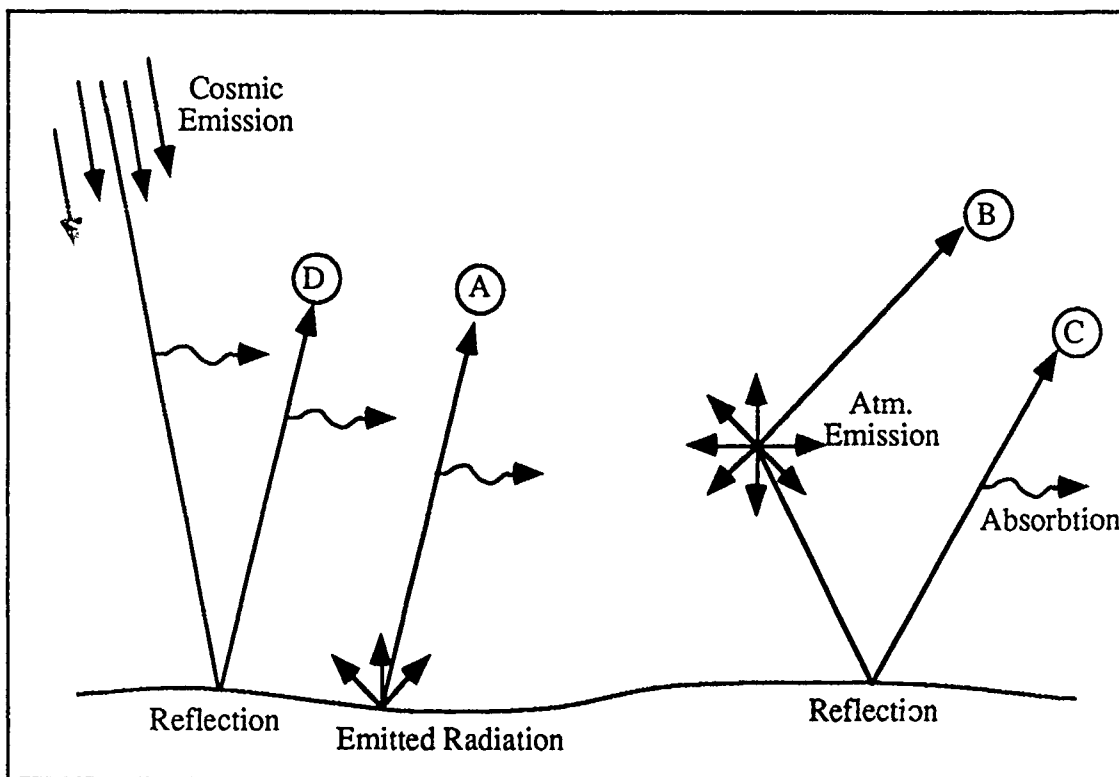


Figure 3 Illustration of the four terms in the radiation model.

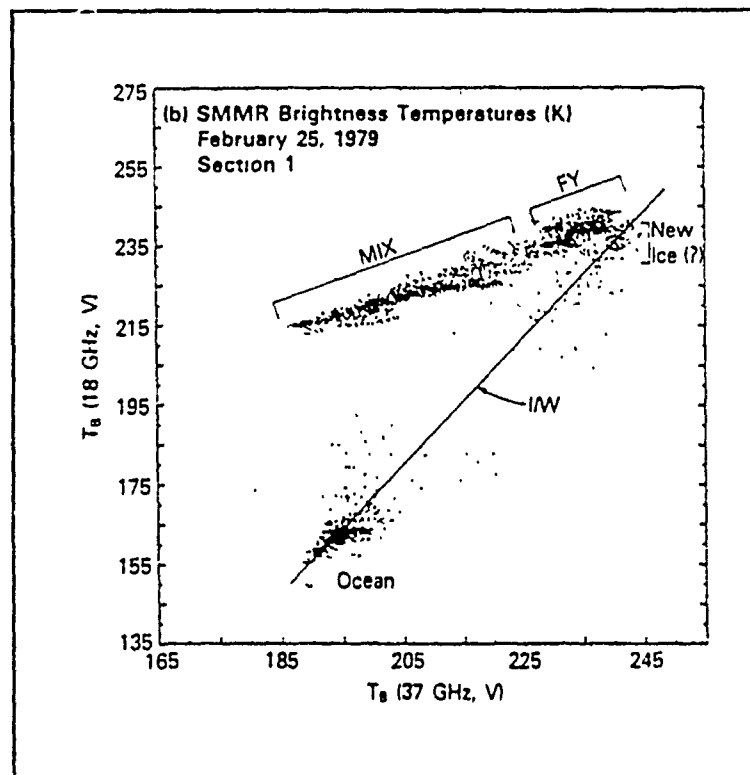


Figure 4 Multispectral analysis of brightness temperatures (from Comiso, 1983).

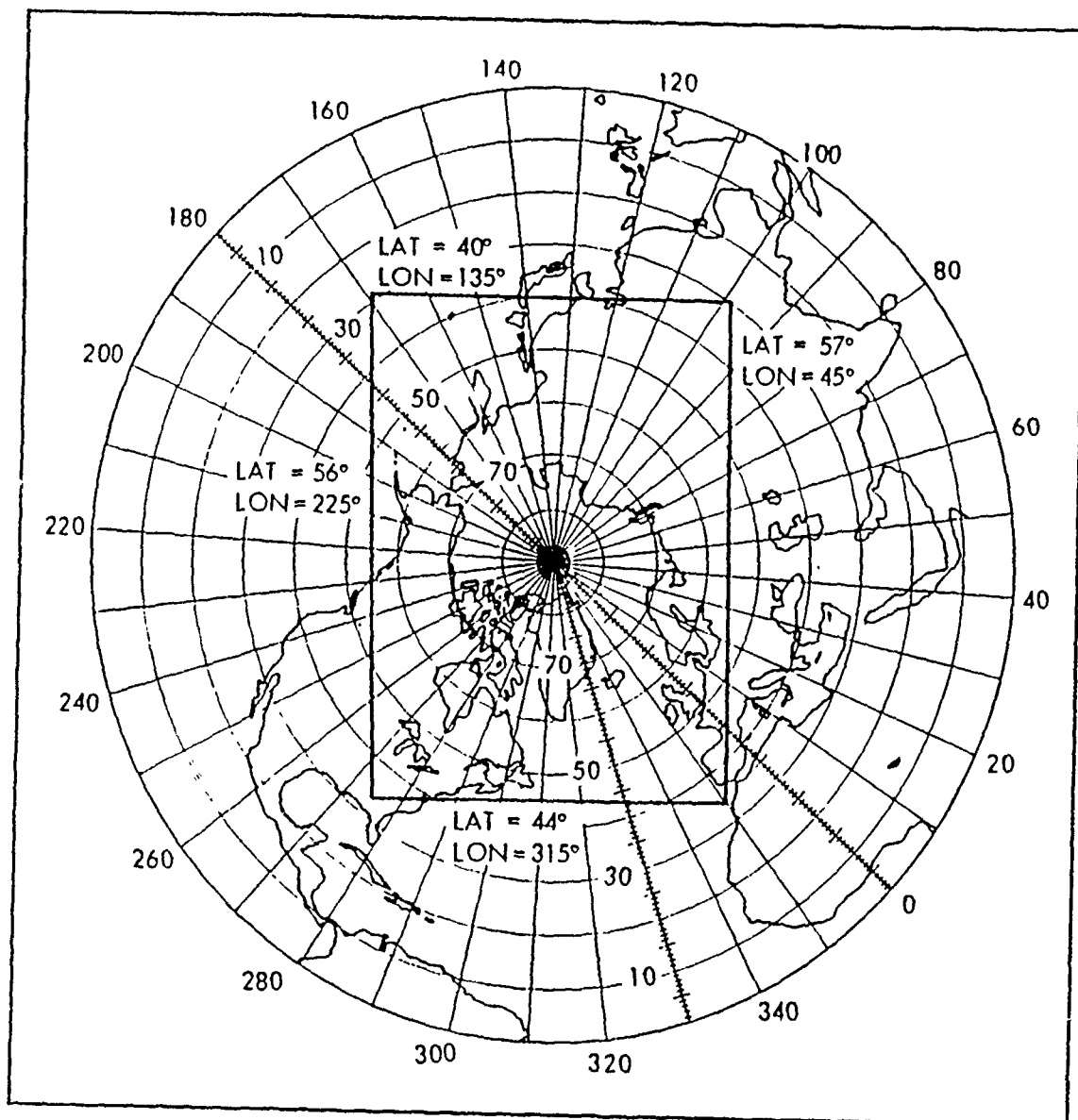


Figure 5 SSM/I north polar grid (from NSIDC, 1990).

III. CASE STUDY: ANOMALOUS DIURNAL CURRENTS ON THE YERMAK PLATEAU

A. BACKGROUND

1. The Yermak Plateau

The Yermak Plateau (Figure 6) is a hooked, finger-like extension of the Barents Sea continental slope, located off the northwestern coast of Svalbard. The plateau extends 400 km into the Arctic Ocean and covers roughly 20,000 km². Plateau depths range from 1000 to 600 m. The shallowest depth is 425 m on a ridge striking north-northwest near the plateau's central eastern edge (Perry, 1986). The plateau slopes down rapidly to 3500 m to the north and northwest. The eastern slopes gradually level out to a semi-enclosed 2000 m deep basin.

2. Regional Tides

Tides in the Arctic Ocean are predominantly semi-diurnal. Schwiderski (1986) developed a model for global tidal prediction based on a 1° by 1° grid with accuracies better than 10 cm. Figures 7 and 8 show the structure of the leading semi-diurnal (M₂) and leading diurnal (K₁) partial tides, respectively, for the Nordic Seas. Dashed lines depict the co-range lines measured in centimeters. The M₂ amplitude varies from zero at the amphidromic points to 80 cm and ranges from 20-30 cm over the Yermak Plateau. The amplitude of the K₁ tide varies only from zero to 10 cm, ranging from 2-5 cm over the Plateau.

Gjevik and Straume (1989) developed a regional tidal model to simulate the M₂ and K₁ tides for the Arctic Ocean and Nordic Seas with a 50 by 50 km grid size. The M₂ and K₁ amplitudes are similar to Schwiderski's global model.

The regional model also shows clockwise K1 current rotation along the west Norwegian shelf up to Svalbard. These authors believe this indicates the presence of a coastal trapped wave modal structure.

3. Observations

Anomalous diurnal currents over the Yermak Plateau were first reported by Hunkins (1986) from FRAM III and IV current meter data. The meters drifted from deep (4000 m) water to shallow water over the plateau's northwestern flank. Hunkins resolved absolute currents into orthogonal components in the along slope (60°) and cross slope (150°) directions and found that strong diurnal currents exist along the plateau's slope. Figure 9 shows current velocities at 104 m along with the bathymetric profile for the FRAM IV drift. During the deep water portion of the drift, the current record is noisy with some evidence of semi-diurnal tidal motion. Over the slope diurnal motion dominates the signal. Once on top of the plateau, the semi-diurnal signal returns. Kinetic energy spectra confirm the dominance of diurnal over semi-diurnal amplitudes (Figure 10).

Tidal motion polarization differs for the two tidal periods. Figure 11 shows a broad diurnal peak in the kinetic energy spectra near 150° and a minimum near 60° . Conversely, the semi-diurnal motions are nearly parallel to the slope with a maximum at 60° and a minimum at 150° . The semi-diurnal alignment agrees with the modeled M_2 tides for the Arctic Ocean (Kowlik, 1979 as cited by Hunkins, 1986). Hunkins believed the cross-shelf diurnal currents indicated strong topographic vorticity waves.

Strong diurnal currents were also reported from MIZEX 84 data. Morison et al. (1987) noted semi-diurnal currents dominated over most of the current meter drift record with amplitudes of 10 cm/s. Diurnal motions, however,

predominated when the current meter drifted over the southwestern slope of the Yermak Plateau. The diurnal component of motion ranged up to 12 cm/s.

The observations of Hunkins (1986) and Morison et al. (1987) were confirmed by Hoffman's (1990) analysis of ARCTEMIZ 86 drifter buoy tracks. He showed a strong correlation between the enhanced diurnal currents and bathymetry. While in deep water no significant peak in the energy spectrum at the semi-diurnal or diurnal period was found. However, once the buoys crossed the 3000 m contour into shallower water the energy spectra exhibited a diurnal peak which exceeded the semi-diurnal peak. Figure 12 is a buoy track that clearly shows diurnal clockwise looping over the plateau's northern slope. Hoffman also reported a periodic increase in diurnal clockwise motion that he associated with the fortnightly (spring-neap) beat in surface height inequality caused by the superposition of the two principal semi-diurnal tidal components.

4. Analysis

Hunkins (1986) showed that topographically trapped vorticity waves can exist at the diurnal frequency over the Yermak Plateau. He ignored the details of forcing and used a simple free wave analytic model. Chapman (1989) explored the actual forcing of the waves by the diurnal tide. He showed that a rectilinear oscillating barotropic current is significantly amplified by Hunkin's idealized representation of Yermak Plateau topography.

Recent work by Prazuck (1991) indicated high kinetic energy cells are possible on the Plateau. His linear barotropic numerical model created such cells in close agreement with observed diurnal currents. He showed through an analytic model that the highest energy cell could be due to the backscattered

energy of a coastally trapped wave that is unable to propagate beyond the tip of the plateau.

Prazuck concluded that the enhanced rotating diurnal currents may influence ice floe motion. The high energy cells would increase the grinding together of the floes and alter the break-up and freeze-up patterns in the region. Several phenomena might be related to this interaction:

- Strong turbulent fluxes associated with the diurnal currents such as those found during CEAREX 89 by Padman and Dillon (1991).
- Enhanced ambient noise in the region of grinding. Cousins (1991) correlated strong variations in ambient noise levels with 12 hour tidal/inertial oscillations east of the Yermak Plateau.
- Altered ice morphology due to the convergence/divergence of ice floes.

5. Effects on Sea Ice Characteristics

The interaction of the enhanced diurnal currents on the sea ice should be a seasonal phenomena. The high ice concentrations of the winter pack ice should significantly dampen floe motion, reducing the possibility of altering ice conditions. Lower ice concentrations in summer on the other hand should permit larger amplitude motions and increase the chances of remotely observable changes of sea ice characteristics.

Ice floe motion effects both ice concentration and morphology. The enhanced currents can induce local divergence in the ice field and raise or lower ice concentrations on a scale observable from space. Divergence and grinding together of floes can increase fracturing. Subsequent refreezing would increase

the fraction of first year ice in a predominantly multiyear ice field without significantly affecting the total ice concentration.

B. METHODOLOGY

Data from the NSIDC SSM/I CD-ROM data set were used to test the hypothesis that changes in ice concentration/morphology could be detected by satellite remote sensing. SSM/I data were used because, although visible and IR measurements provide higher resolution data, cloud contamination impede most attempts to examine a time series extending beyond a few days.

Sea ice concentrations were computed using the algorithm adopted by the NASA Sea Ice Algorithm Working Group (NSIDC, 1990). Gradient ratios were also calculated by modifying the ice concentration program to return gradient ratios instead of ice concentrations. The 25 km grid spacing used by the NSIDC data set was retained. Appendix A contains the software code listing.

Figure 13 shows how the Yermak Plateau region was divided into test and control areas. A strip of 5 pixels (125 by 25 km), extending over the northwestern flank of the plateau, was selected as the test area. Control areas of the same size were located 50 km to the northwest and 125 km to the southeast. These strips will be referred to as 'Slope', 'North' and 'South', respectively. A perpendicular strip 75 km upstream of the general ice flow, northeast of the plateau tip, was used to establish the gradient ratio of ice flowing into the test area.

A 168 day time series of daily ice concentrations, extending from 1 May to 15 October 1988, was studied. One four day and several one to two day data gaps in the record were filled by linear interpolation of surrounding values. As seen in Figure 14, ice concentrations varied from 75-100% during the period for the

northern and test strips, and dipped to as low as 35% for the southern strip. At other times of the year concentrations remained near 100%. For the gradient ratio analysis the time series extended from 13 January to 30 April 1988. This period avoided brightness temperatures contaminated by melt ponds.

C. RESULTS

a. Ice Concentration

The ice concentration algorithm was first checked for spatial consistency. Figure 15 shows concentration values for each pixel within the Slope strip during the period of interest. Table 3 contains a correlation matrix showing that the values are spatially consistent with 0.74 as the lowest correlation between the two endpoint pixels.

Differencing between the North - Slope and South - Slope concentration values (Figure 16) showed no significant deviations between ice concentrations over the slope and control areas. The North - Slope mean difference is 1.04%, well inside the 10% accuracy of the concentration algorithm. The Slope - South mean difference is larger at 8.56%, but as seen from the concentration record this is due to the generally lower concentrations in the South strip later in the summer.

The record was next examined for evidence of the fortnightly beat of current intensity reported by Hoffman (1986). If the currents influence ice concentrations, the largest signal should be present when the currents are strongest. An autocorrelation of Slope concentration values showed no significant correlations over a fortnightly period (Figure 17). Spectral densities were also computed for the mean Slope, North and South concentrations, as well as the North - Slope and South - Slope differences (Figures 18 - 19). In none of

these cases was a spectral peak located at or near the 13.66 day lunar fortnightly cycle (0.07 cycles per day).

TABLE 3: CORRELATION MATRIX FOR YERMAK SLOPE PIXELS

Position	Pixel 1	Pixel 2	Pixel 3	Pixel 4	Pixel 5
Pixel 1	1				
Pixel 2	.955	1			
Pixel 3	.881	.954	1		
Pixel 4	.803	.890	.963	1	
Pixel 5	.743	.823	.915	.966	1

b. Gradient Ratio

The gradient ratio is indicative of ice age. As shown in Table 2, the gradient ratio should be near zero for first year ice, less than zero for multiyear ice and greater than zero for sea water. The Siberian Branch of the Polar Drift Stream advects mostly multiyear ice through this region (Polarstern Scientific Party, 1988). If interactions between the diurnal currents and the ice are sufficiently strong to increase ice fracturing over the Yermak Plateau slope, the refreezing of

the resultant small leads should increase the total fraction of first year ice. An increased fraction of more saline ice will drive the gradient ratio more positive compared with the control areas to north, south and upstream of the flow.

Gradient ratios for the North, Slope and South regions are shown in Figure 20. Mean values are -0.033, -0.031 and -0.034, respectively. All gradient ratios are negative as expected from the predominantly multiyear ice. Although the gradient ratios are at least 26% higher over the slope than over the control areas during days 10 - 42, the difference between upstream and slope values is negligible for the same period (Figure 21). This means that no change measurable by the SSM/I occurred as the ice flowed over the slope region.

D. CONCLUSIONS

Anomalous diurnal currents over the Yermak Plateau slopes have been reported and analyzed by Hunkins (1986), Morison et al. (1987), Hoffman (1990) and Prazuck (1991). These currents have the potential for affecting the sea ice cover in this region in several ways. Divergence/convergence patterns could alter local ice concentrations. Stresses induced in the ice could lead to increased grinding and fracturing of floes, changing the morphology of the ice cover. If such changes could be noted through remote sensing, existing data bases could be explored for similar phenomena in other ice-covered regions.

Ice concentration/morphology changes are not observed by the SSM/I. Two explanations could account for this lack of confirmation:

- 1) The currents have little or no effect on the ice cover.
- 2) SSM/I limitations obscure features in the ice caused by the currents.

Factors supporting the second hypothesis include poor SSM/I spatial resolution and contamination by melt ponds or snow cover. Passive microwave emissions

observed by the SSM/I are too imprecise to verify the anomalous current effects on the sea ice cover.

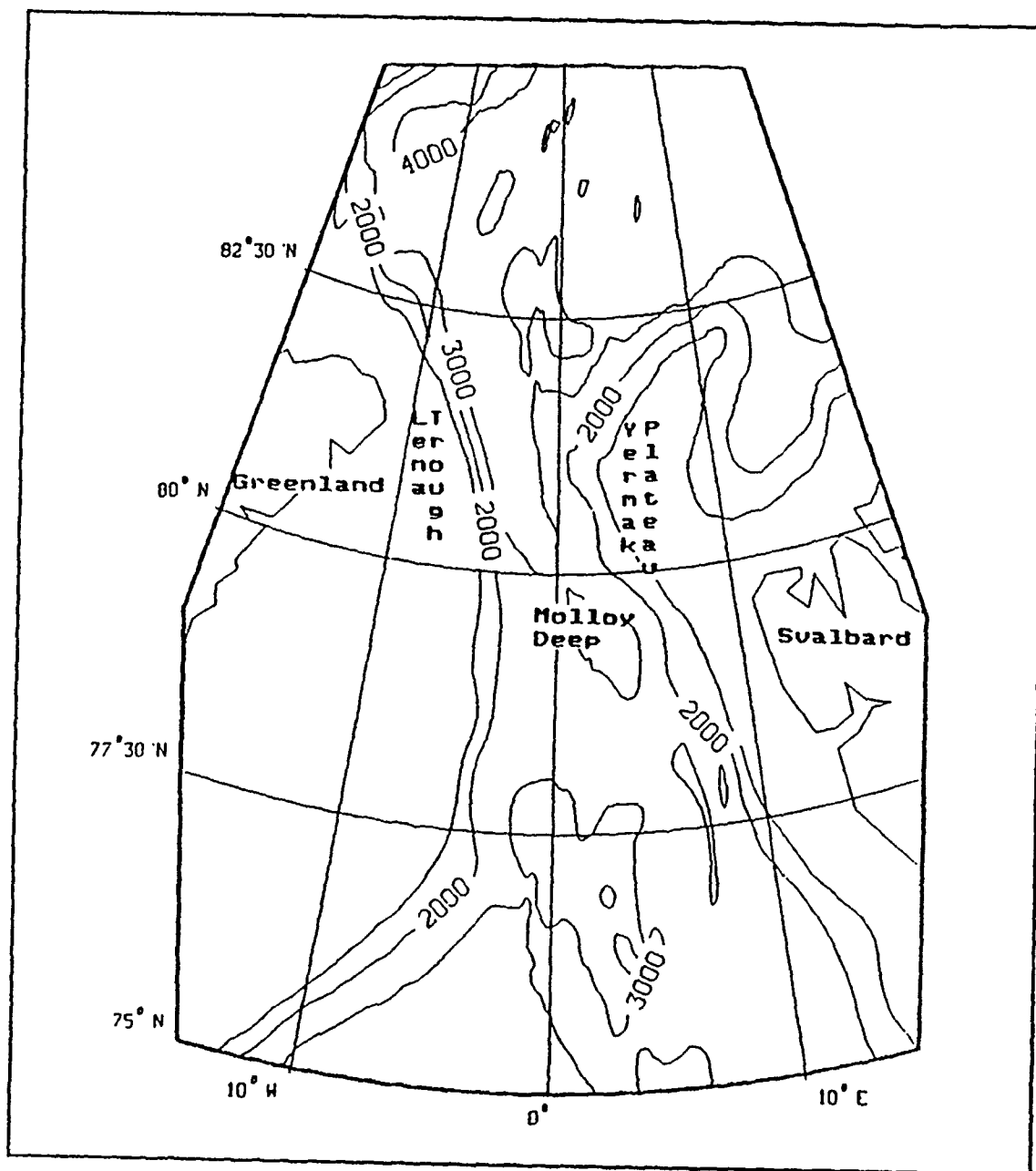


Figure 6 Bathymetric chart of the Yermak Plateau (from Hoffman, 1990).

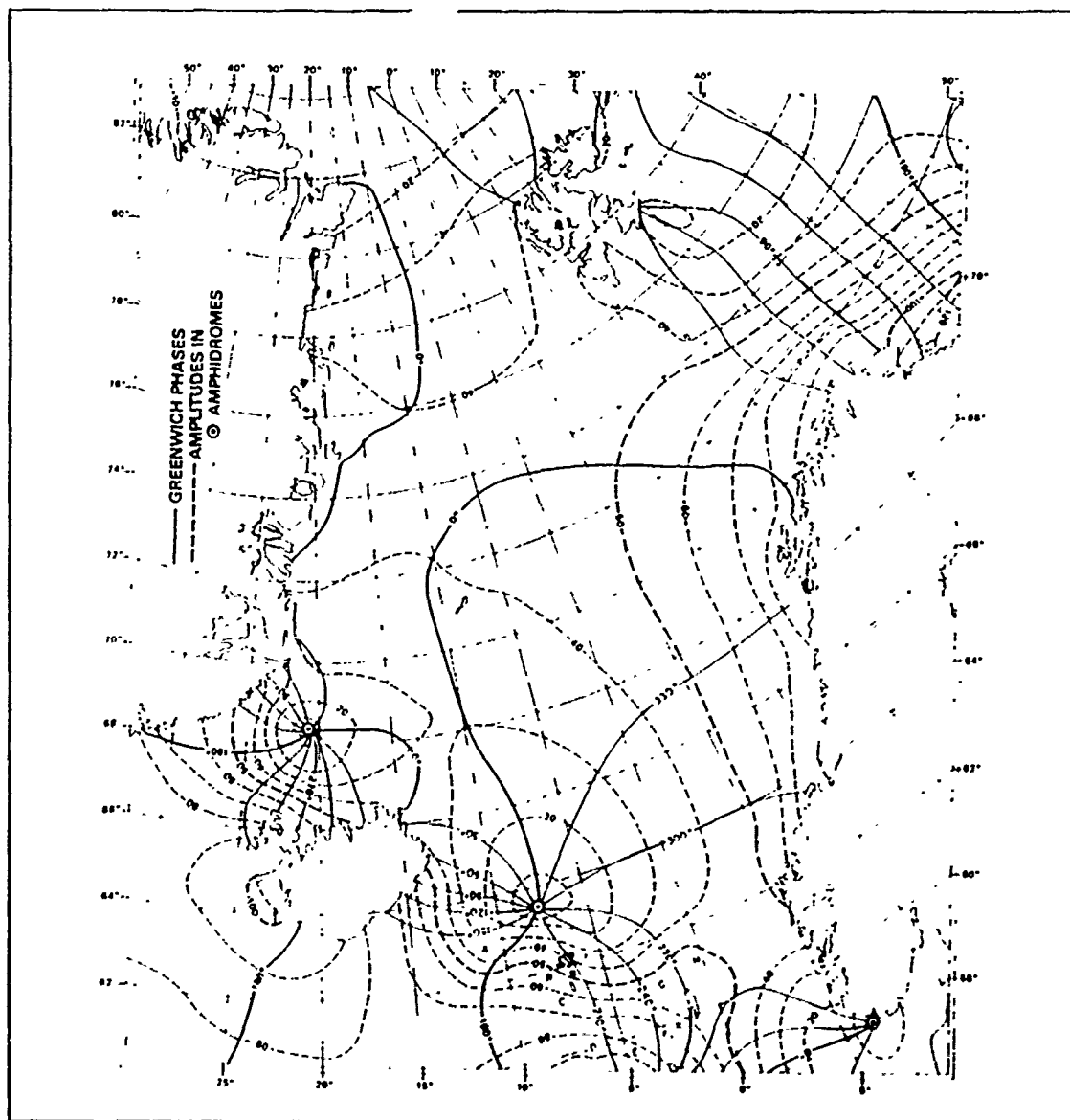


Figure 7 Leading semi-diurnal (M_2) ocean tide (from Schwiderski, 1986).

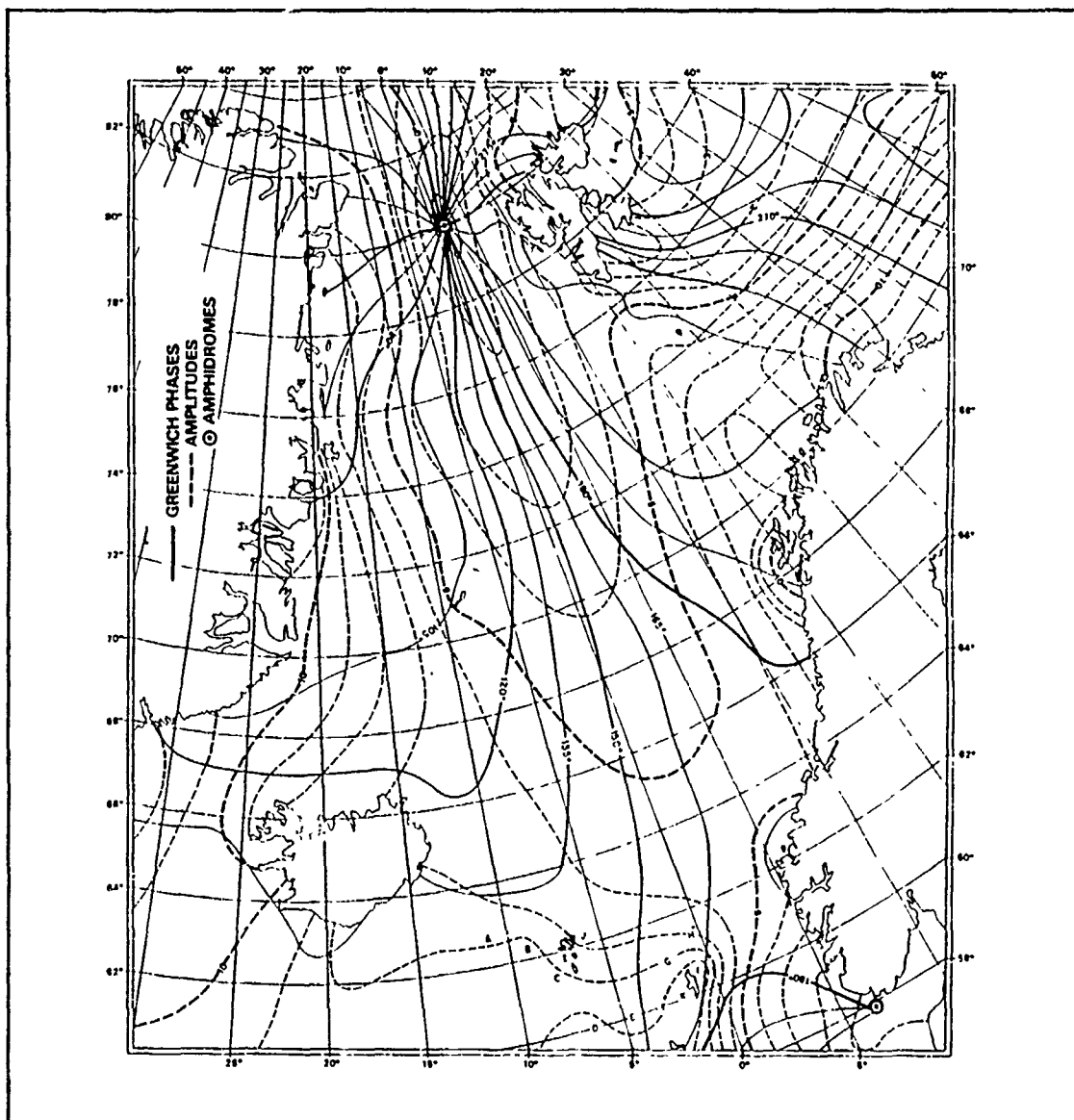


Figure 8 Leading diurnal (K_1) ocean tide (from Schwiderski, 1986).

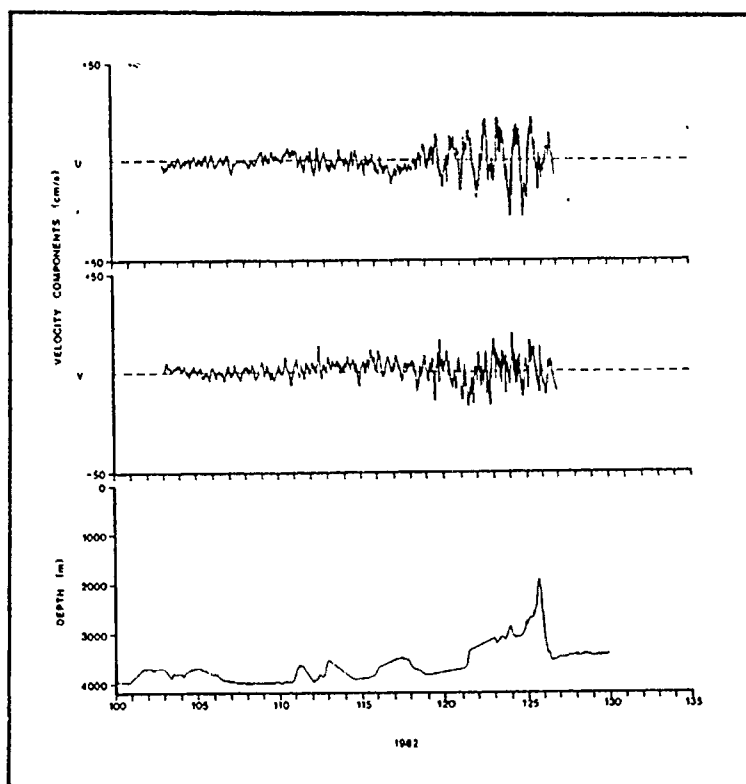


Figure 9 Absolute current velocities along the FRAM IV track at 104 m (from Hunkins, 1986).

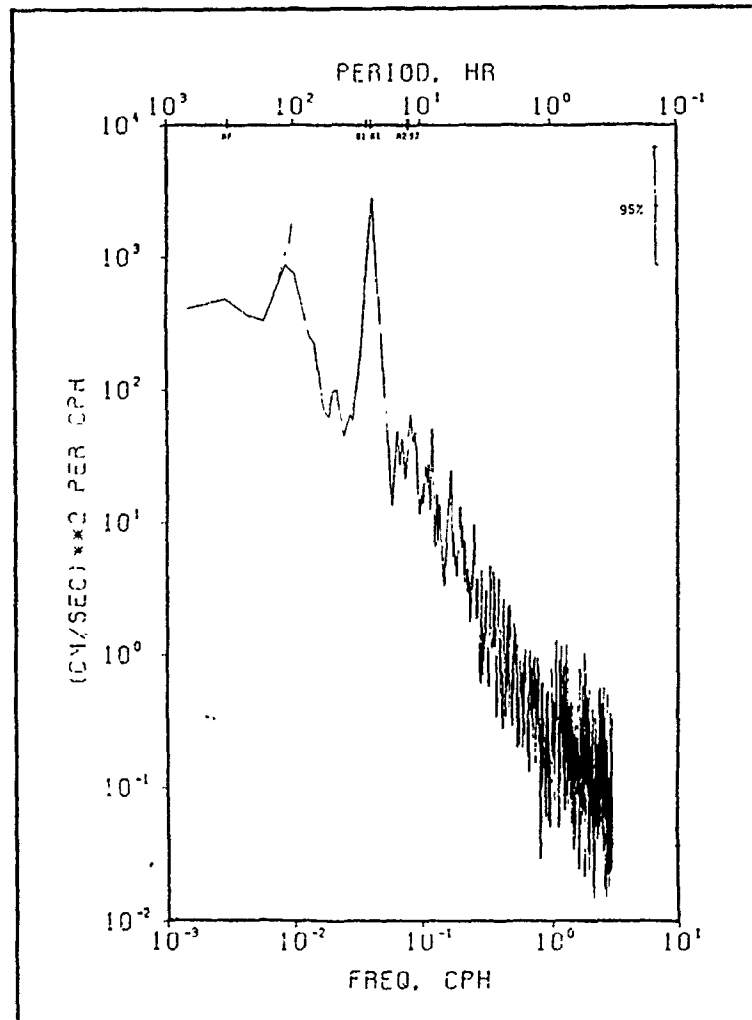


Figure 10 Kinetic energy spectra for the cross slope velocity component from FRAM IV at 303 m (from Hunkins, 1986).

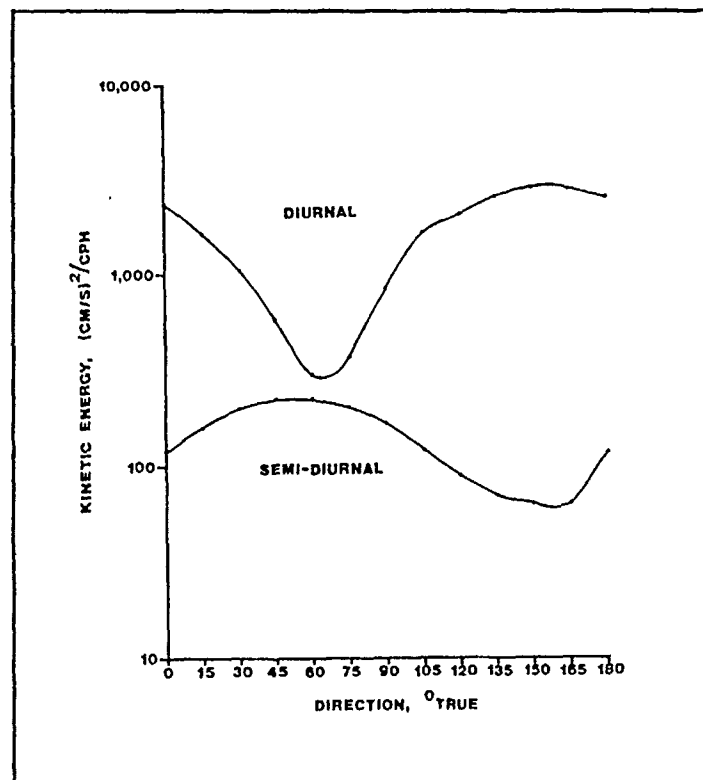


Figure 11 Peak amplitudes of kinetic energy for the K_1 and M_2 frequencies as a function of current axis orientation for FRAM IV at 303 m (from Hunkins, 1986).

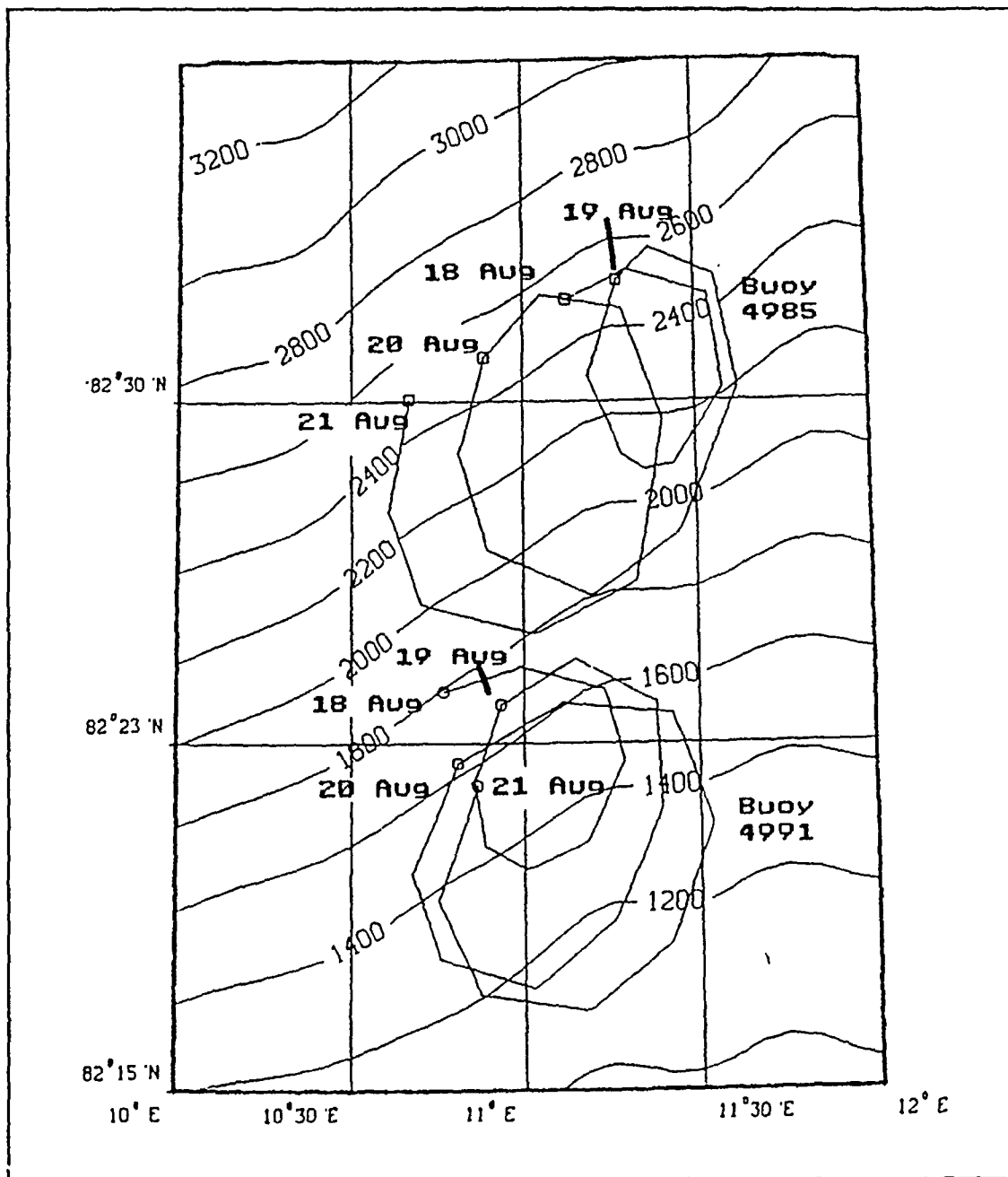


Figure 12 Diurnal looping of ARCTEMIZ 86 drifter buoys (from Hoffman, 1990).

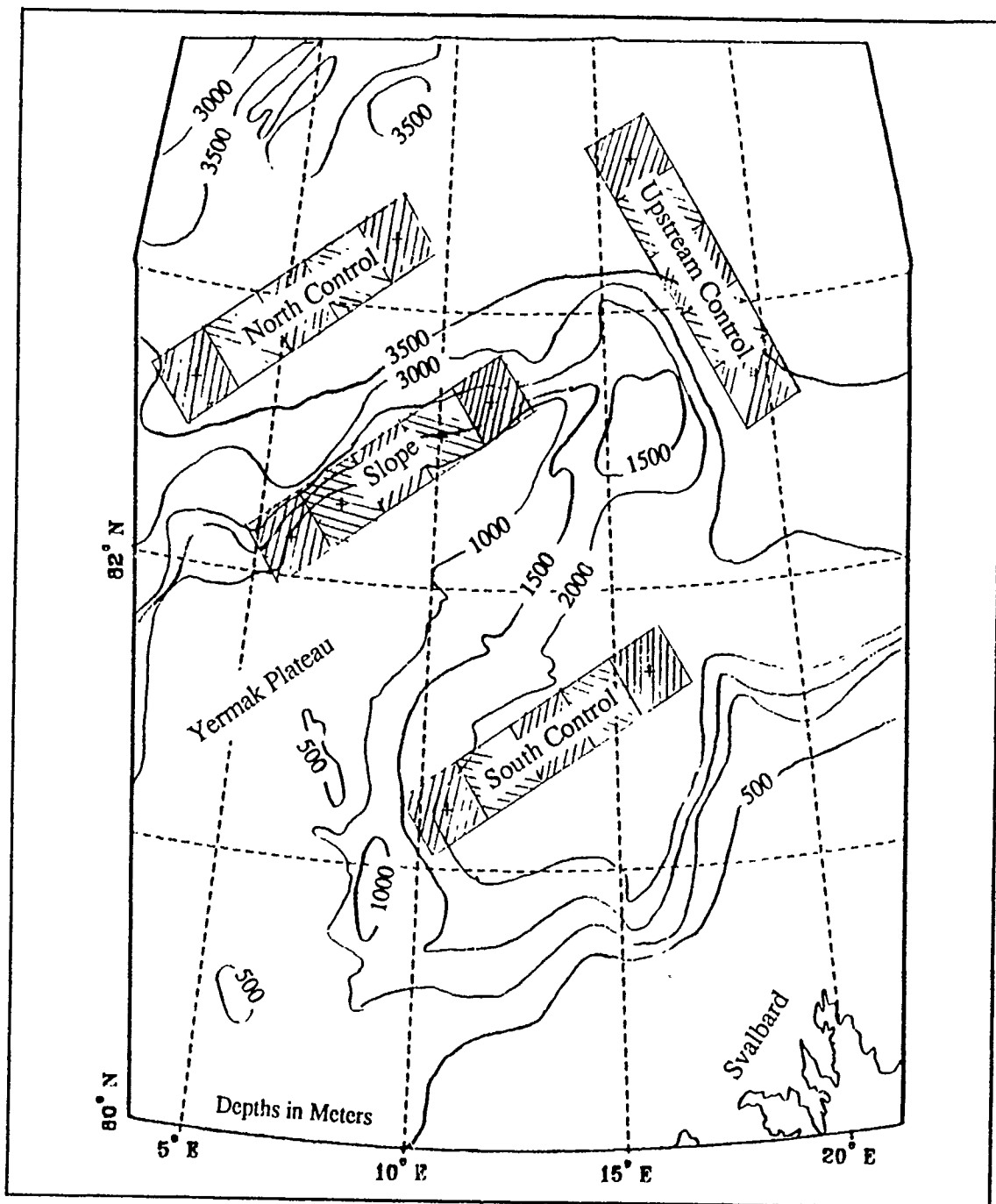


Figure 13 Yermak Plateau test and control areas. Hatched boxes indicate individual pixels. Depths are in meters.

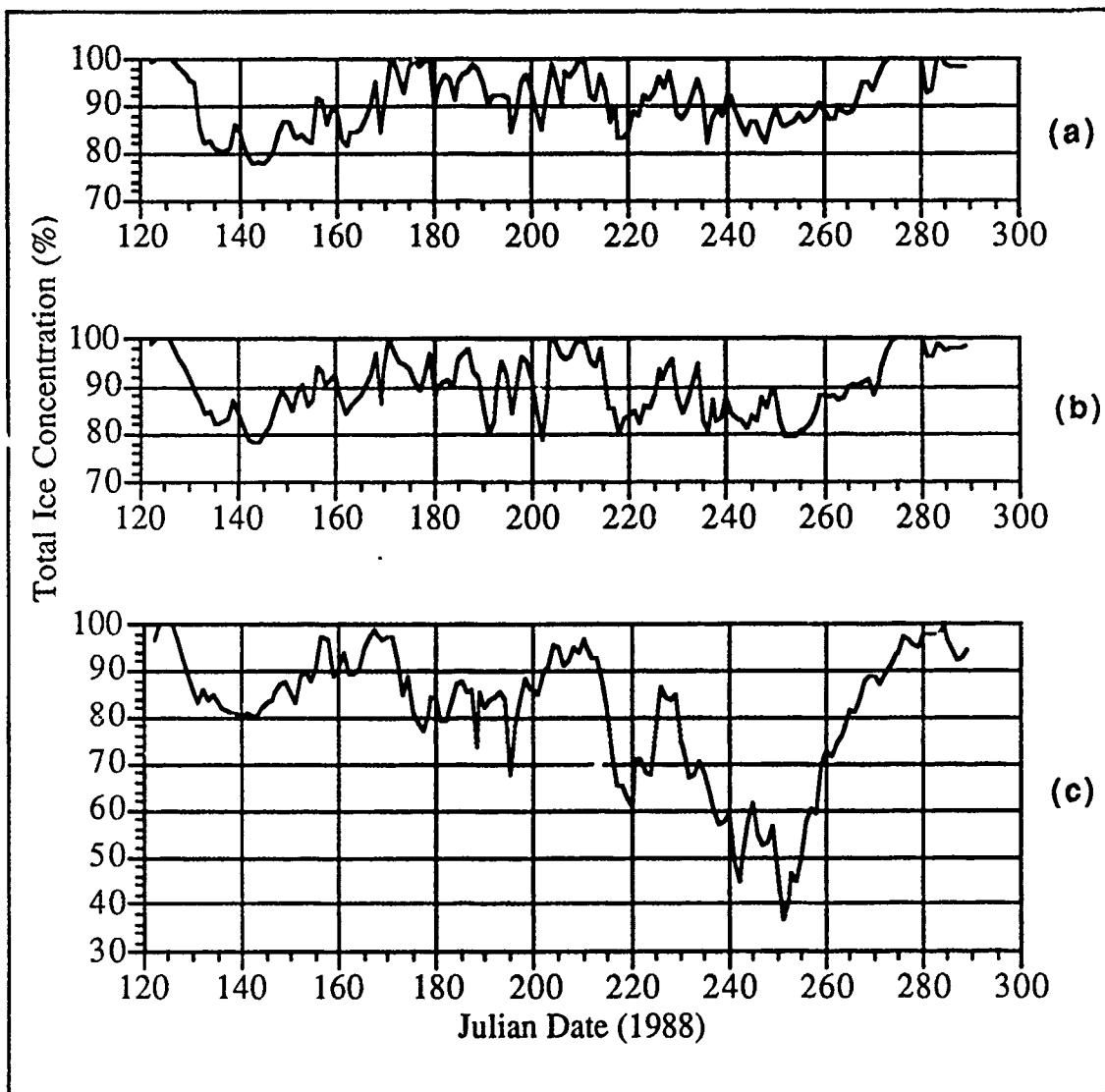


Figure 14 Total ice concentrations, 1 May - 15 October 1988: (a) North control, (b) Slope and (c) South control.

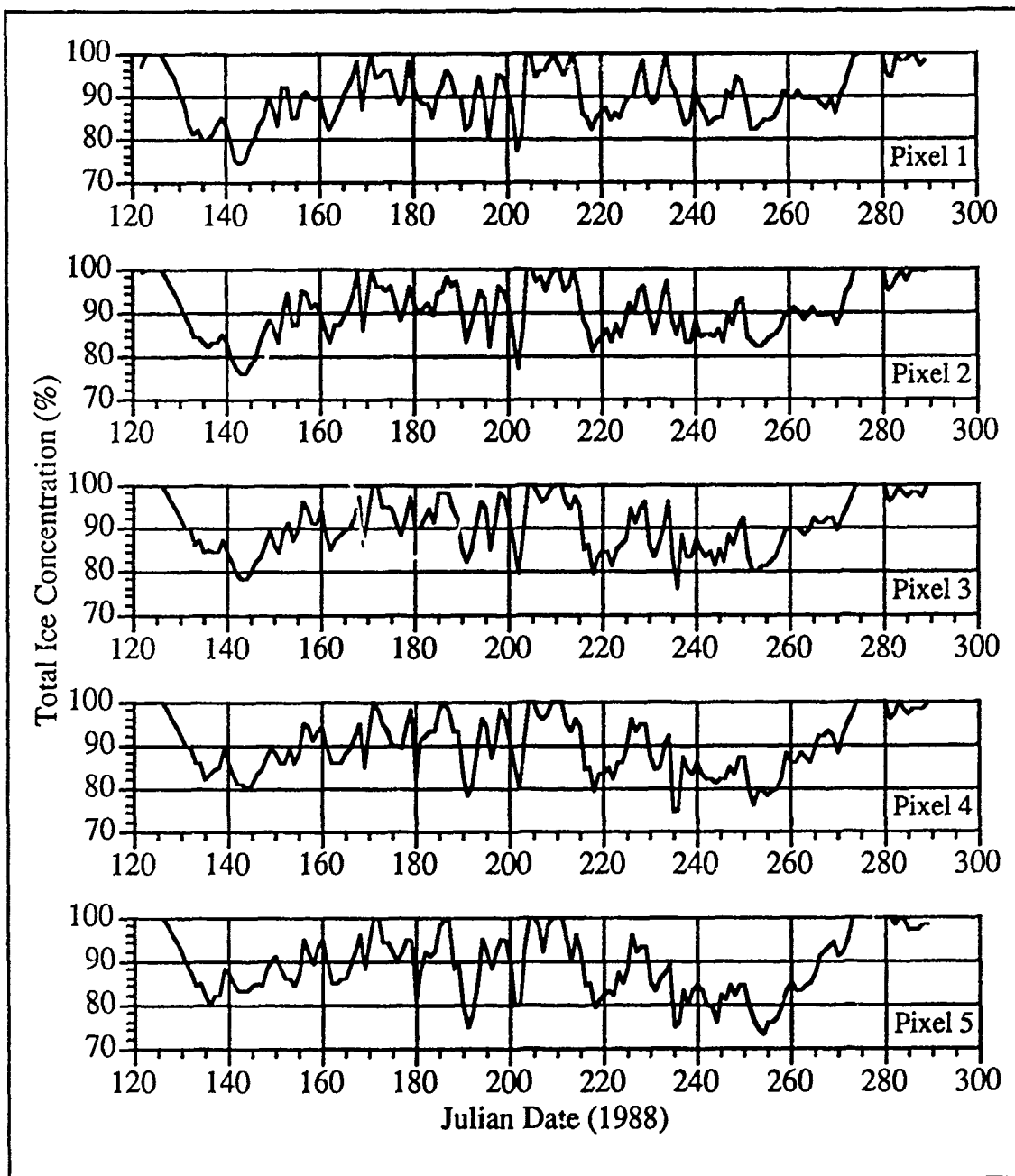


Figure 15 Yermak slope ice concentrations, 1 May - 15 October 1988.

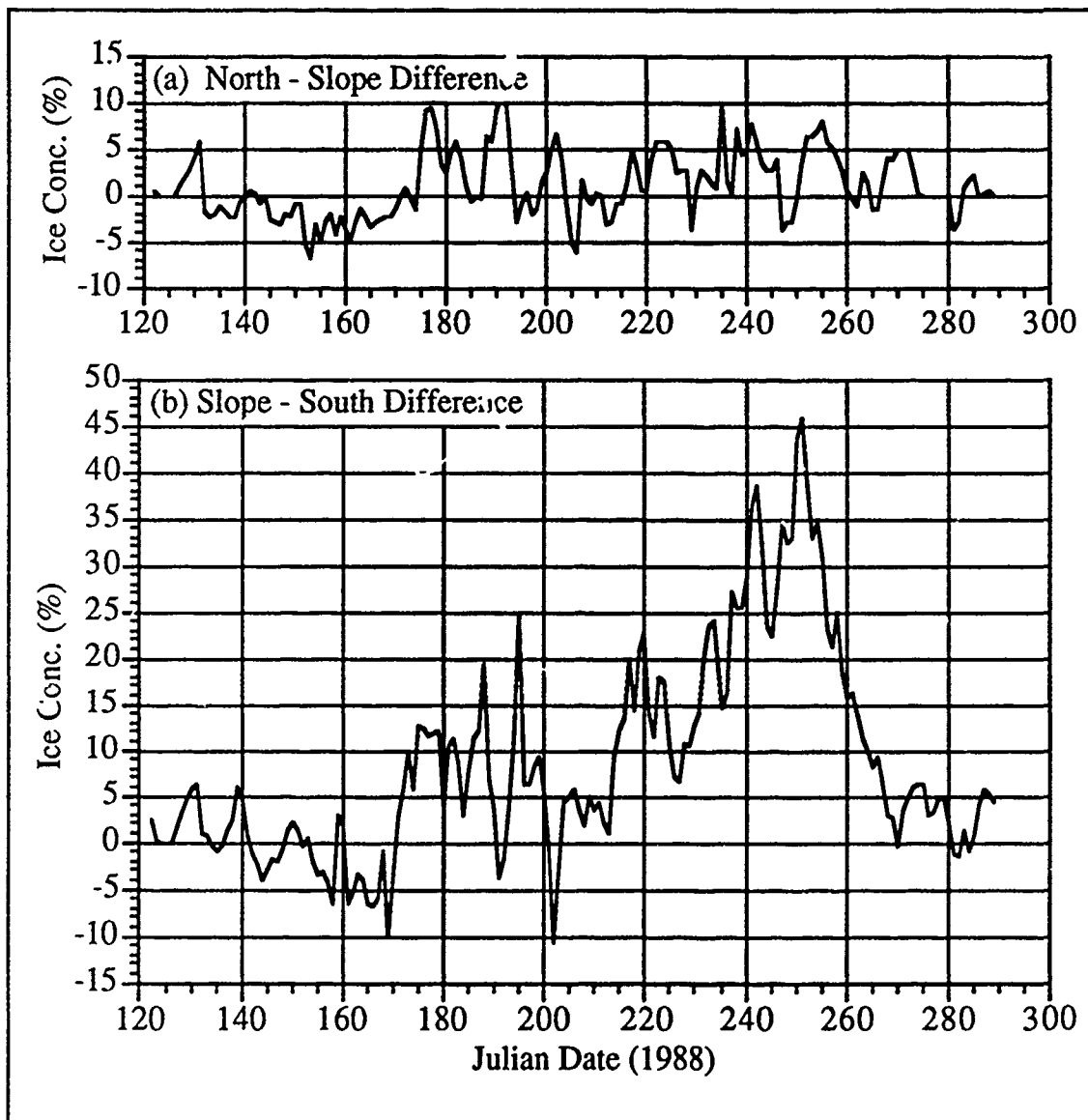


Figure 16 Percent concentration differences (1 May - 15 October 1988): (a) North control minus Slope, (b) South control minus Slope.

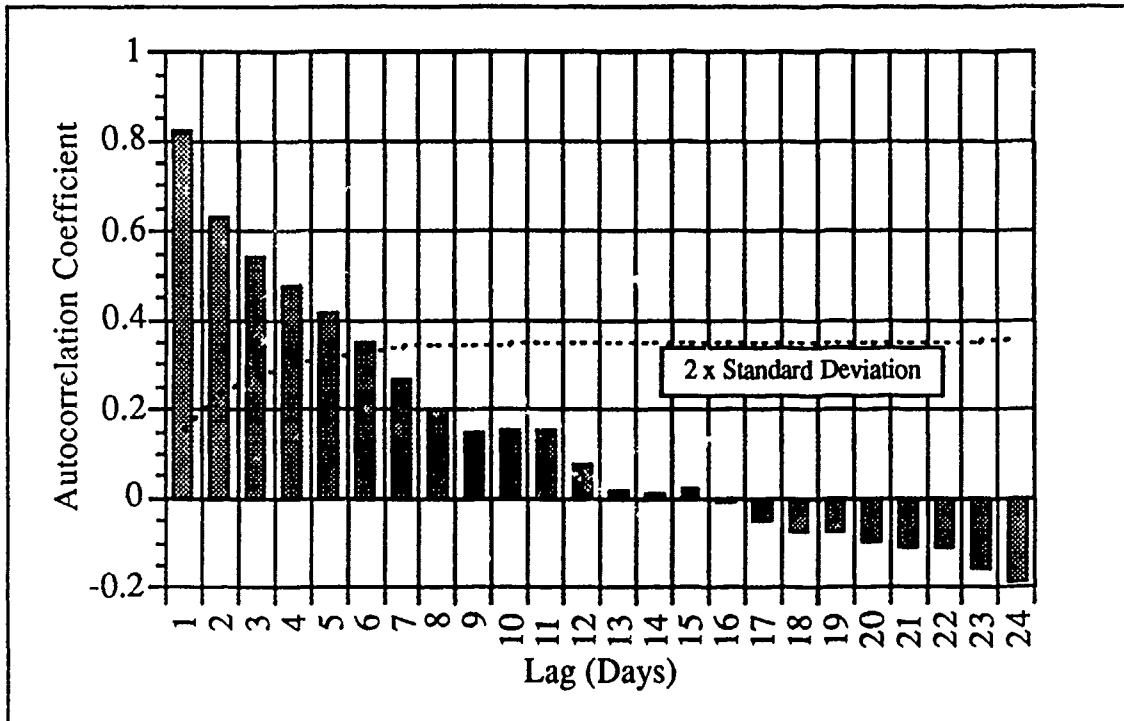


Figure 17 Autocorrelation of slope region ice concentrations.

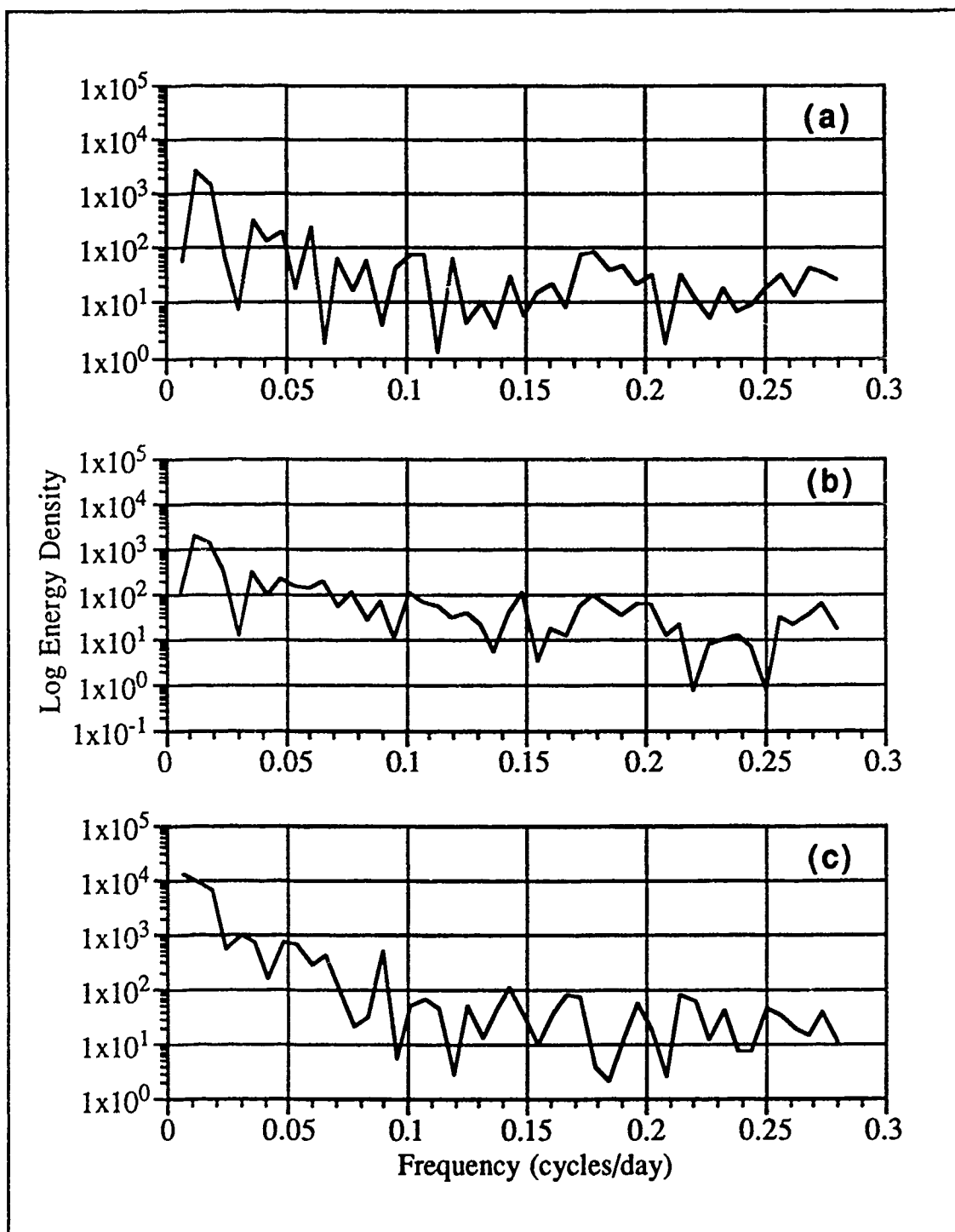


Figure 18 Ice concentration spectra (1 May - 15 October 1988): (a) North Control, (b) Slope, and (c) South control.

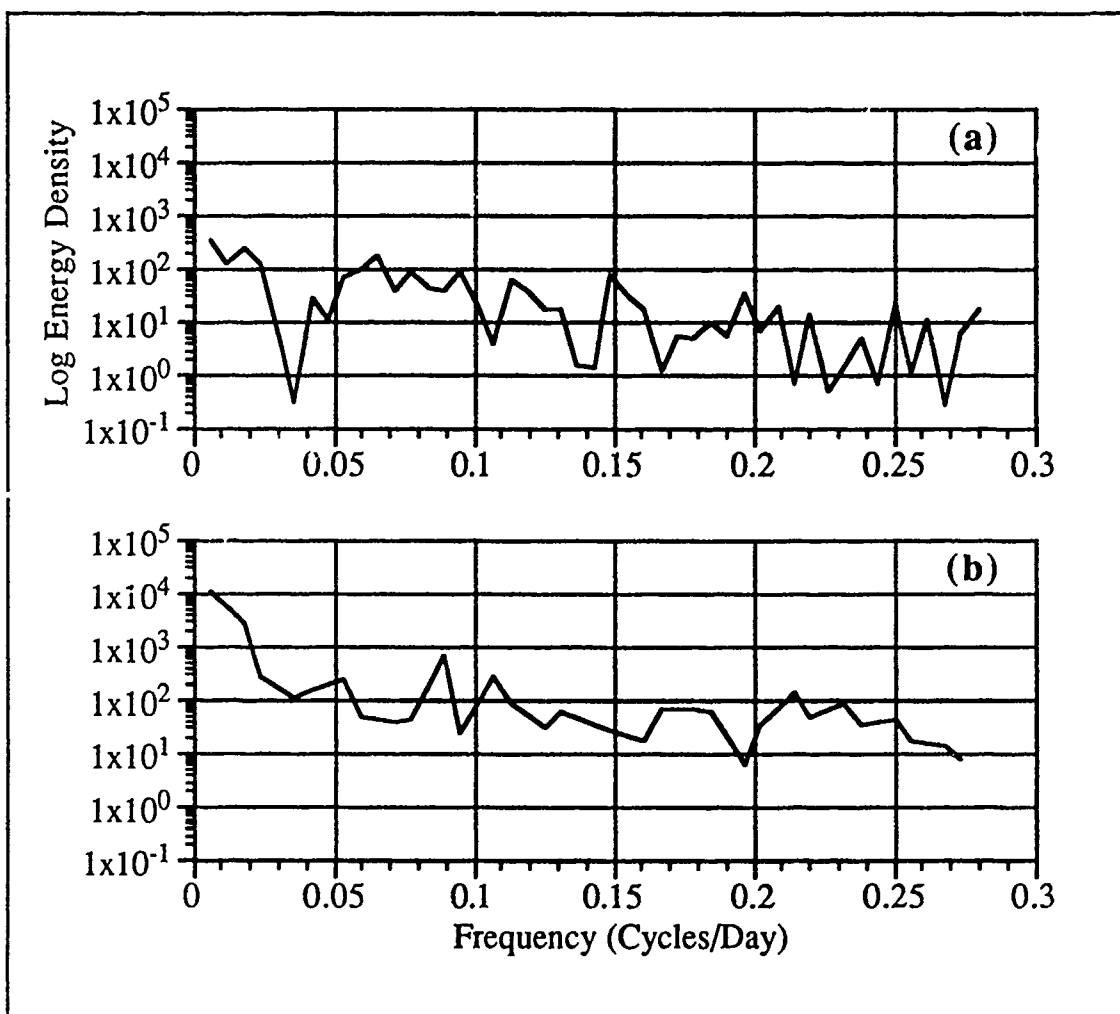


Figure 19 Ice concentration spectra (1 May - 15 October 1988): (a) North - Slope difference and (b) Slope - South difference.

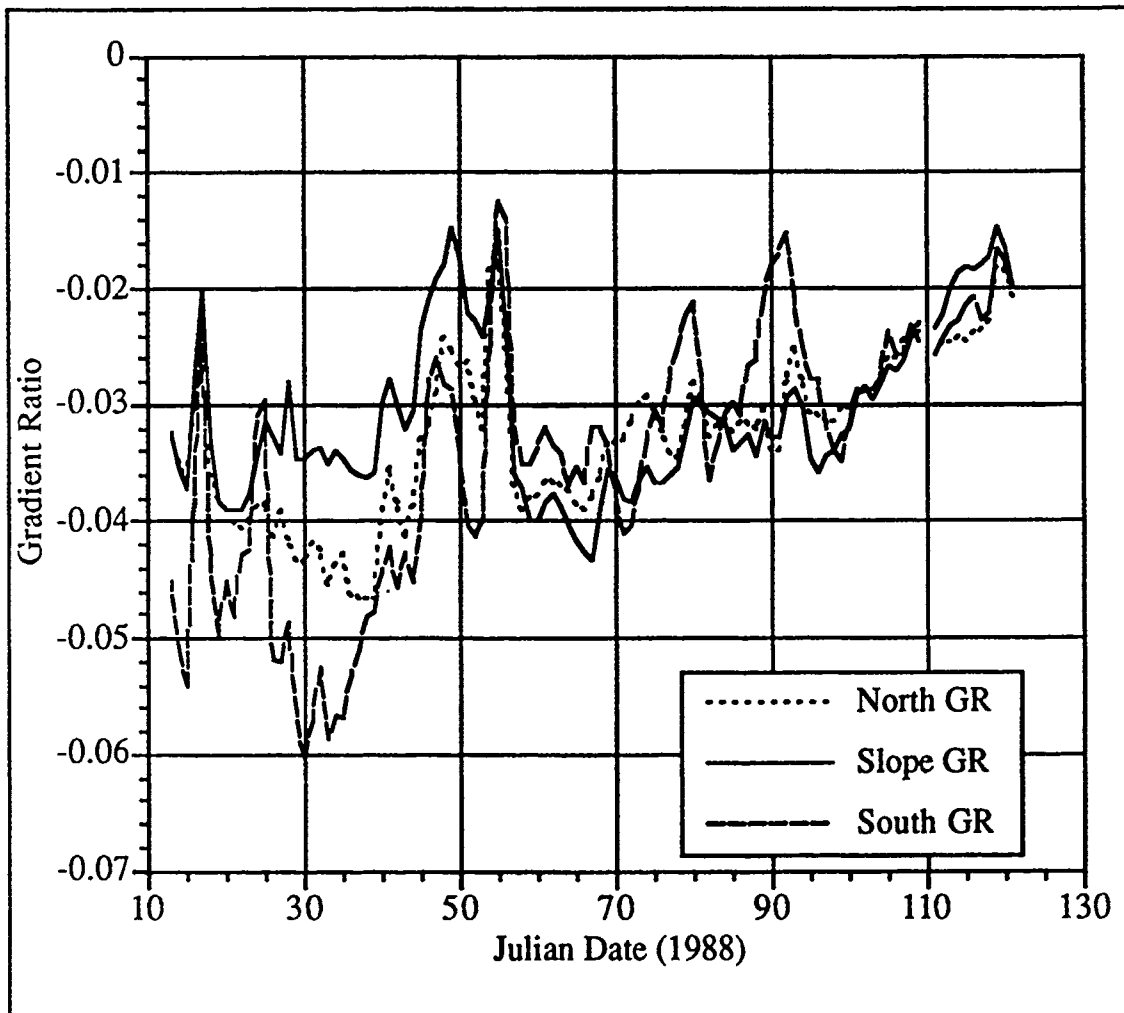


Figure 20 Gradient ratios for Slope and Control areas, 13 January - 30 April 1988.

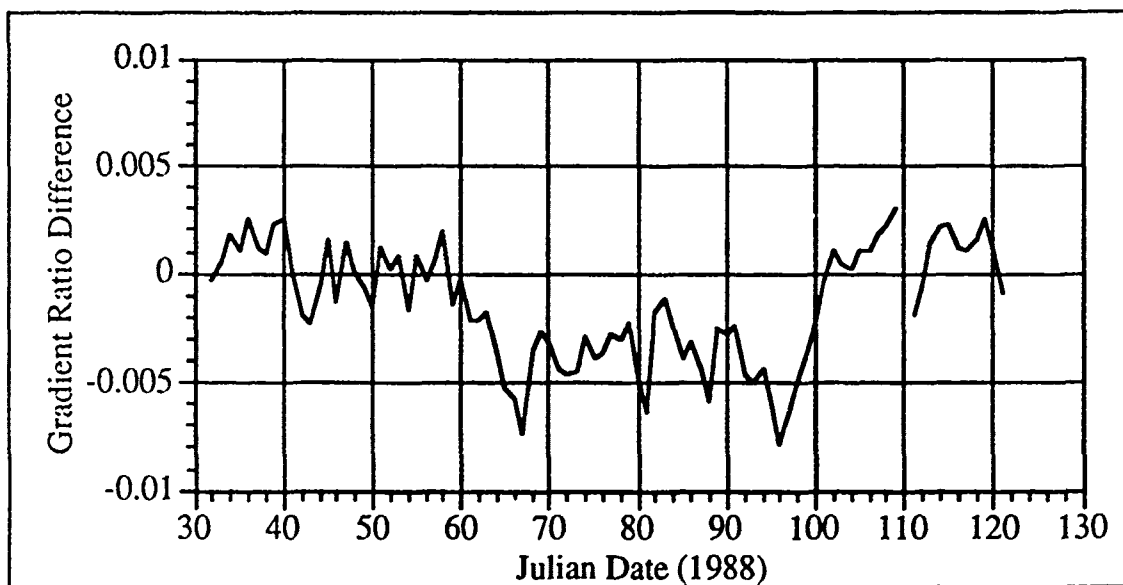


Figure 21 Slope - Upstream gradient ratio difference, 1 February - 30 April 1988.

IV. CASE STUDY: ICE MOTION ANALYSIS

A. BACKGROUND

1. General Ice Flow

Sea ice motion affects a variety of important arctic processes. Carsey and Holt (1987) note that ice movement affects latent heat advection, oceanic surface stress, open water production through divergence and shear, is a passive tracer of ocean currents, and affects icebreaker navigation and ice structure. Within the central ice pack, relative ice motion creates both open water, through which significant heat is lost, and ridges that are operational hazards. At the ice margins ice growth associated with divergence affects brine production which, in turn, influences intermediate and deep water formation.

Ice motion is primarily due to local surface wind stress, ocean currents, Coriolis and inertial forces, and effects of horizontal stresses transferred through the ice itself (Hibler, 1986). Colony and Thorndike (1984) examined a 90 year record of ship, research station and buoy tracks to create a quantitative estimate of the mean ice motion in the arctic basin (Figure 22). Two features dominate the circulation pattern—the anticyclonic Beaufort Gyre in the Canadian Basin and the Transpolar Drift Stream (TDS) extending across the Eurasian Basin to Fram Strait.

The TDS is the largest and most concentrated meridional ice flow in the world. It is the primary outflow region for arctic sea ice. Variations in flow magnitude are theorized to effect the global climate (Vinje and Finnekasa, 1986). As seen in Figure 23, the TDS is composed of two branches. The Polar Branch

advects old multiyear ice across the pole and out through Fram Strait. The Siberian Branch contains thick, deformed multiyear ice floes that probably originated on the Siberian shelves. Closer to the Yermak Plateau, generally thin, first year ice formed locally or in the Barents and Kara Seas is found (Polarstern Scientific Party, 1988). The merging of these different ice types makes Fram Strait a rich area for SSM/I feature tracking.

2. Feature Tracking

Feature tracking estimates motion of a fluid by tracking features that are advected in the fluid. Zhang (1991) identifies two main steps necessary for successful feature tracking:

- 1) Tie point selection - Identification in the first image of suitable features to be tracked; and
- 2) Tie point registration - Matching the same tie points in a subsequent image.

The underlying assumption is that the tracked features are advected by the fluid. Motion vectors are representative of the surrounding medium only when this assumption is valid. Possible disruptive influences include waves in the fluid, when fluctuations in fluid properties are tracked rather than the Lagrangian flow of the fluid, atmospheric contamination which can temporarily obscure features, and Eulerian effects such as local heating or cooling that provide feature sources and sinks.

In the past sea ice motion has been inferred from the drift records of ice-locked ships, manned research stations and buoy tracks. The number and spatial density of these in-situ observations is limited. Satellites offer the advantage of

repeated sampling over large areas—a potentially rich source of information on the spatial and temporal structure of the sea ice motion field.

Sea ice movement can be computed from displacements of features in sequential images. Subjective techniques, which require manual tracking of specific floes, are labor intensive and subject to repeatability problems due to differences in operator training. Automated techniques, such as the maximum cross correlation method described by Ninnis et al. (1986), are much more efficient but must be heavily filtered to remove spurious movement vectors.

Three electromagnetic regimes are currently available for passive space-based observations of ice motion. In order of decreasing resolution, they are visible (0.3 - 0.7 μm), infrared (3 - 12 μm) and microwave (0.3 - 1.5 cm). The major limitations of high resolution visible and IR imagery are their inability to penetrate cloud cover and the light dependence of visual wavelengths. For example, Emery et al. (1991) investigated Fram Strait ice motion with IR imagery but were limited to six images over a 10 day period in April 1986 that contained exceptionally cloud-free conditions. On the other hand, low resolution passive microwave imagery can penetrate clouds and are independent of light conditions.

Active microwave systems offer the advantages of cloud penetration and light independence with much higher resolutions than passive methods. For example, Synthetic Aperture Radar (SAR) data from SEASAT had a resolution of 25 m (Carsey and Zwally, 1986). SAR information from the ERS-1 satellite will soon be available, however its application will be limited due to the limited sampling in time and space, especially in the subpolar regions (Zhang, 1991).

Many researchers believe satellite passive microwave sensing is unsuitable for tracking ice motion (Zhang, 1991; Cavalieri, 1991 personal

communication) due to its inherent coarse spatial resolution. The primary use of this satellite data for arctic sea ice studies has been to examine the temporal and spatial variability of the ice cover. Svendsen et al. (1983) reported the motion of a patch of high multiyear ice concentration that correlated well with buoy movements, but the potential for feature tracking has not been pursued in the published literature (Cavalieri, 1991 personal communication).

One can understand why passive microwave feature tracking has been overlooked. As mentioned earlier, brightness temperatures are sensitive to variations in surface conditions such as wet snow or melt ponds. The spatial resolution is too coarse to track individual floes. Judicious application of SSM/I data, however, can overcome these limitations. The basic requirements are large scale spatial gradients in ice type (as determined from gradient ratios) to overcome the coarse data resolution, and small temporal variability of surface conditions to limit melt pond or wet snow contamination. The first requirement is achieved by examining areas where old and new ice merge. The second requirement is met by rejecting data during the summer melt season.

These two restrictions limit the wide-scale use of inferring ice motion through SSM/I feature tracks. Regions where this technique shows the most promise, however, are areas of high interest such as Fram Strait, through which occurs approximately 90% of the heat exchange and 75% of the mass exchange between the Arctic and World Oceans (Aagaard and Greisman, 1975).

B. METHODOLOGY

1. Satellite Images

Multiyear ice fractions were calculated using the NASA gradient ratio technique described earlier. The same software that computed ice concentrations

and gradient ratios for the Yermak Plateau case study was used to create multiyear ice fraction images. Appendix A contains the FORTRAN code listing. The software merges the computed multiyear ice fractions with a land mask to produce a 304 by 448 pixel polar stereographic representation of the arctic region, extending from the pole south to 70° N. The pixel resolution is 25 km.

Images were produced from the NSIDC Winter 88 and Winter 89 data sets. Images were created at 3 day intervals. If one assumes a typical 10 cm/s ice speed, a feature advected by the flow will move nearly 26 km over 72 hours. Since the grid resolution is 25 km, a 3 day sampling interval is the minimum needed to show expected movement of a feature within the data set.

The imagery was displayed on a Macintosh II desktop computer using Imagic image processing software (Norris and Emery, 1989). Imagic was designed to display satellite remote sensing imagery on the Macintosh and is distributed by NSIDC with the CD-ROM data set. Images were color enhanced to accentuate multiyear ice features and looped to provide a continuous animation of feature movement.

2. Feature Tracking

The two main steps for determining ice motion from successive images are tie point selection and registration. These steps are achieved in this study through subjective imagery analysis following rules that could be incorporated into an objective scheme. Tie points are selected by identifying spatially coherent features through a visual inspection of the animated imagery. These tie points are registered in succeeding images by matching the same points in their new locations. This procedure is described in detail below:

- 1) Create a series of multiyear ice fraction data sets.

2) Load the data sets into Imagic and generate ice fraction images. Decide on a color enhancement scheme that best shows multiyear ice features and apply this enhancement to all images.

3) Using Imagic, observe the advection of the multiyear ice features.

4) Select features that appear to be advected with the general ice flow according to the following criteria:

- Size - Features must be small, no more than 100 km across (4 pixels). Accurate tiepoint registration within larger features is too difficult.
- Background Discrimination - Features must stand out from the background by at least 10 percentage points for most of their lifespan. This increases one's confidence that what is being observed is actually a feature advected in the flow rather than random variability of multiyear ice fractions.
- Temporal Coherence - Features must be present in a least 6 consecutive images (18 days). This further reduces the possibility of spurious tracks due to temporary brightness temperature fluctuations in the ice cover.

5) Record the pixel position of an appropriate tie point within the feature during its lifespan using the following guidelines:

- If one pixel value is 3 percentage points or more higher than all other values within the feature, select it.

- If 2 or more pixel values are within 3 percentage points, select the pixel which best corresponds to the previous relative position of the tie point within the feature.
- If the relative maximum within the feature is ambiguous, choose the pixel which most conserves ice motion.

6) Convert the pixel location within the polar stereographic grid to geodetic latitude and longitude using software supplied by NSIDC. A version modified for the Macintosh is listed in Appendix A.

7) Determine ice velocities by measuring the change of position with time. FORTRAN code that converts geodetic positions to u and v components of velocity is also contained in Appendix A.

An example of the feature tracking technique is shown in Figures 24 through 26. This particular feature was tracked from 1 February through 22 April 1988 as it moved southward down the east coast of Greenland. Figure 24 contains six consecutive images of multiyear ice fraction contour plots from 3 - 17 March. Each plot covers the same 500 by 250 km region centered at 76.1°N, 13.5°W (note the Greenland coast in the lower left corner of the plots). An area of relatively high multiyear ice fractions can be seen migrating from the upper left to the lower right corner of each plot. This is the trackable feature. Figure 25 shows pixel values for this same region expressed as multiyear ice fractions. The circled number is the feature tie point. Pixel locations were converted to geodetic coordinates and the u and v velocity components are shown in Figure 26.

3. Feature Selection

The number of trackable features depends on the region of interest. For example, the generally homogeneous conditions in the high arctic (above 85°N)

create a poor environment for feature tracking. No suitable features were observed in the 1988 data set. Only two features in the high arctic were observed during the 1989 winter season. On the other hand, Fram Strait is a potentially rich area due to the merging of the Siberian and Polar branches of the TDS.

To assess the validity of this feature tracking technique, the trajectories of multiyear ice features were compared with true ice motion using the arctic data buoy program as ground truth for the ice velocities. The criterion to colocate trackable features with a drifting buoy was challenging. Suitable features had to be identified and their positions compared against buoy tracks as reported in Colony and Rigor (1990 and 1991). Three feature-buoy matchups were selected from the winter 88 data set, each representing a different region of the arctic. Named after the closest geographic reference point, the features are Severnaya Zemlya (SZ), Franz Josef Land (FJL), and East Siberian Sea (ESS). A feature from the Winter 89 data set (CA) was chosen to represent motion in the central arctic basin. Although no satisfactory matchup between a trackable feature and a drifting buoy was found in the Fram Strait region, a buoy (#7001) that passed down the Greenland coast two weeks ahead of a feature (FRAM) was used for a relative comparison of the ice trajectory.

The tracked features and ground truth buoys were not coincident in space; the average distance between the selected features and buoys varied from 76 to 557 km. The closest matchup (76 km) occurred between FJL and buoy #1790. The ESS feature was 420 km from buoy #1896. SZ was 320 km from the buoy #7048. CA averaged 497 km from the closest buoy (#3288). Table 4 summarizes the characteristics of the feature-buoy tracks.

TABLE 4: MYI FEATURE - BUOY DATA

Feature	Buoy	Separation (km)	Start Track Date	Position	Stop Track Date (Total Days)	Position
ESS	7048	420	1 APR 88	76.2N, 160.1E	25 APR 88 (24)	77.3N, 159.0E
FJL	1790	76	1 FEB 88	80.2N, 41.3E	14 MAR 88 (42)	79.5N, 41.9E
SZ	1897	320	1 FEB 88	81.7N, 105.9E	28 APR 88 (85)	82.0N, 100.6E
CA	3288	491	1 JAN 89	84.5N, 143.5E	31 MAR 89 (90)	86.6N, 125.2E
FRAM	N/A	N/A	1 FEB 88	79.9N, 4.6W	22 APR 88 (80)	68 1N, 23.9E

Geolocation Key: SZ - Severnaya Zemlya
FJL - Franz Josef Land
ESS - East Siberia Sea
CA - Central Arctic
FRAM - Fram Strait

Note: Features are named according to nearby geographic reference points.

4. Errors

Before ice motion vectors between the buoy - feature pairs are compared, the maximum errors inherent to this technique are described. Three types of positional errors are possible: imperfect tiepoint registration, SSM/I data geo-location, and ARGOS buoy positioning. In addition, ice velocity gradients between the feature and buoy locations need to be considered. These errors, expressed as an ice speed error over a 3-day period, are examined in detail below.

Imperfect tiepoint registration within the data grid is the largest source of error in this feature tracking technique. For small, well-defined features the maximum registration error is estimated to be one pixel for each observation. The

actual error should be uniformly distributed within the pixel. The maximum error is equivalent to a 50 km or 19.3 cm/s velocity error over a 3 day period. The geo-location error, as reported by NSIDC (1990), is 8 km for each scan. Since each pixel represents a daily averaged mean of multiple scans, the geo-location error should be somewhat smaller. For an error of 5 km, the magnitude of ice motion could vary by 3.8 cm/s over 3 days. Thus the maximum estimated position error is 30 km. If this error is assumed to be uniformly distributed, then the standard deviation of the error is 19.0 km.

The estimated velocity error due to the maximum position error is 23.1 cm/s over 3 days. This is over twice the typical ice velocity of 10 cm/s. If instead the standard deviation of the position error is considered, the velocity error reduces to 14.7 cm/s. These velocity errors decrease if the motion is averaged over longer time periods. For example, a 12 day average would result in a maximum error of 5.8 cm/s.

The ARGOS system currently used to track buoy locations can determine position accuracy within a few hundred meters (Thorndike, 1986). Assuming a maximum error of 500 m for each ARGOS reported position, the resulting velocity error over 3 days would be 0.4 cm/s.

When comparing SSM/I-derived ice trajectories with buoy locations, the velocity gradient between the two locations must be considered. These velocity gradients are the result of the ice pack response to external forces such as wind and ocean currents. Thorndike (1986) compared the velocity components of ice camps and buoys separated by distances ranging from 1 to 1000 km. He concluded that on scales of this magnitude ice behaves as a homogeneous, isotropic velocity field. Thorndike examined the correlations of buoy and ice

camp velocities as a function of distance. For a 100 km camp-buoy separation, he found the correlation to be 0.9. At a 400 km separation, the correlation drops to approximately 0.6.

Using these correlations, the variance of the differences in ice velocity between two separate points within the ice pack can be estimated. The variance of the velocity difference between the points (σ^2_{err}) is given by

$$\sigma^2_{\text{err}} = E[V(x+s) - V(x)]^2 \quad (8)$$

where E is the expected value operator and $V(x)$ and $V(x+s)$ are the ice velocities separated by some distance s . Assuming the variance of ice velocity is the same at both points, (8) reduces to

$$\sigma^2_{\text{err}} = 2\sigma^2_i(1-\rho) \quad (9)$$

where σ^2_i is the variance of the ice velocity and ρ is the correlation coefficient. Given a standard deviation of ice velocity of 10 cm/s (Thorndike, 1986) and assuming the u and v components of motion are independent of each other (the total variance then equals the sum of the variance of each component), σ^2_{err} is 40 cm²/s² and 10 cm²/s² for correlations of 0.6 and 0.9, respectively. The resulting velocity errors are 6.3 cm/s for a 400 km separation and 3.2 cm/s for a 100 km separation. These velocity errors equate to 16 km and 8 km positional errors, respectively.

Table 5 summarizes the maximum errors expected for each error source. The first three position errors are per observation. The corresponding velocity

error results from combining two position errors for each velocity calculation. Velocity errors are calculated over 3 and 12 day day intervals to show how the maximum estimated error decreases for longer mean flow calculations.

TABLE 5: SUMMARY OF MAXIMUM ERRORS

Error Source	Positional Error (km)	3 - Day Velocity Error (cm/s)	12 - Day Velocity Error (cm/s)
Tie Point Registration	25	19.3	4.8
SSM/I Geolocation	5	3.8	0.9
Buoy Position	0.5	0.4	0.1
Velocity Gradient (100 Km)	8 (3 Day)	3.2	3.2
Velocity Gradient (400 Km)	16 (3 Day)	6.3	6.3

This error analysis shows that 3 day ice motion estimates are unreliable indicators of true ice motion because the velocity error can exceed the typical true ice velocities of 10 cm/s. Longer term averages, however, reduce the impact

of the SSM/I position errors and have the potential to represent accurately general ice flow.

An expected correlation coefficient can be calculated from the maximum expected errors. This correlation can be used to validate the hypothesis that the feature tracks are representative of true ice motion. If the observed correlations are less than the expected value, then either the feature tracks do not represent true ice motion or the errors were underestimated. If the observed correlations are larger than the expected value, then the actual errors are smaller than expected.

The correlation coefficient between two quantities, x and y , is given by

$$\rho = \frac{E_{xy}}{[E_{xx} E_{yy}]^{1/2}} \quad (10)$$

where both x and y are assumed to have zero means. Let x and y be defined as the ice motion at the feature and buoy, respectively, as observed from the data:

$$x = v + \epsilon_f + \epsilon_d \quad (11)$$

$$y = v + \epsilon_b \quad (12)$$

where v is the true ice velocity, ϵ_f is the error in measuring the velocity of the feature, ϵ_d is the error due to the velocity difference between the feature and the buoy and ϵ_b is the error in measuring the velocity of the buoy. The variances due to these errors are defined as

$$\sigma_f^2 = E\epsilon_f^2 + E\epsilon_d^2 \quad (13)$$

$$\sigma_b^2 = E\epsilon_b^2 \quad (14)$$

$$\sigma_i^2 = E v^2 \quad (15)$$

where σ_f^2 is the variance caused by the feature position and velocity difference errors, σ_b^2 is the variance due to the buoy position errors and σ_i^2 is the variance of true ice velocity. The expected values in equation (10) become

$$E_{xy} = \sigma_i^2 \quad (16)$$

$$E_{xx} = \sigma_i^2 + \sigma_f^2 \quad (17)$$

$$E_{yy} = \sigma_i^2 + \sigma_b^2 \quad (18)$$

Thus the expected correlation coefficient can be defined as the variance of true ice motion divided by the square root of the variances of buoy motion and feature motion multiplied together:

$$\rho = \frac{\sigma_i^2}{[(\sigma_i^2 + \sigma_b^2)(\sigma_i^2 + \sigma_f^2)]^{1/2}} \quad (19)$$

As before, σ_i^2 for each component of motion is $50 \text{ cm}^2/\text{s}^2$. Using the 3 day sampling interval from Table 5, σ_b^2 is negligible at $0.16 \text{ cm}^2/\text{s}^2$ and σ_f^2 is the sum of the variances due to positional error ($266.8 \text{ cm}^2/\text{s}^2$) and the velocity gradient between the buoy and the feature ($39.7 \text{ cm}^2/\text{s}^2$ for 400 km and $10.2 \text{ cm}^2/\text{s}^2$ for 100 km separations). Using these values in equation (19), the expected correlation for a feature and buoy 100 km apart is 0.391. For a separation of 400 km, the correlation decreases to 0.374.

These numbers indicate that if the correlation between 3 day mean velocities determined from buoys and multiyear ice features exceeds approximately 0.4, the feature is moving with the ice and the errors associated with the tracking technique were less than expected. If the same calculations are performed for 12 day mean ice velocities, correlations rise to 0.866 and 0.783 for 100 and 400 km separations, respectively.

C. RESULTS

1. Ice Trajectories

Trajectories of the four feature - buoy pairs from the different arctic regions, each plotted at 3 day intervals, are shown in Figures 27 through 31. Because the feature tracks are limited to discrete 25 km jumps in position, periods of slow, looping or retrograde motion confuse the trajectories. In these cases, the positions have been slightly offset to show movement more clearly.

The correspondence between 3 day positions of the buoys and features appears somewhat erratic. This is probably due to the resolution limitations inherent in the SSM/I data grid. Taken over longer periods, however, the general flow corresponds quite well to the buoy positions. This is best shown in the Fram Strait trajectories (Figure 27). Both the buoy and FRAM tracks are roughly parallel as they traveled southward down the east Greenland coast, the buoy preceding FRAM by about two weeks. Of special note is the sudden surge eastward at 78°N for the feature and at 69°N for the buoy. Although separated by 9° of latitude, this surge occurred at the same time (20-23 Feb). This corresponds to a period of strong geostrophic wind flow to the northeast due to a 984 mb low centered over the northern coast of Greenland (Colony and Rigor, 1990).

2. Velocity Comparisons

For each feature - buoy pair, the u and v components of motion over each 3 day period were calculated. Buoy velocities were computed directly from their reported positions. With the exception of ESS, all multiyear feature velocities were smoothed over two positions to reduce velocity spikes resulting from the gridded data set. The ESS feature, tracked for 24 days, has only one local velocity maximum in each direction so the smoothing was not applied.

Correlation coefficients between the buoys and both smoothed and unsmoothed feature velocities are presented in Table 6. Applying a t distribution test to the smoothed velocities, all but one correlation (Franz Josef Land u component) exceed the 95% confidence level that the feature and buoy velocities were correlated. The generally high correlations are particularly surprising since the maximum error analysis indicates that correlations only as high as 0.4 should be expected for 3 day mean ice velocities. These higher than expected correlations imply that the estimated errors used in the error analysis were too large.

Specific velocity comparisons are plotted in Figures 32 through 35 and are discussed below.

a. Franz Josef Land - Buoy 1790 (Figure 32)

This is the closest spatial match-up of any feature - buoy pair investigated. The separation distance averaged 76 km over a 42 day period. The buoy trajectory shows complex motion with two separate periods of retrograde east - west movements. The SSM/I grid had trouble resolving these complicated movements, providing the lowest correlation of any velocity component: -0.069 for the unsmoothed and 0.322 for the smoothed u component. When velocities

were averaged over 12 days, the unsmoothed u component correlation improved to 0.666. Three day v correlations were 0.458 and 0.678 for unsmoothed and smoothed velocities, respectively. The higher correlations in the v direction are probably due to the slow, southward trend of the drift.

TABLE 6: MYI FEATURE - BUOY CORRELATIONS

Feature	Buoy	Correlations (3 day velocities)			
		u	v	smooth u	smooth v
ESS	1896	.791	.724	.845	.490
FJL	1790	-.069	.458	.322	.674
SZ	7048	.652	.537	.685	.455
CA	3288	.051	.501	.311	.582

b. East Siberian Sea - Buoy 1896 (Figure 33)

This pair was tracked over the shortest interval (24 days). Although separated by 320 km, it also had the highest correlations. The correlations for the unsmoothed u and v components were 0.791 and 0.724, respectively. The trajectory characteristics responsible for these high correlations were a steady northwestern drift interrupted by a strong southwesterly surge (16-19 April) large enough to be resolved within the SSM/I grid. This surge corresponded to a period of strong geostrophic wind flow to the southwest from a low in the Chukchi Sea region (Colony and Rigor, 1990).

c. Severnaya Zemlya - Buoy 7048 (Figure 34)

The feature and buoy were tracked for 75 days. The average separation distance was 420 km. Both trajectories showed a slow easterly drift culminating in a clockwise loop. Correlations for the smoothed u and v components were 0.685 and 0.455, respectively. The higher u correlation is due to the predominantly eastward movement of the feature and buoy.

d. Central Arctic - Buoy 3288 (Figure 35)

This pair was taken from the 1989 data set to represent ice motion in the central arctic region. They were tracked for 90 days at an average separation of 491 km. The smoothed u correlation was low at 0.311. The v component was much higher at 0.582. The low u correlation can be explained by the steady northerly movement of the feature. East-west velocities were generally small and not well resolved in the SSM/I data grid. Correlations for the 12 day mean velocities jumped to 0.783 and 0.776 for u and v components, respectively. The longer sampling period allowed time for the slow motion of the ice field in this region to be resolved within the SSM/I grid.

3. Position Error

The maximum estimated feature position error can be compared against the position errors calculated from the data. Solving equation (19) for σ_f^2 :

$$\sigma_f^2 = \sigma_i^2 \left(\frac{1}{\rho^2} - 1 \right) \quad (20)$$

σ_i^2 is assumed to be the same as the variance of buoy velocities and σ_b^2 is negligible compared with σ_{ice}^2 . The average variance of each buoy velocity

component is $30.08 \text{ cm}^2/\text{s}^2$ and the average correlation (ρ) between the smoothed feature and buoy velocities is 0.545.

Using equation (20) and the average variances and correlations observed from the feature track data, σ^2_f is $71.19 \text{ cm}^2/\text{s}^2$. The ice velocity difference between the buoy and feature must be taken into account because σ^2_f is the sum of the variances due to position error and the velocity difference. Substituting the average standard deviation of the buoy velocities into equation (9) and again assuming that u and v components of motion are independent of each other, the variance due to the ice velocity gradient is $12.32 \text{ cm}^2/\text{s}^2$ and $3.08 \text{ cm}^2/\text{s}^2$ for 400 km and 100 km feature-buoy separations, respectively. Taking into account the average feature-buoy separation was 326 km, nearly 17% of the observed variance can be explained by the ice velocity gradient between the feature and the buoy. The remaining variance of approximately $58 \text{ cm}^2/\text{s}^2$ equates to a 10.7 cm/s total velocity error (u and v velocity variances added together).

This velocity error is less than half of the maximum expected value of 23.1 cm/s and 72% of the standard deviation of the expected error. A 10.7 cm/s velocity error over a three day period implies close to a 15 km position error in each of the two observations used to calculate the velocity. This is less than both the maximum expected position error (30 km) and the standard deviation of this error (19 km). Possible explanations for the difference between expected and actual values include: 1) the tiepoint registration and geo-location errors are smaller than expected because the gridded brightness temperatures in the dataset are obtained by averaging information gathered from several satellite passes each day; 2) the actual ice velocity gradient between the features and buoys is smaller

than Thorndike's (1986) estimates; and 3) the standard deviation of the ice velocities is smaller than the assumed value of 10 cm/s. The latter explanation probably had the greatest influence because standard deviations of the buoy velocities only ranged from 3 to 9 cm/s. These smaller than expected standard deviations could result from the use of three day ice velocity averages which reduce the effect of short term velocity surges.

D. DISCUSSION

There is good reason to doubt the practicality of inferring sea ice motion by tracking multiyear ice concentrations from space-based passive microwave radiometers. Data resolution is poor. At 37 and 19.35 GHz (the frequencies currently used to calculate ice fractions), resolutions are 33 and 56 km, respectively. The 25 km grid resolution of the SSM/I dataset is only achieved by averaging several observations over the same spot each day. Not only does the low resolution increase the position error, it also greatly reduces the possibility of tracking individual floes. The radiometer must instead observe broad regions of anomalous radiances to create trackable features. The precision of the multiyear ice fraction algorithm is only estimated to be in the range of 13 - 25 %. Moreover, a variation of 0.04 cm in cloud liquid water content will contribute as much as 30% to the uncertainty of computed multiyear ice fractions (Cavalieri et al., 1984).

In spite of these handicaps, ice drift inferred through tracking multiyear ice features from SSM/I radiometer data corresponded quite well with ice motion as measured by in-situ buoys. Ice feature trajectories were similar to nearby buoy drift patterns. In two cases (ESS and FRAM), when high atmospheric pressure gradients caused anomalously strong wind stress on the ice pack, both the feature

and buoy exhibited similar trajectories in accordance with the forcing. Comparisons between the orthogonal velocity components of the feature and buoy motion averaged over 3 days also showed surprisingly high correlations. Instances of high correlations in one component direction but low correlations in the other can be explained by slow or oscillatory movement in the direction of the velocity component exhibiting the low correlation and are a function of the low spatial resolution of the grid.

The good results achieved above were the result of being extremely selective during the tiepoint selection process. First, all tracked features were of high multiyear ice fractions surrounded by a background of relatively low fractions. Multiyear ice is thicker than first year ice and therefore less subject to deformational and destructive processes that might obscure the characteristic radiometric signal. Second, the features were small—no more than 100 km across. This simplified the task of registering the same tiepoint in successive images. The variation of multiyear ice fraction percentages within a larger feature could preclude accurate tiepoint registration. Limiting the feature spatial extent also reduced the possibility of confusing an atmospheric disturbance with an ice feature. Third, imposing a temporal coherence requirement of 18 days ensured that the tracked object was not a result of random brightness temperature fluctuations in the ice cover. Finally, limiting the record to the winter season reduced the possibility of surface melt conditions contaminating radiances from the sea ice. Another benefit of the winter season is that moisture-laden clouds with their contaminating effects are generally restricted to the open ocean and the marginal ice zone areas.

The number of trackable features was limited. The abovementioned limitations restricted the number of suitable features to only a dozen or so during the winter season. Relaxing these restrictions should produce more trackable features (and possibly introduce spurious features) and is an area suitable for further research. Development of an objective scheme to identify and track features should also increase the number of available datapoints.

Despite the above restrictions, this limited ability to observe and track areas of anomalous multiyear ice fractions can be useful for arctic studies. Ice fluxes from the central arctic have been shown to be the largest exporter of fresh water from the Arctic Ocean and the largest freshwater input to the Greenland Sea (Aagaard and Carmack, 1989). Available databases, extending back to 1978, can be used to assess the intra and interannual variability of ice transport. Researchers can identify previous, and possibly forecast future, pulses of ice types to examine their influence on regional heat and salinity budgets. Ice camps are generally located on relatively smooth, thick floes of multiyear ice for logistical and safety reasons. Potential sites are currently scouted by aircraft. This space-based technique offers the possibility of remotely identifying sites well in advance of deployment. As satellite instrumentation improves and emanations from higher microwave frequencies are utilized, surface resolution will also improve resulting in increased reliability of short term ice velocity vectors.

E. CONCLUSIONS

When images of arctic multiyear ice fractions calculated from winter season SSM/I data are examined in sequence, distinct features are observed to move in the general direction of climatological ice flow. These features exist throughout the arctic basin but are mainly located in regions where first year and multiyear

ice merge together. Some features are short-lived, others can be tracked throughout the data record.

Four of these multiyear ice features from the winters of 1988 and 1989 were compared against nearby arctic buoy trajectories. Three day average ice velocity vectors were found to correlate well with the buoy velocities; the average smoothed velocity correlation was 0.545. The maximum estimated velocity errors, mainly due to the low data resolution, are double a typical ice velocity of 10 cm/s making short-term ice motion calculations unreliable. Actual velocity errors derived from the feature-buoy correlations are half the maximum estimated error and less than three quarters of the standard deviation of this error. This difference is probably due to the smaller than estimated variances of ice motion because the ice motion is averaged over a three day period, smoothing out short-term ice velocity surges.

The higher than expected correlations between multiyear ice feature velocities and arctic buoys are due to the stringent requirements established for feature selection. Relaxing these requirements could substantially increase the number of trackable features from the dozen or so noted in the winter of 1988 but also decrease the confidence that tracked features accurately represent ice motion. A similar increase in trackable features could probably be attained by objectively scanning the dataset for subtle features that were not recognized through a subjective analysis of the data.

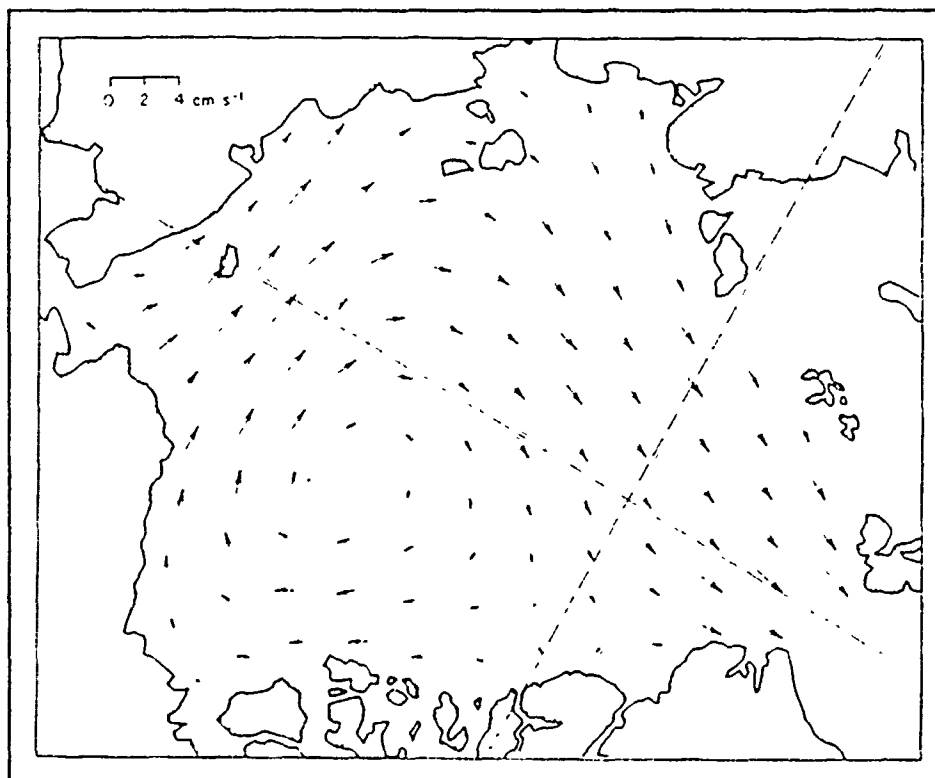


Figure 22 Field of mean ice motion (from Colony and Thorndike, 1984).

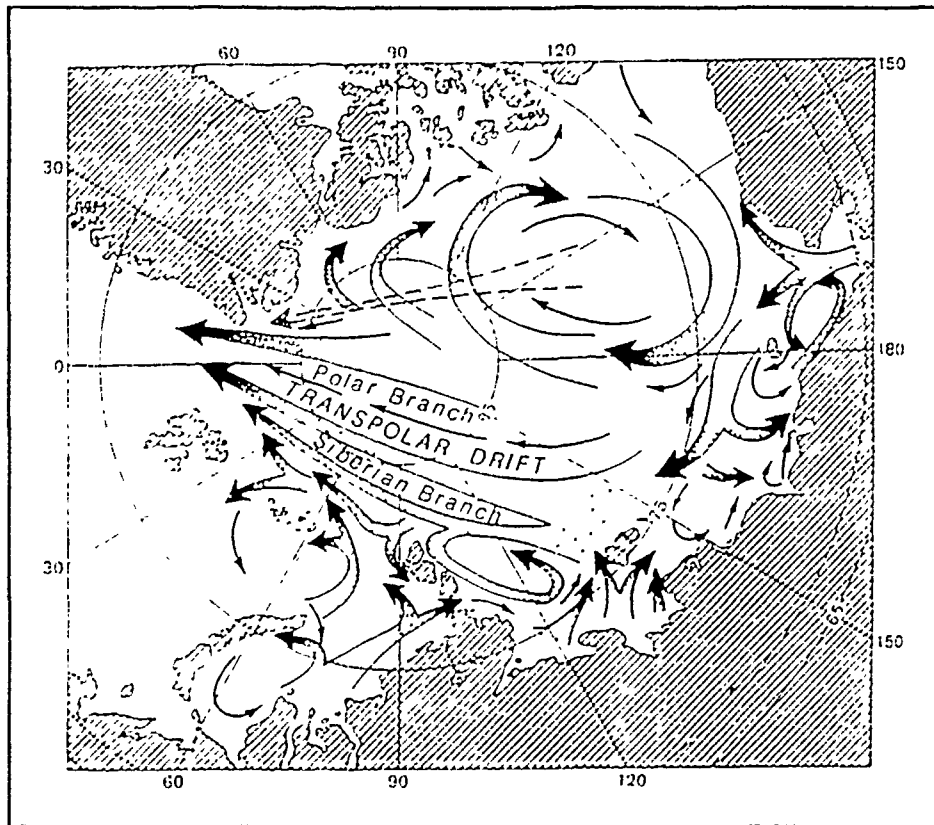


Figure 23 Average sea ice drift showing the two components of the Transpolar Drift Stream (from Polarstern Scientific Party, 1988).

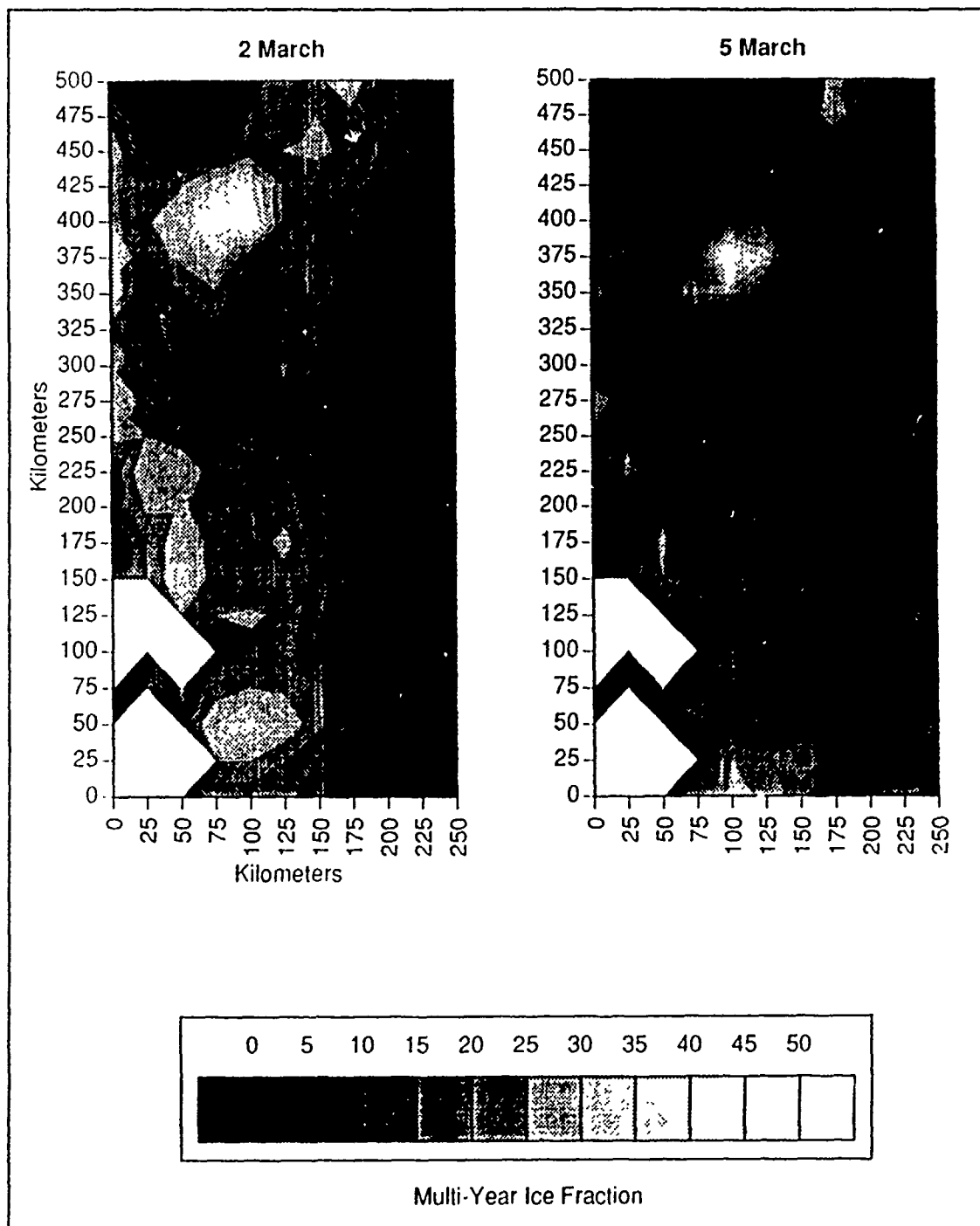


Figure 24a Contour plots showing advection of multiyear ice feature along the east Greenland coast. Images from 2 and 5 March, 1988. Plots are centered at 76.1°N, 13.5°W. The feature moves from the upper left to the lower right corner.

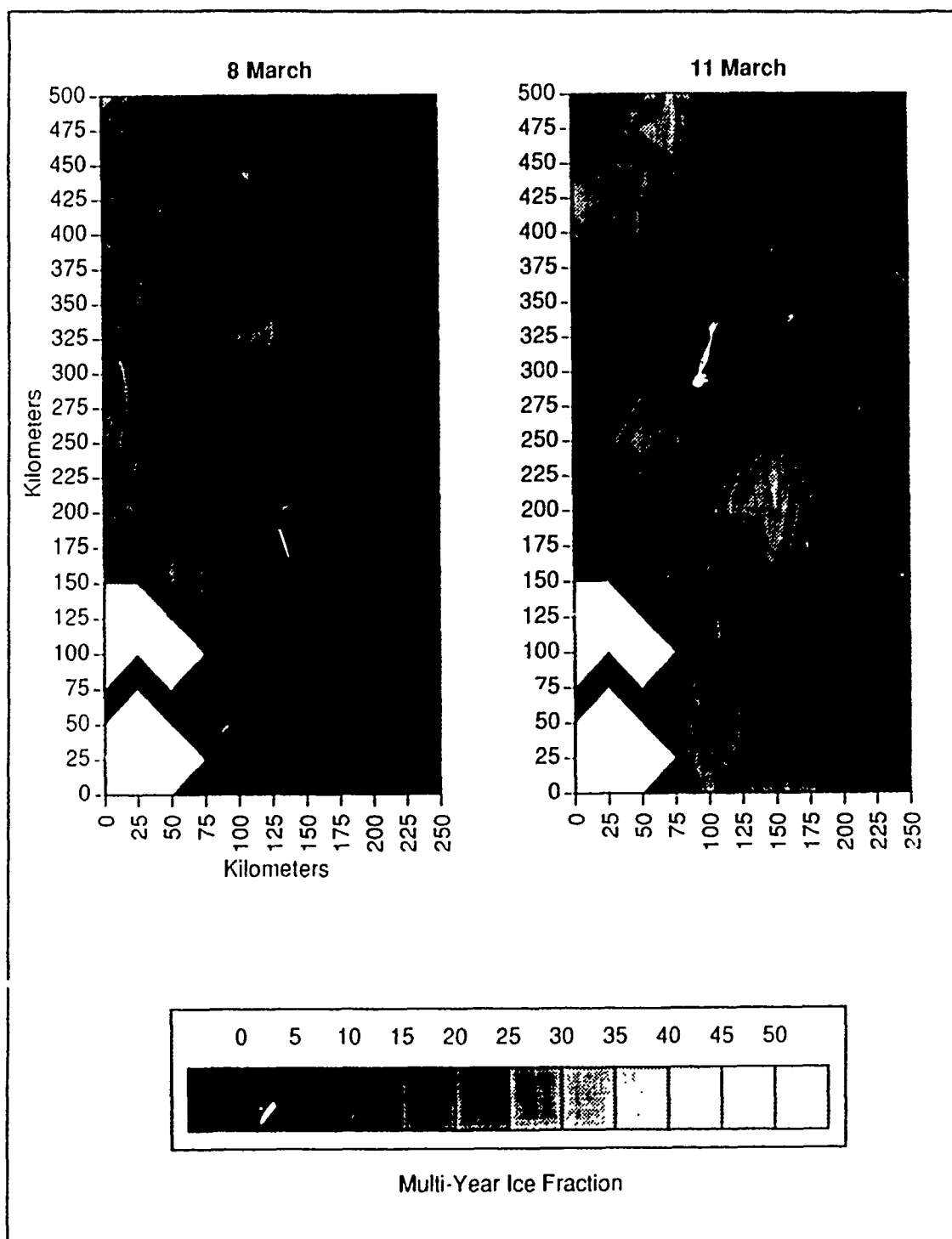


Figure 24b Same as Figure 24a except images are from 8 and 11 March, 1988.

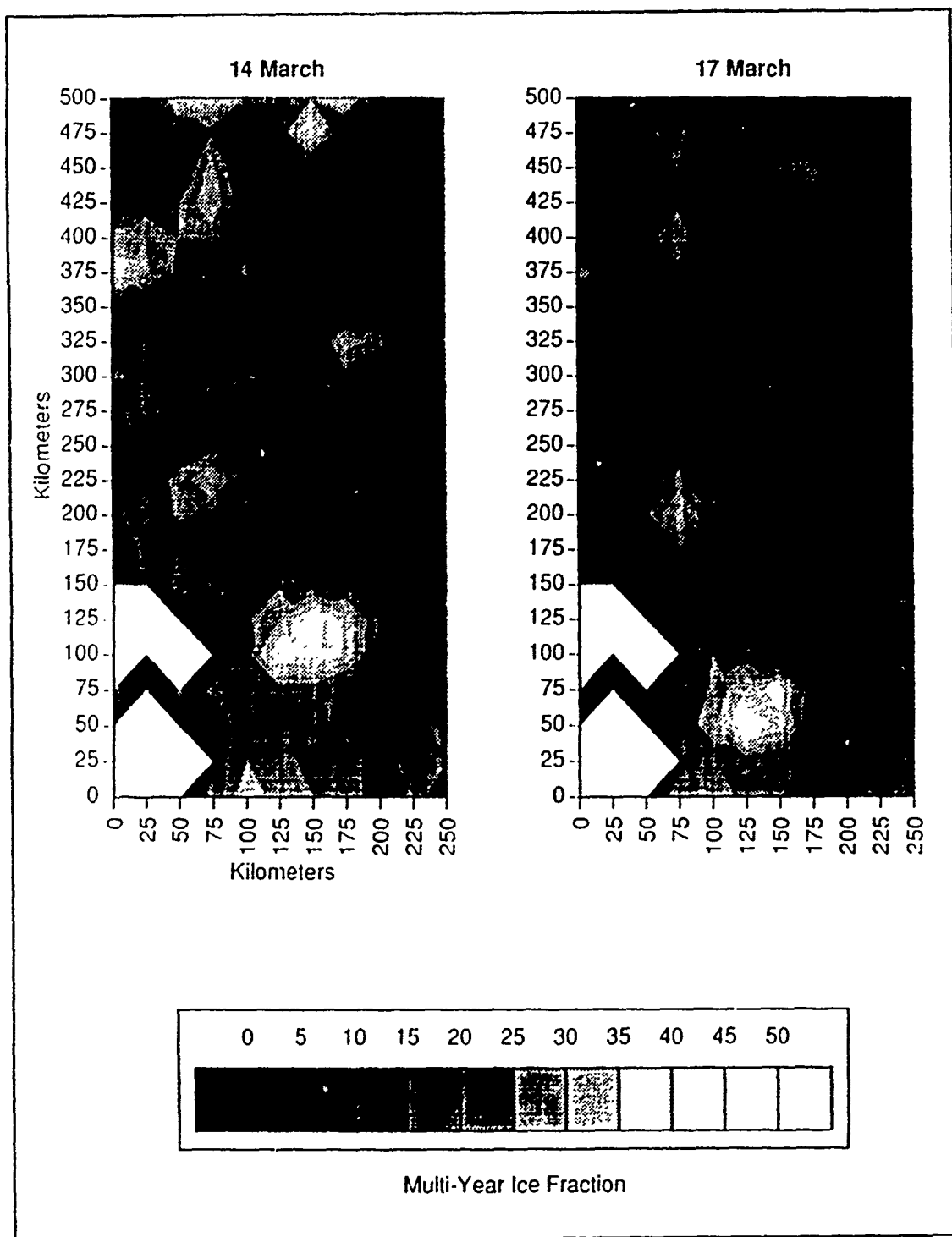


Figure 24c Same as Figure 24a except images are from 14 and 17 March, 1988.

		Kilometers										
Kilometers		0	25	50	75	100	125	150	175	200	225	250
	500	13	6	9	17	18	22	23	30	17	10	9
	475	19	12	12	20	20	23	25	23	21	12	9
	450	24	13	11	16	21	25	26	24	19	16	12
	425	24	21	24	33	42	25	22	23	17	15	13
	400	25	24	29	45	(47)	25	18	21	15	14	12
	375	30	22	26	34	21	24	23	18	16	10	11
	350	31	14	19	24	15	15	22	17	14	9	8
	325	17	12	18	19	17	15	16	14	13	10	4
	300	25	20	16	15	13	21	14	10	11	6	2
	275	31	23	19	16	17	18	13	11	8	5	6
	250	27	25	23	19	20	18	12	10	8	8	8
	225	16	30	28	23	23	21	16	9	5	5	9
	200	17	26	26	21	23	27	17	10	6	5	9
	175	8	20	29	23	21	27	18	6	6	14	8
	150	13	20	30	23	19	23	19	7	4	8	8
	125	LAND	LAND	25	25	26	24	16	6	2	0	0
	100	LAND	14	LAND	22	23	23	13	8	5	0	4
	75	11	15	17	22	25	24	21	13	4	0	7
	50	15	LAND	18	30	37	29	21	14	9	2	6
	25	LAND	12	LAND	25	25	20	14	10	7	6	11
	0	20	LAND	11	16	16	17	11	12	11	1	11

3 March 1988

		Kilometers										
Kilometers		0	25	50	75	100	125	150	175	200	225	250
	500	9	10	11	20	7	6	6	28	21	0	4
	475	11	2	0	4	3	9	13	31	17	0	1
	450	18	10	4	14	14	14	13	12	8	0	3
	425	22	11	3	12	11	14	16	17	8	3	0
	400	21	15	16	8	21	22	13	15	12	6	1
	375	23	27	19	21	(49)	39	9	8	9	5	0
	350	29	17	17	31	32	21	9	8	7	1	0
	325	18	6	16	16	1	5	16	12	4	3	0
	300	19	12	7	10	11	6	8	6	1	0	0
	275	28	22	15	9	12	7	10	5	0	0	0
	250	24	24	18	13	8	10	11	3	1	0	0
	225	16	26	23	15	8	13	11	5	0	0	0
	200	12	21	23	17	15	16	11	4	0	0	0
	175	8	16	26	21	18	16	13	12	2	1	0
	150	12	18	25	16	13	20	17	9	4	4	5
	125	LAND	LAND	20	15	13	19	15	5	9	6	4
	100	LAND	11	LAND	14	15	15	15	7	8	5	3
	75	11	14	16	18	20	15	16	6	8	6	6
	50	14	LAND	11	15	12	17	14	7	7	7	7
	25	LAND	9	LAND	9	25	21	25	16	8	7	8
	0	14	LAND	11	19	27	24	16	7	10	12	9

5 March 1988

Figure 25a Pixel values for multiyear ice contour plot shown in Figure 24a. Circled value is tiepoint registration location.

		Kilometers										
Kilometers		0	25	50	75	100	125	150	175	200	225	250
	500	29	18	15	9	6	4	0	0	0	3	0
	475	20	13	15	12	2	0	0	11	9	2	0
	450	17	6	6	5	0	3	4	20	13	3	0
	425	19	9	2	6	2	8	8	10	5	0	0
	400	22	15	5	8	11	8	10	7	4	0	0
	375	21	21	10	8	5	8	11	11	6	0	0
	350	23	22	14	12	15	23	12	8	6	0	0
	325	20	19	10	15	26	28	7	4	3	2	0
	300	19	14	9	14	19	13	6	6	1	0	0
	275	20	18	8	8	8	7	5	7	1	0	0
	250	23	19	14	8	7	6	0	0	0	0	0
	225	14	21	20	11	6	7	2	0	0	0	0
	200	13	24	23	17	10	8	3	2	0	0	0
	175	4	13	22	20	12	9	5	6	0	0	0
	150	5	14	20	21	15	12	5	2	0	0	0
	125	LAND	LAND	16	17	12	11	7	4	0	0	0
	100	LAND	7	LAND	11	14	14	9	3	0	0	0
	75	10	10	9	12	11	11	12	6	1	0	0
	50	10	LAND	12	11	9	14	9	7	0	0	0
	25	LAND	10	LAND	7	11	12	9	3	0	0	0
	0	10	LAND	3	10	15	10	5	0	0	0	0

8 March 1988

		Kilometers										
Kilometers		0	25	50	75	100	125	150	175	200	225	250
	500	10	13	23	31	23	8	8	9	11	0	0
	475	15	19	30	33	12	6	11	12	12	3	0
	450	21	24	27	29	21	16	12	5	8	7	1
	425	36	30	26	20	23	17	13	11	12	12	6
	400	26	27	25	14	18	16	11	21	15	11	8
	375	19	17	18	22	17	13	12	22	18	11	20
	350	18	18	14	22	14	10	14	15	12	11	11
	325	22	21	13	11	12	10	16	19	14	10	6
	300	20	23	22	11	11	12	14	19	18	12	4
	275	15	21	26	21	12	14	14	17	17	14	5
	250	6	23	33	27	17	16	24	21	16	13	8
	225	14	22	25	19	19	26	37	24	11	9	10
	200	15	22	21	19	19	30	35	21	10	5	7
	175	7	14	18	21	19	20	32	19	9	9	9
	150	5	16	17	21	23	20	20	9	9	11	5
	125	LAND	LAND	18	18	22	16	15	6	5	7	9
	100	LAND	9	LAND	19	22	17	19	12	8	3	5
	75	14	10	12	17	23	19	21	11	7	10	3
	50	11	LAND	14	17	24	20	15	16	3	4	5
	25	LAND	11	LAND	19	23	19	18	15	8	6	4
	0	12	LAND	5	15	20	18	20	16	11	9	4

11 March 1988

Figure 25b Pixel values for multiyear ice contour plot shown in Figure 24b. Circled value is tiepoint registration location.

		Kilometers										
Kilometers		0	25	50	75	100	125	150	175	200	225	250
		10	12	30	31	25	18	24	30	19	12	4
500		10	8	20	24	22	20	37	19	14	9	0
475		8	11	18	32	17	10	16	11	9	4	1
450		14	21	25	35	20	5	10	14	5	8	6
425		28	30	25	26	22	15	14	12	5	9	3
400		32	31	24	17	26	20	14	3	3	7	7
375		19	17	23	18	15	17	11	11	13	11	6
350		18	20	16	16	18	14	14	33	29	11	8
325		21	21	14	21	24	13	13	23	15	14	11
300		14	21	19	21	15	6	7	13	12	14	10
275		8	14	20	23	16	7	8	15	15	15	10
250		16	20	27	36	24	8	11	13	14	18	15
225		12	22	26	24	20	11	13	18	14	13	14
200		8	17	20	21	16	17	16	15	19	14	10
175		7	17	21	20	21	24	17	18	18	16	10
150		LAND	LAND	17	19	24	30	43	34	19	14	14
125		LAND	10	LAND	15	23	40	42	34	18	13	11
100		16	15	16	21	24	23	21	13	11	12	8
75		14	LAND	15	17	23	21	17	13	11	14	16
50		LAND	11	LAND	17	25	21	19	19	11	19	15
25		14	LAND	6	17	29	22	20	18	12	16	13
0												

14 March 1988

		Kilometers										
Kilometers		0	25	50	75	100	125	150	175	200	225	250
		4	0	7	16	15	16	14	6	6	7	5
500		4	9	24	27	19	19	15	14	5	6	7
475		3	6	21	25	22	19	25	28	17	10	7
450		5	11	19	23	18	18	24	23	19	8	4
425		17	20	22	30	18	7	15	15	16	10	4
400		33	26	22	23	11	4	13	9	11	10	5
375		24	26	19	16	20	21	12	5	4	8	2
350		18	18	21	13	18	18	10	0	0	9	2
325		18	18	16	15	10	8	11	7	6	6	6
300		18	20	14	19	23	11	16	21	9	7	5
275		9	16	13	23	20	10	9	18	17	7	5
250		16	21	16	26	19	4	2	7	10	8	5
225		19	22	23	37	25	9	0	6	7	10	9
200		9	21	22	24	15	6	4	5	7	5	8
175		12	19	24	19	10	9	12	5	11	13	7
150		LAND	LAND	21	19	16	13	11	10	7	14	13
125		LAND	11	LAND	17	25	23	10	9	9	10	9
100		16	15	15	21	26	35	44	20	11	12	11
75		20	LAND	15	21	29	45	38	18	13	15	14
50		LAND	12	LAND	20	21	22	19	13	10	14	13
25		16	LAND	10	24	25	17	15	14	8	14	14
0												

17 March 1988

Figure 25c Pixel values for multiyear ice contour plot shown in Figure 24c. Circled value is tiepoint registration location.

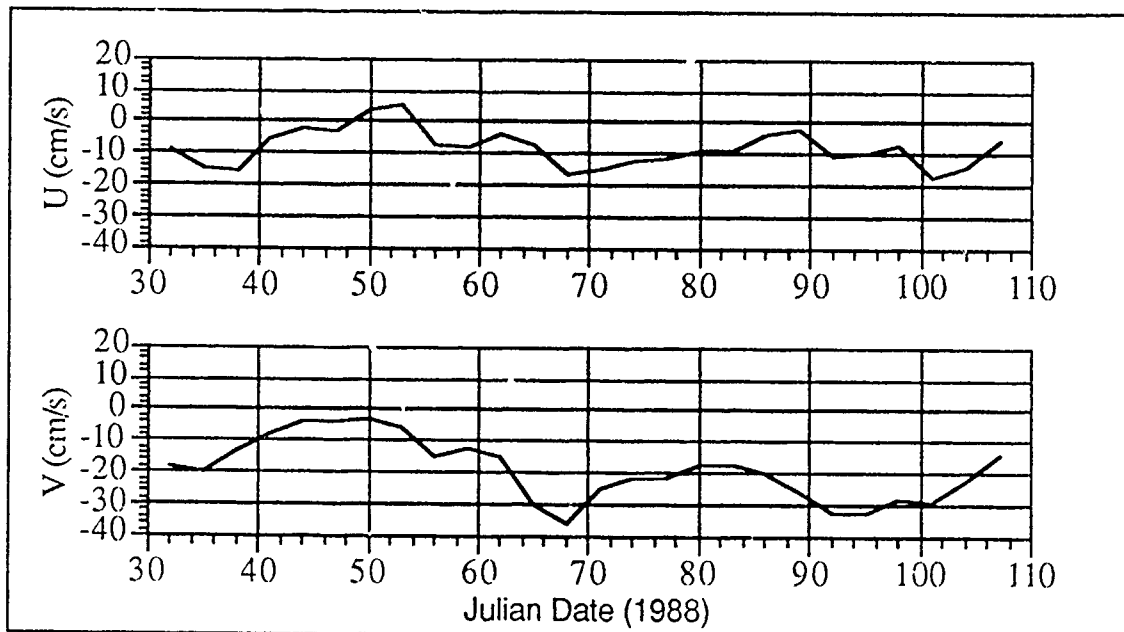


Figure 26 Ice velocities for Fram Strait feature (1 February - 22 April, 1988).

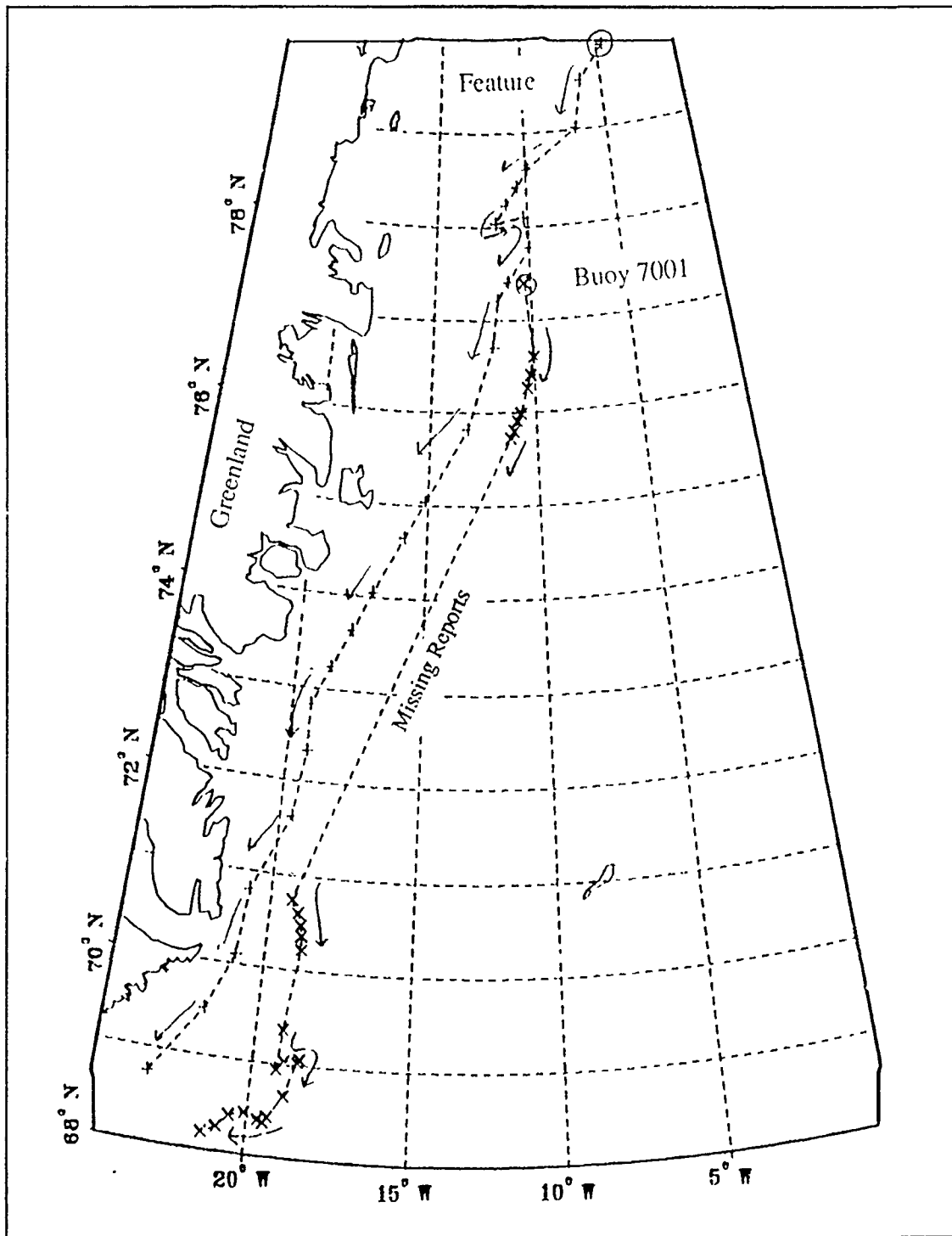


Figure 27 Ice trajectories: Fram Strait feature and Buoy 7001 (1 February - 22 April, 1988). Circled points are initial positions.

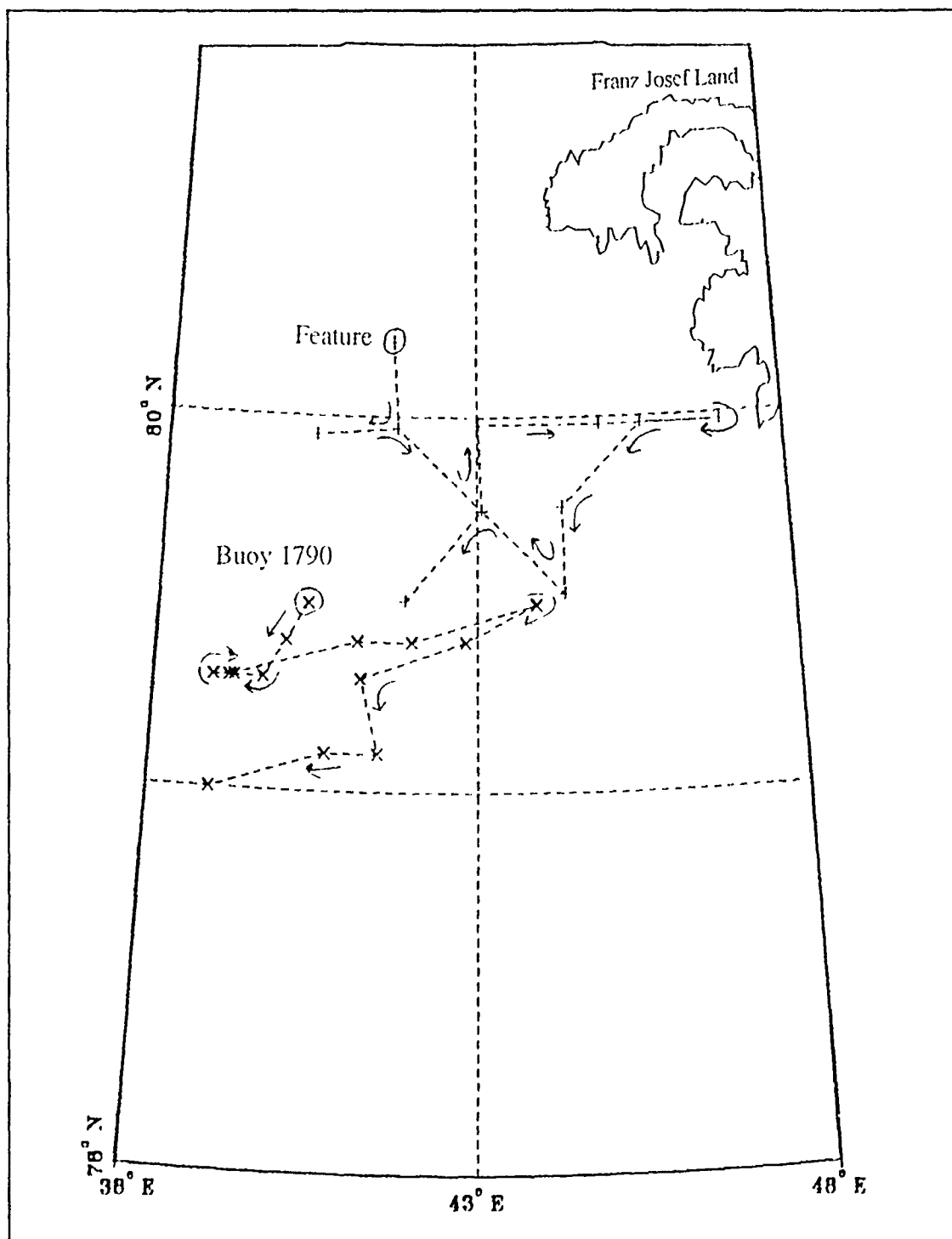


Figure 28 Ice trajectories: Franz Josef Land feature and Buoy 1790 (1 February. - 14 March, 1988). Circled points are initial positions.

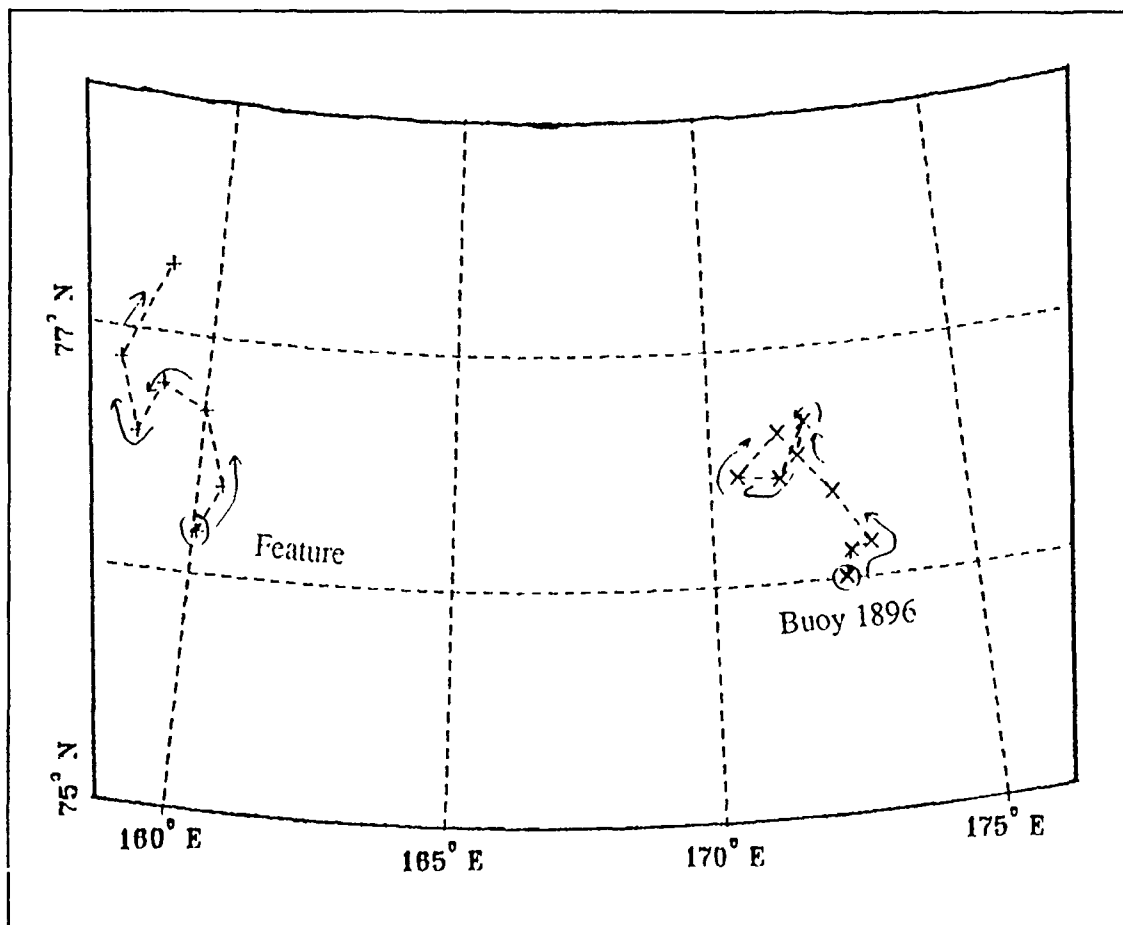


Figure 29 Ice trajectories: East Siberia Sea feature and Buoy 1896 (1 - 25 April, 1988). Circled points are initial positions.

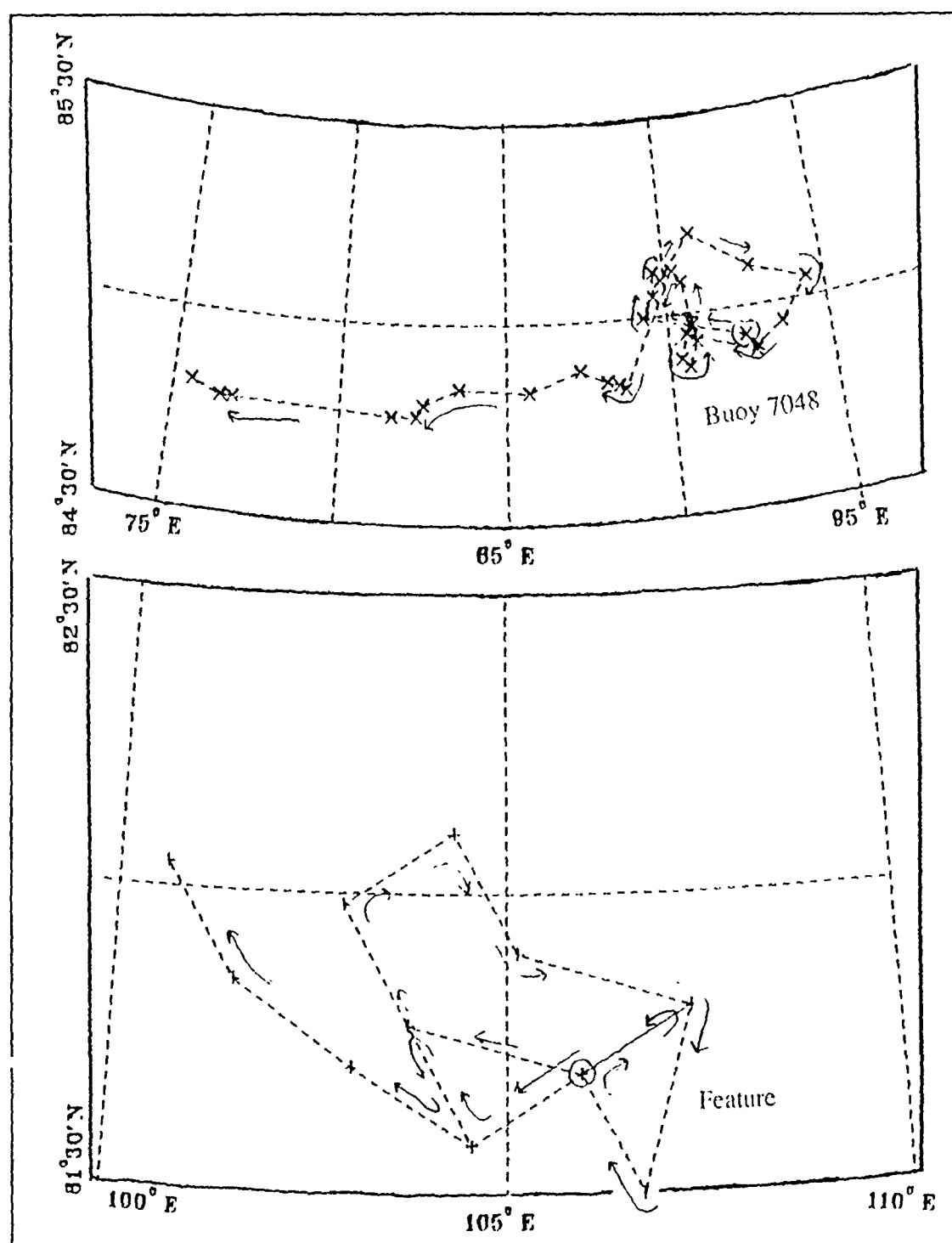


Figure 30 Ice trajectories: Severnaya Zemlya feature and Buoy 7048 (1 February - 28 April, 1988). Circled points are initial positions.

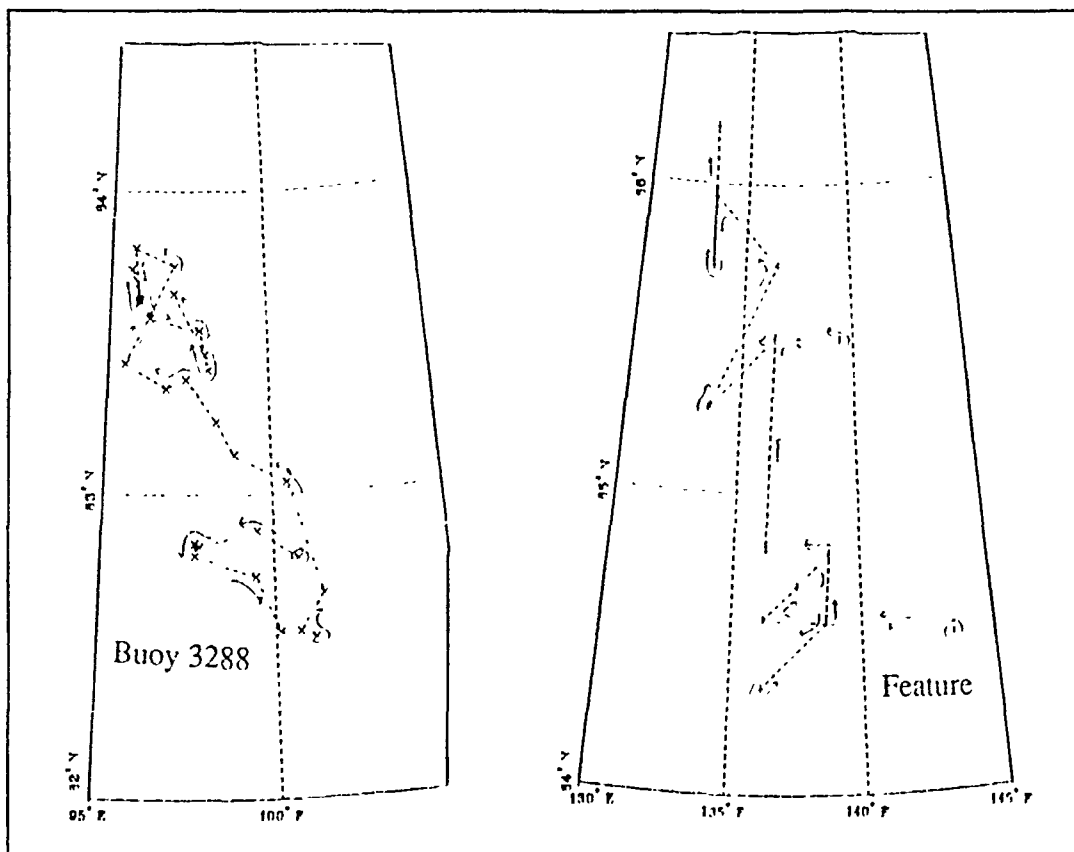


Figure 31 Ice trajectories: Central Arctic feature and Buoy 3288 (1 January - 31 March, 1988). Circled points are initial positions.

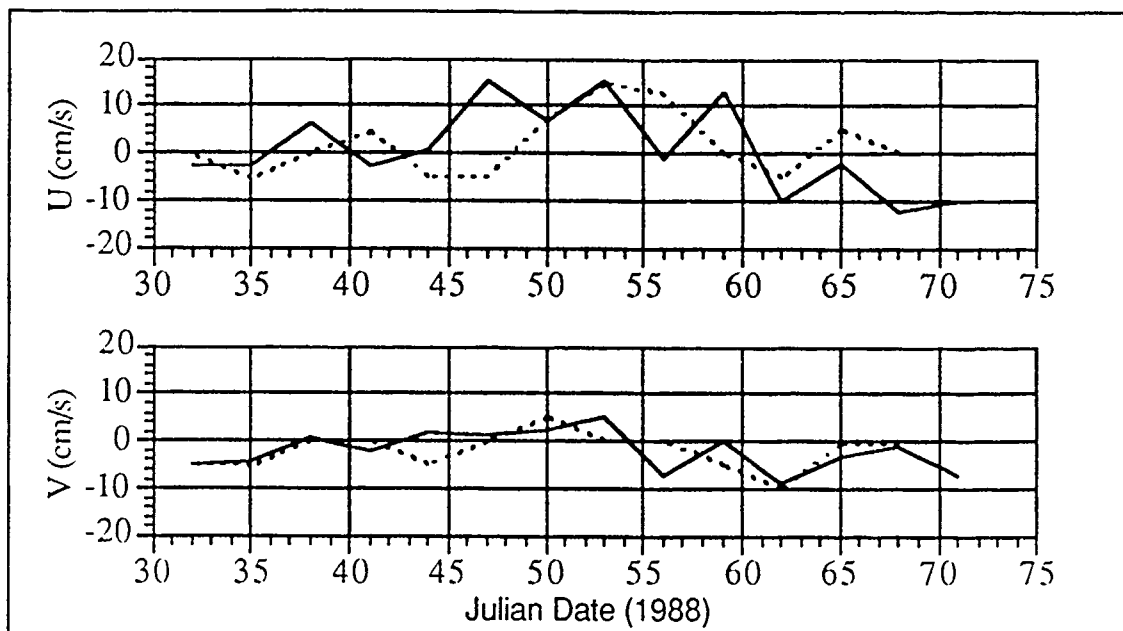


Figure 32 Franz Josef Land and Buoy 1790 velocity comparison. Buoy is solid line, feature is dashed line.

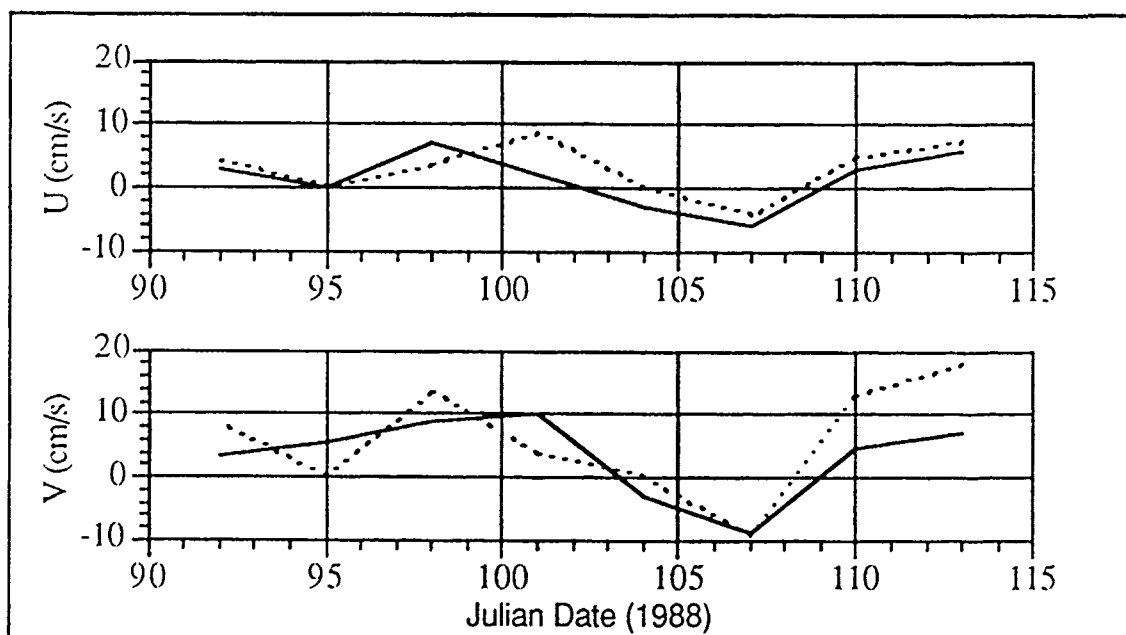


Figure 33 East Siberian Sea and Buoy 1896 velocity comparison. Buoy is solid line, feature is dashed line.

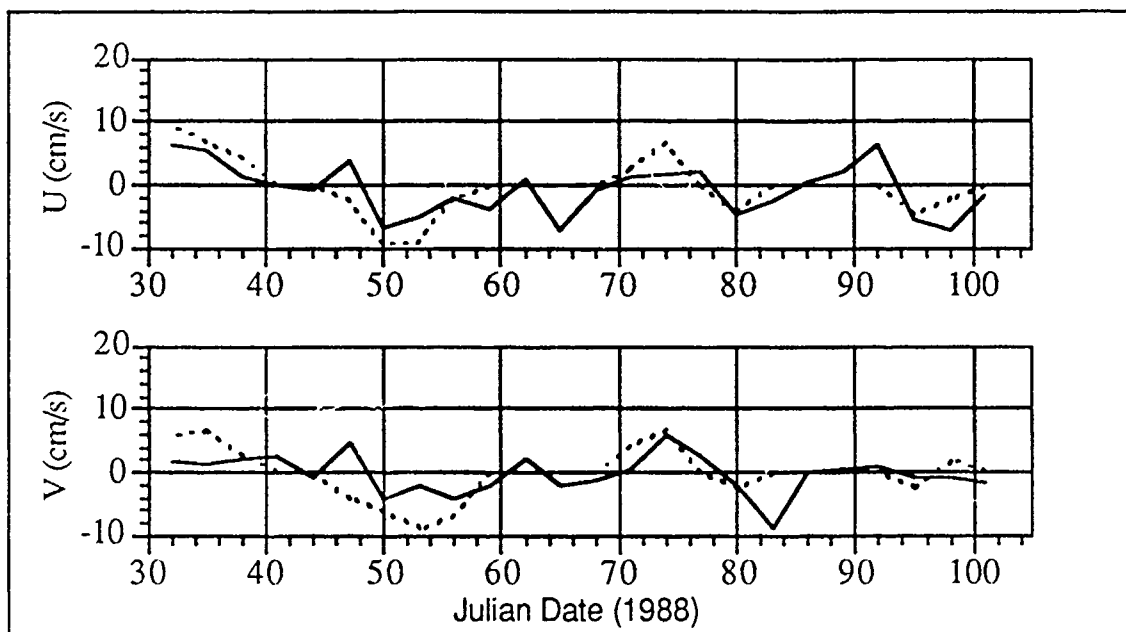


Figure 34 Severnaya Zemlya and Buoy 7048 velocity comparison. Buoy is solid line, feature is dashed line.

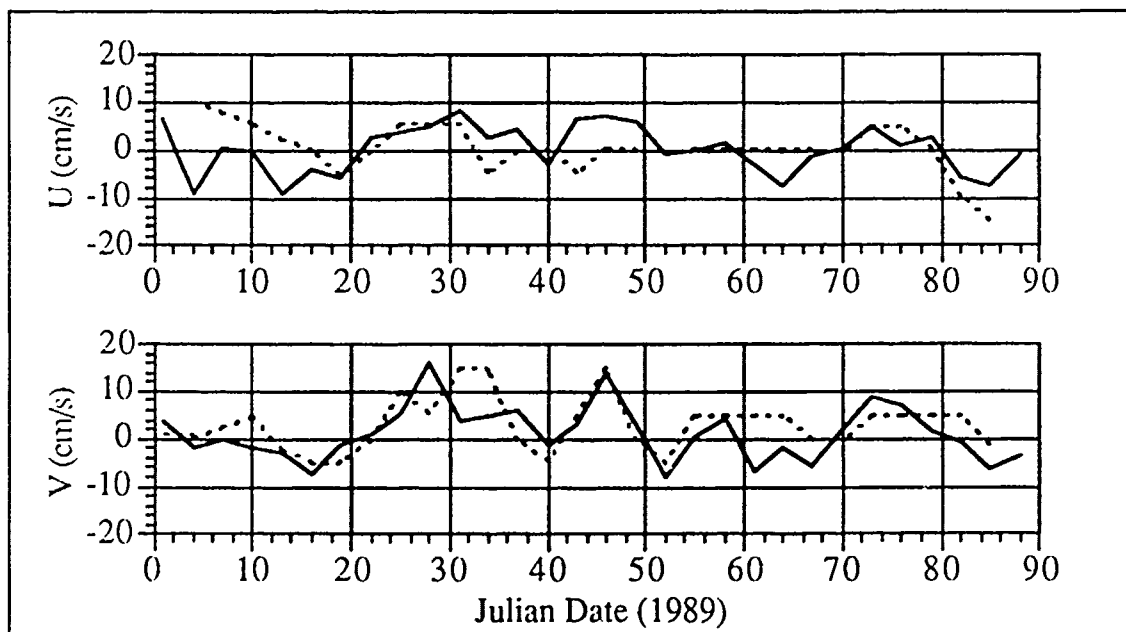


Figure 35 Central Arctic and Buoy 3288 velocity comparison. Buoy is solid line, feature is dashed line.

V. CONCLUSIONS AND RECOMMENDATIONS

Arctic sea ice conditions are an important component of the global climate system. The sea ice cover affects the Earth's radiative balance by influencing the heat flux between the ocean and atmosphere and heat transport between the lower and upper latitudes. Passive microwave remote sensing of sea ice offers continuous, all-weather observations of these remote areas independent of solar illumination. This is particularly important in the arctic where much of the region is shrouded by clouds or covered in darkness.

Accurate ice observations using passive microwave remote sensing techniques require knowledge of the radiative characteristics of sea ice. The radiative properties of sea ice are complicated due to its complex nature which is determined by formation environment, age and season. Other complicating factors include contamination from moisture-laden clouds and the presence of snow cover, melt ponds and ridging. In spite of these difficulties, emissivity differences between sea ice and water at various microwave frequencies can be exploited to estimate ice characteristics. Current algorithms use polarization and gradient ratio differences to estimate ice concentrations and type.

Historical SSM/I data are readily available on CD-ROM media distributed by NSIDC. Two applications of this dataset to arctic sea ice studies were examined. Data from 1 February to 15 October 1988 were used to associate anomalous diurnal tidal currents over the Yermak Plateau with ice morphology. Data from 1 February to 28 April 1988 and 1 January to 31 March 1989 were used to explore the possibility of determining sea ice motion by tracking advection of multiyear ice features. Software supplied by NSIDC were modified to compute and display

the requisite ice concentration, gradient ratio and multiyear ice fraction calculations and imagery on a Macintosh II desktop computer.

The hypothesized ice concentration/morphology changes induced by the anomalously strong diurnal tidal currents observed over the Yermak Plateau could not be verified by the SSM/I data. Either the currents do not affect the ice cover or SSM/I limitations obscure the ice signatures of the currents. The low spatial resolution and susceptibility to melt and snow contamination of passive microwave emissions prevent a definitive assessment of tidal current effects on ice cover in this region.

Distinct multiyear ice features are observed to move in the general direction of the mean ice flow. Feature movement correlates well with ice motion as measured by arctic data buoys. The subjective nature of the feature tracking technique and its reliability on 'features of opportunity' prevent wide scale application throughout the arctic region. Positional errors resulting from low data resolution could make short term ice motion calculations unreliable. Long term averages, however, are reliable and can be used to augment our knowledge of general ice flow. For example, motion vectors can be used to estimate the interannual variability of ice transport through the Fram Strait and aid our understanding of heat and salinity budgets in the Greenland Sea. In spite of the limitations, tracking multiyear ice features can be a useful method of discerning continuous, all-weather ice motion from satellite data.

Further attempts to verify anomalous diurnal currents over the Yermak Plateau using SSM/I data are not recommended. The data resolution is too low to observe small scale changes of sea ice concentration or morphology. Feature tracking, however, does show some promise. Conversion of the subjective

technique described here to an objective scheme for computer analysis would greatly reduce the time and effort required for tie point selection and registration, and probably increase the number of tie points suitable for tracking. Exploration of the higher spatial resolutions afforded by 85.5 GHz data would greatly increase the reliability of ice motion vectors.

APPENDIX A

This appendix contains FORTRAN source code listings of software used to process the dataset contained on the NSIDC CD-ROM disks.

<u>Program</u>	<u>Page</u>	<u>Purpose</u>
ssmiice	89	Computes ice concentrations from SSM/I brightness temperature values on the NSIDC CD-ROM dataset.
locate	95	Transforms I, J coordinates of the NSIDC SSM/I polar grids to latitude and longitudes coordinates and vice versa.
u,v calc	102	Calculates u and v components of motion from a list of user specified geodetic latitude and longitude positions.
<u>Subroutine</u>	<u>Page</u>	<u>Purpose</u>
usetie	105	Computes coefficients for the ice algorithm in ssmiice using NASA-approved tiepoints.
ice25	108	Computes ice concentrations from NSIDC CD-ROM data at 25 km grid resolution.

```

program ssmiice
cccccccccccccccccccccccccccccccccccccccccccccccccccccccccccc
c
c SSMIICE - This program computes ice concentrations from SSMI TB
c   grids residing on CD-ROM.
c
c   Inputs
c
c   USER DEFINED
+++++
c
c
c   drive : Name of CD-ROM disk
c
c   indate : Date in the format YYMMDD (eg., 870710)
c           From this variable the CD-ROM is searched for the
c           appropriate filename. The filename for the ice
c           concentration algorithm is derived from this
c           variable.
c
c   them : Defines the appropriate hemisphere to apply this
c          algorithm (1=North, 2=South)
c
c   icepar : Defines the type of ice concentrations to derive:
c            1=total, 2=multi-year, 3=first-year.
c
c   INTERNAL
+++++
c
c   infile : The path, name, and descriptor string describing
c            the data file from which the SSMI Tb data will be
c            extracted from the CD-ROM. User must specify appropriate
c            filepath.
c
c   buff : Input buffer containing the SSMI Tb data read from
c          the CD-ROM. Two lines of SSMI TB grid data will
c          read with a single IO request.
c
c   mask : Landmask used in computing the 25 km
c          ice concentration grid.
c
c   idim1 : Number of parameters in an SSM/I Tb grid cell
c
c   idim2 : Number of cells in the SSM/I Tb grid line
c
c   idim3 : Number of grid lines in an SSM/I Tb grid
c
c   grdtyp : Three character descriptor designating the grid type
c            to access from the CD-ROM (N3B or S3B)

```

```

c   icetyp : Three character descriptor designating the extension
c           for the resultant ice parameter image (N3C or S3C).
c
c   c       : Array of tiepoint coefficients. Returned from USETIE
c           and used in GETICE. Refer to NODS Handbook Appendix
c           CC pp 23-24.
c
c   Outputs
c
c   INTERNAL
c   ++++++
c
c   outfil : The name and descriptor string which reference
c           the data file which will be used to store the
c           ice concentration grid. This string is computed
c           internally from the variables, indat and grdtyp. The
c           file will be created in the default directory.
c           Program will abort if file currently exists!
c
c           The file dimensions will be 304 1-byte cell values
c           with 448 grid lines for the grid type 'N3C' and
c           316 1-byte cell values with 332 grid lines for the
c           grid type 'S3C'.
c
c   ice     : Output buffer containing the computed ice
c           concentrations for the 25 km total ice concentration
c           grid. Totice is 316 bytes in length which corresponds
c           to the length of an S3C raster line.
c
c   Vince Troisi
c   5/3/1989
c
c   1/4/1989 - Modified for SSM/I CD-ROMs
c   7/1/91 - Modified for Apple Macintosh and 25 km grid by W. A. Wright
c   ccccccccccccccccccccccccccccccccccccccccccccccccccccccccccc
c       integer idim1, idim2, idim3
c
c   There are five channels in the N3B or S3B grid cells
c
c       parameter (idim1 = 5)
c       parameter (maxlen = 316)
c
c       integer iunit, ounit, munit, olen,z
c       integer ymd(6), ier, recln,ok
c
c       character * 3 grdtyp, icetyp
c       character * 9 drive
c       character * 2 year, month, day
c       character * 6 indat(95), ifile
c       character * 3 mon(12)
c       character *80 outfil,infile, mfile

```

```

integer * 2 buff(maxlen*idim1),abyte,bbyte
integer * 1 ice(maxlen) , mask(maxlen),atemp(2),btemp(2)
real      c(12)
equivalence (bbyte,btemp)
equivalence (atemp,abyte)
data mon
+  /'JAN','FEB','MAR','APR','MAY','JUN','JUL','AUG','SEP',
+  'OCT','NOV','DEC'/

```

C=====

c Query user for search criteria

c Query for name of CD-Rom drive

```

print *, 'Name of CD-Rom?'
read (*, '(a)') drive

```

c Query user for file dates

```

5  print *, 'Number of files to create? (95 max)'
   print *, 'Note: Read lasts approx. 10 min. per file'
   read *, n

```

```

c  print *, 'Enter file dates (yymmdd).'
   open (unit=29, file='Archs HardDisk:THESIS:daylist',
+       status='old')
   do 10 i=1,n
     read (29,'(a)') indate(i)

```

```

10  continue

```

```

   print *, 'These are the selected dates:'
   do 20 i=1,n
     print *, indate(i)

```

```

20  continue

```

```

   print *, 'OK? (1=yes, 2=no, 3-stop) <ret>'
   read *, ok

```

```

   if (ok.eq.2) go to 5
   if (ok.eq.3) go to 6000

```

c Query user for appropriate polar region

```

   print *, '
   print *, 'Select one of the polar regions:'
   print *, '1. North'
   print *, '2. South'
   print *, 'Enter 1 or 2:'
   read *, ihem

```

c Query user for ice type to compute

```
print *, '
print *, 'Select type of ice characteristic to derive:'
print *, ' 1. Total Ice Concentration'
print *, ' 2. Multi-Year Ice Concentration'
print *, 'Enter 1 or 2:'
read *, icepar
```

c Combine responses to form filenames and paths and to define
c IO constants

```
if (ihem.eq.1) then
  grdtyp = 'N3B'
  icetyp = 'N3C'
  lrec = 3040
  idim2 = 304
  idim3 = 448
  npar = idim1*idim2
else
  grdtyp = 'S3B'
  icetyp = 'S3C'
  lrec = 3160
  idim2 = 316
  idim3 = 332
  npar = idim1*idim2
endif
```

```
do 5000 z=1,n
  ifile = indat(z)
  read (ifile(3:4),'(i2)')mm
```

```
infile=drive//'://grdtyp//':19//ifile(1:2)//'://mon(mm)//
+ '://ifile(1:6)//'://grdtyp//':1'
```

```
print *, 'infile = ', infile
```

c Open brightness temperature file on CD

```
iunit = 21
open (unit=iunit,file=infile,status='old',access='sequential',
+ form='unformatted',recl=lrec,iostat=ierr)
if (ierr.ne.0) then
  print *,infile, ' not accessible! <ret>'
  pause
  stop
endif
```

c Construct output file name and open the file.

```
outfil = 'Archs HardDisk:THEESIS:Conc Data://ifile(1:6)//  
+       '//ice:typ  
print *, 'output file = ',outfil  
ounit= 22  
open (unit=ounit,file=outfil,status='new',recl=idim2,  
+ iostat=ierr,form='unformatted', access='sequential')  
if (ierr.ne.0) then  
    print *,'Error opening file ',outfil(25:35)  
    stop  
endif
```

c Oper. Landmask file

```
mfile = drive//' :TOOLS://grdtyp//'MASK.DAT;1'  
print *, 'mask file = ',mfile  
munit = 18  
open (unit=munit,file=mfile, access='sequential',  
+ form='unformatted',recl=idim2,status='old')
```

c Get ice algorithm coefficients derived from tiepoints

```
call usetie (c,ihem)
```

c----- start ice concentration algorithm

```
do 1000 lp=1,idim3
```

c Swap bytes in buffer file for Apple Macintosh

```
do 800 inb=1,npar  
    read(iunit) bbyte  
  
    atemp(2)=btemp(1)  
    atemp(1)=btemp(2)  
  
    buff(inb)=abyte
```

800 continue

```
read(munit)(mask(ir.m),inm=1,idim2)
```

c Average TB₀ into 25 km cells and determine ice concentrations

```
call ice25 (buff,c,maxlcn,idim1,idim2,ice,mask,icepar)
```

c Write grid line of ice concentrations to file.

```
write(ounit)(ice(iout),iout=1,idim2)
```

1000 continue

c----- end ice algorithm

close (unit=munit)

close (unit=iunit)

close (unit=ounit)

close (unit=29)

5000 continue

6000 end

```

      program locate
cccccccccccccccccccccccccccccccccccccccccccccccccccccccccccccccccccc
c
c LOCATE : This program transforms I,J coordinates of an SSM/I grid cell
c         to latitude and longitude coordinates. This program provides
c         the inverse functions as well. LOCATE interfaces to the revised
c         forms of the subroutines, MAPXY and MAPLL.
c
c User-defined Parameters:
c
c  gtype  : Integer supplied by the user to describe one of the three
c          grid cell dimensions (12.5 km, 25.0 km, or 50.0 km).
c
c  ihem   : Integer supplied by the user to describe one of the two
c          polar regions (1=North , 2=South)
c
c  itrans : Integer supplied by the user to describe the type of
c          transformation LOCATE will perform (1=I,J-to-Lat,Lon;
c          2=Lat,Lon-to-I,J)
c
c  i,j    : Integers supplied by the user when itrans = 1. These
c          integers describe the position of a cell in an SSM/I grid.
c
c  lat,lon : Reals supplied by the user when itrans = 2. These
c          integers describe the latitude and longitude in an SSM/I
c          grid which LOCATE will transform to an I,J grid cell position.
c          Note: All latitudes and longitudes must be entered as
c          positive numbers!
c
c Internal:
c
c  x,y    : Distance in kilometers from the origin of the grid
c          (ie., pole).
c
c  alat,
c  alon   : Computed latitude and longitude returned from MAPXY.
c
c  SIGN   : Sign of the latitude (positive = north latitude,
c          negative = south latitude)
c
c  delta  : Meridian offset for the SSM/I grids (0 degrees for
c          the South Polar grids; 45 degrees for the North Polar
c          grids.
c
c  kk     : Integer variable used for reorientation of the grid. The
c          grid is 'flipped' in the Y direction for transformations.
c
c  SLAT   : Standard latitude for the SSM/I grids is 70 degrees.
c
c  numy   : Number of lines in an SSM/I grid. This attribute varies
c          for each of the six grids.

```



```

c
c cell : Size of the SSM/I grid ( 12.5 km, 25.0 km, 50.0 km)
c
c xydist : Distance from the origin of the grid in the cartesian plane.
c           The x-y coordinates for the edge of the lower left pixel
c           is (3850.0, 5350.0) for the northern grids and
c           (3950.0, 3950.0) for the southern grids.
c
c RE : Radius of the earth in kilometers.
c
c E : Eccentricity of the Hughes ellipsoid
c
c E2 : Eccentricity squared
c
c PI : Pi
c           Written by V.J.Troisi - January, 1990
c           Modified by W.A. Wright - July, 1991
cccccccccccccccccccccccccccccccccccccccccccccccccccccccccccccccc

```

```

real SLAT,E,RE,PI
real alat,alon,x,y
integer ihem
real lat, lon
real SGN, delta
integer numy(2,3)
real cell(3), xydist(2,2)
data numy / 896, 664, 448, 332, 224, 166 /
data cell / 12.5 , 25.0 , 50.0 /
data xydist / 3850.0 , 5350.0 , 3950.0 , 3950 /

```

```

SLAT = 70.
RE = 6378.273
E2 = .006693883
PI = 3.141592654
E = sqrt(E2)

```

```

c
c Query for the SSM/I grid cell size.
c

```

```

print *, 'Enter the grid cell dimension:'
print *, ' 1. 12.5 Km'
print *, ' 2. 25.0 Km'
print *, ' 3. 50.0 Km'
read *, gtype

```

```

c
c Query for polar region of interest.
c

```

```

print *, 'Enter the hemisphere of interest:'
print *, ' 1. North'
print *, ' 2. South'
read *, ihem

```

```

c
c Define the sign and meridian offset (delta) for the SSM/I grids.
c
    if (ihem.eq.1) then
        SGN = 1.0
        delta = 45.
    else
        SGN = -1.0
        delta = 0.0
    endif
c
c Query for translation type.
c
    print *, 'Enter one of the following transform functions:'
    print *, ' 1. Convert I,J to Latitude, Longitude'
    print *, ' 2. Convert Latitude, Longitude to I,J'
    read *, itrans
c
c Start translation
c
    if (itrans.eq.1) then
c
c Obtain the I,J position of the grid cell to transform to Latitude
c and Longitude
c
        print *, 'Enter i,j:'
        read *, i,j
c
c Convert I,J pairs to x and y distances from origin. The grid will be
c 'flipped' in the 'Y' direction.
c
        x=((i-1)*cell(gtype))-(xydist(1,ihem)-cell(gtype)/2.)
        kk=numy(ihem,gtype)-(j-1)
        y=((kk-1)*cell(gtype))-(xydist(2,ihem)-cell(gtype)/2.)
c
c Transform x and y distances to latitude and longitude
c
        call mapxy (x,y,alat,alon,SLAT,SGN,E,RE)
c
c Transform radians to degrees.
c
        alon=alon*180./PI
        alat=alat*180./PI
        alon=alon-delta
c
c Convert longitude to positive degrees
c
        if (alon.le.0.0) alon=alon+360.
        if (alon.ge.360.0) alon=alon-360.

```

```

c Print the latitude and longitude for the center of the I,J cell.
c
    print *,alat,alon
    pause
else
c
c Obtain the latitude and longitude pair and transform to cell where
c that pair is located.
c
    print *, 'Enter latitude and longitude (positive values):'
    read *,lat,lon
c
c Transform degrees to radians
c
    alat=abs(lat)*PI/180.
    alon=(lon+delta)*PI/180.
c
c Transform latitude and longitude to x and y distances from origin
c
    call mapll (x,y,alat,alon,SLAT,SGN,E,RE)
c
c Convert x and y distances from origin to I,J pair (ii,jj)
c
    ii=nint((x+xydist(1,ihem)-cell(gtype)/2.)/cell(gtype))+1
    jj=nint((y+xydist(2,ihem)-cell(gtype)/2.)/cell(gtype))+1
c
c Flip grid orientation in the 'Y' direction
c
    kk=numy(ihem,gtype)-(jj-1)
c
c Print the I,J location of the cell.
c
    print *,ii,kk
    pause

endif
end
SUBROUTINE MAPLL (X,Y,ALAT,ALONG,SLAT,SGN,E,RE)
CS*****
CS
CS
CS DESCRIPTION:
CS
CS This subroutine converts from geodetic latitude and longitude to Polar
CS Stereographic (X,Y) coordinates for the polar regions. The equations
CS are from Snyder, J. P., 1982, Map Projections Used by the U.S.
CS Geological Survey, Geological Survey Bulletin 1532, U.S. Government
CS Printing Office. See JPL Technical Memorandum 3349-85-101 for further
CS details.
CS
CS

```

```

CS  ARGUMENTS:
CS
CS  Variable  Type    I/O  Description
CS
CS  ALAT    REAL*4    I    Geodetic Latitude (degrees, +90 to -90)
CS  ALONG   REAL*4    I    Geodetic Longitude (degrees, 0 to 360)
CS  X       REAL*4    O    Polar Stereographic X Coordinate (km)
CS  Y       REAL*4    O    Polar Stereographic Y Coordinate (km)
CS
CS
CS      Written by C. S. Morris - April 29, 1985
CS      Revised by C. S. Morris - December 11, 1985
CS
CS      Revised by V. J. Troisi - January 1990
CS      SGN - provides hemisphere dependency (+/- 1)
CS*****
REAL*4 X,Y,ALAT,ALONG,E,E2,CDR,PI,SLAT,MC
CS*****
CS
CS  DEFINITION OF CONSTANTS:
CS
CS  Conversion constant from degrees to radians = 57.29577951.
    CDR=57.29577951
    E2=E*E
CS  Pi=3.141592654.
    PI=3.141592654
CS
CS*****
C    Compute X and Y in grid coordinates.
    IF (ABS(ALAT).LT.PI/2.) GOTO 250
    X=0.0
    Y=0.0
    GOTO 999
250 CONTINUE
    T=TAN(PI/4.-ALAT/2.)/((1.-E*SIN(ALAT))/(1.+E*SIN(ALAT)))** (E/2.)
    IF (ABS(90.-SLAT).LT.1.E-5) THEN
      RHO=2.*RE*T/((1.+E)**(1.+E)*(1.-E)**(1.-E))** (E/2.)
    ELSE
      SL=SLAT*PI/180.
      TC=TAN(PI/4.-SL/2.)/((1.-E*SIN(SL))/(1.+E*SIN(SL)))** (E/2.)
      MC=COS(SL)/SQRT(1.0-E2*(SIN(SL)**2))
      RHO=RE*MC*T/TC
    END IF
    Y=-RHO*SGN*COS(SGN*ALONG)
    X= RHO*SGN*SIN(SGN*ALONG)
999 CONTINUE
    END

```

```

SUBROUTINE MAPXY (X,Y,ALAT,ALONG,SLAT,SGN,E,RE)
C$*****
C$
C$
C$ DESCRIPTION:
C$
C$ This subroutine converts from Polar Stereographic (X,Y) coordinates
C$ to geodetic latitude and longitude for the polar regions. The equations
C$ are from Snyder, J. P., 1982, Map Projections Used by the U.S.
C$ Geological Survey, Geological Survey Bulletin 1532, U.S. Government
C$ Printing Office. See JPL Technical Memorandum 3349-85-101 for further
C$ details.
C$
C$
C$ ARGUMENTS:
C$
C$ Variable   Type      I/O  Description
C$
C$ X          REAL*4     I    Polar Stereographic X Coordinate (km)
C$ Y          REAL*4     I    Polar Stereographic Y Coordinate (km)
C$ ALAT       REAL*4     O    Geodetic Latitude (degrees, +90 to -90)
C$ ALONG      REAL*4     O    Geodetic Longitude (degrees, 0 to 360)
C$
C$
C$           Written by C. S. Morris - April 29, 1985
C$           Revised by C. S. Morris - December 11, 1985
C$
C$           Revised by V. J. Troisi - January 1990
C$           SGN - provide hemisphere dependency (+/- 1)
C$
C$*****
REAL*4 X,Y,ALAT,ALONG,E,E2,CDR,PI
C$*****
C$
C$ DEFINITION OF CONSTANTS:
C$
C$ Conversion constant from degrees to radians = 57.29577951.
C$   CDR=57.29577951
C$   E2=E*E
C$   Pi=3.141592654.
C$   PI=3.141592654
C$
C$*****
SL = SLAT*PI/180.
200 RHO=SQRT(X**2+Y**2)
   IF (RHO.GT.0.1) GOTO 250
   ALAT=90.*SGN
   ALONG=0.0
   GOTO 999
250 CM=COS(SL)/SQRT(1.0-E2*(SIN(SL)**2))

```

```

T=TAN((PI/4.0)-(SL/(2.0)))/((1.0-E*SIN(SL))/
C(1.0+E*SIN(SL)))** (E/2.0)
IF (ABS(SLAT-90.).LT.1.E-5) THEN
T=RHO*SQRT((1.+E)**(1.+E)*(1.-E)**(1.-E))/2./RE
ELSE
T=RHO*T/(RE*CM)
END IF
CHI=(PI/2.0)-2.0*ATAN(T)
ALAT=CHI+((E2/2.0)+(5.0*E2**2.0/24.0)+(E2**3.0/12.0))*SIN(2*CHI)+
C((7.0*E2**2.0/48.0)+(29.0*E2**3/240.0))*SIN(4.0*CHI)+
C(7.0*E2**3.0/120.0)*SIN(6.0*CHI)
ALAT=SGN*ALAT
ALONG=ATAN2(SGN*X,-SGN*Y)
ALONG=SGN*ALONG
999 CONTINUE
END

```

program u, v calc

```
*****
*
*   This program calculates the u and v components of motion from a list of
*   user specified geodetic latitude and longitude postions. Results are output
*   as an ASCII data file in units of cm/s. Appropriate lines in code must be
*   modified to specify the filepath of input and output files.
*
*   Variables: fname - input file name
*               infile - input file path
*               ofile - output file path
*               lat,lon - latitude and longitude expressed as real numbers
*               mlat - mean latitude between two positions
*               u, v - u and v components of motion
*               day - day of position (integer)
*               length - length in days of series
*               tmpd - time between postions (in days)
*
*****
```

```
character*10 fname
character*70 ofile, infile
real lat(60), lon(60), u(60), v(60), mlat
integer day(60), length, tmpd
```

c Construct input file path and open

```
5  print *, 'Enter input file name'
   read (*, '(a)') fname

   print *, 'Enter number of days in series'
   read *, length

   print *, 'Enter separation time period (days)'
   read *, tmpd

   infile='Archs HardDisk:THESIS:Position Data: '//fname
   open (unit=15, file=infile, status='old', iostat=ier)
   if (ier.ne.0) then
       print *, infile, 'not accessible! <ret>'
       pause
       stop
   endif
```

c Construct output file path and open

```
   ofile='Archs HardDisk:THESIS:Position Data: '//fname//'.uv'
   open (unit=18, file=ofile, status='new', form='formatted',
+       iostat=ier)
   if (ier.ne.0) then
```

```

        print*, 'Error opening ', ofile, ' <ret>'
        pause
        stop
    endif

c Read in data

    read (15,10) (day(i), lat(i), lon(i), i=1,length)

c Compute u, v components (km/time period)

    do 100 i=1, length-1

        v(i) = (lat(i+1) - lat(i)) * 111.6114

        mlat = (lat(i) + lat(i+1))/2.

        call gcircl(mlat,lon(i),mlat,lon(i+1),u(i))
        if (lat(i+1) .lt. lat(i)) u(i) = -u(i)
        print*, u(i), v(i)

100    continue
        pause

c Convert u, v components to cm/s

    do 200 i=1, length-1

        u(i) = u(i) * (1./tmpd)*(1000.)*(100.)*(1./24.)*(1./3600.)
        v(i) = v(i) * (1./tmpd)*(1000.)*(100.)*(1./24.)*(1./3600.)

200    continue

c Write to file

    write (18,20) 'u', 'v'
    write (18,20) 'cm/s', 'cm/s'
    write (18,30) (u(i), v(i), i=1,length-1)

10    format (i6,3x,f5.2,2x,f6.2)
20    format (1x, a,',',3x,a)
30    format (1x, f6.2,',',3x,f6.2)

    end

```

```
subroutine gcircl(lat1,lon1,lat2,lon2,gcircl)
```

c This program computes great circle distance.

c Inputs are latitude/longitude pairs in decimal degrees.

c Output is circumferential distance between the points in kilometers.

```
implicit real*8 (a-z)
```

```
real*8 dpr
```

```
real*4 lat1, lon1, lat2, lon2, gcircl
```

```
integer again
```

```
dpr = 57.29577951308232
```

c Compute difference in longitudes

```
t = (lon2 - lon1) / dpr
```

c Compute r

```
dsinr = dsin(t) * dcos(lat2/dpr)
```

```
r = dasin(dsinr)
```

c Compute k

```
dsink = dsin(lat2 / dpr) / dcos(r)
```

```
k = dasin(dsink)
```

c Compute angle D

```
dcosd = dcos(r) * dcos(k - (lat1 / dpr))
```

```
d = dacos(dcosd) * dpr
```

c Compute distance based on 111.6114 km/deg

```
gcircl = d * 111.6114
```

```
return
```

```
end
```

```

      subroutine usetie ( c , ihem )
cccccccccccccccccccccccccccccccccccccccccccccccccccccccccccccccccccc
c
c  USETIE - This subroutine computes coefficients for the ice algorithm
c           using the NASA-approved tiepoints.
c
c  Inputs
c
c     c   : Real array of coefficients. Refer to NODS User
c           handbook for description of coefficients A-L.
c
c     ihem : Integer denoting hemisphere (1=north, 2=south). Used
c            in determining which set of coefficients to use.
c
c
c  Internals
c
c     TB...W: Open water tiepoints. One for each of the three channels
c            used in the ice concentration algorithm (19V, 19H, 37V)
c
c     TB...F: Firstyear tiepoints. One for each of the three channels
c            used in the ice concentration algorithm (19V, 19H, 37V)
c
c     TB...M: Multiyear tiepoints. One for each of the three channels
c            used in the ice concentration algorithm (19V, 19H, 37V)
c
c     DW   : Difference between component tiepoints for open water.
c
c     SW   : Sum of the component tiepoints for open water.
c
c     DF   : Difference between component tiepoints for first year ice.
c
c     SF   : Sum of the component tiepoints for first year ice.
c
c     DM   : Difference between component tiepoints for multiyear ice.
c
c     SM   : Sum of the component tiepoints for multiyear ice.
c
c  Outputs
c
c     c   : Array of coefficients which have been computed from
c           tiepoints.
cccccccccccccccccccccccccccccccccccccccccccccccccccccccccccccccccccc

```

```

      real c(12)
      integer ihem

```

c Tiepoints for open water, first-year ice and multi-year ice
 c The first element of each tiepoint array represents the tiepoints
 c for the North Polar region; the second element is applied to the
 c South Polar region.

c declare the two-element open water tiepoints

real TB19VW(2), TB19HW(2), TB37VW(2)

c declare the two-element first-year tiepoints

real TB19VF(2), TB19HF(2), TB37VF(2)

c declare the two-element multi-year tiepoints

real TB19VM(2), TB19HM(2), TB37VM(2)

real DW(2) , DF(2) , DM(2)

real SW(2) , SF(2) , SM(2)

c First component of each tiepoint pair is for Northern Hemisphere
 c Second component of each tiepoint pair is of Southern Hemisphere
 c These tiepoints approved for use by the NASA Sea Ice Algorithm
 c Working Group (1/90)

data TB19VW / 175.3, 175.3/

data TB19HW / 97.7, 97.7/

data TB19VF / 254.0, 251.2/

data TB19HF / 236.0, 241.7/

data TB19VM / 223.2, 223.2/

data TB19HM / 203.9, 203.9/

data TB37VW / 199.6, 199.6/

data TB37VF / 250.0, 248.3/

data TB37VM / 186.3, 186.3/

DW(1) = TB19VW(ihem) - TB19HW(ihem)

DF(1) = TB19VF(ihem) - TB19HF(ihem)

DM(1) = TB19VM(ihem) - TB19HM(ihem)

SW(1) = TB19VW(ihem) + TB19HW(ihem)

SF(1) = TB19VF(ihem) + TB19HF(ihem)

SM(1) = TB19VM(ihem) + TB19HM(ihem)

DW(2) = TB37VW(ihem) - TB19VW(ihem)

DF(2) = TB37VF(ihem) - TB19VF(ihem)

DM(2) = TB37VM(ihem) - TB19VM(ihem)

SW(2) = TB37VW(ihem) + TB19VW(ihem)

$SF(2) = TB37VF(ihem) + TB19VF(ihem)$
 $SM(2) = TB37VM(ihem) + TB19VM(ihem)$

c Derive coefficients from tiepoints

$c(1) = DM(1)*DW(2) - DM(2)*DW(1)$
 $c(2) = DM(2)*SW(1) - DW(2)*SM(1)$
 $c(3) = DW(1)*SM(2) - DM(1)*SW(2)$
 $c(4) = SM(1)*SW(2) - SM(2)*SW(1)$
 $c(5) = DF(1)*(DM(2) - DW(2)) + DW(1)*(DF(2) - DM(2))$
 $1+ DM(1)*(DW(2) - DF(2))$
 $c(6) = DF(2)*(SM(1) - SW(1)) + DW(2)*(SF(1) - SM(1))$
 $1+ DM(2)*(SW(1) - SF(1))$
 $c(7) = DF(1)*(SW(2) - SM(2)) + DW(1)*(SM(2) - SF(2))$
 $1+ DM(1)*(SF(2) - SW(2))$
 $c(8) = SF(2)*(SW(1) - SF(1)) + SW(2)*(SM(1) - SF(1))$
 $1+ SM(2)*(SF(1) - SW(1))$
 $c(9) = DF(2)*DW(1) - DF(1)*DW(2)$
 $c(10) = DW(2)*SF(1) - DF(2)*SW(1)$
 $c(11) = DW(2)*DF(1) - DW(1)*SF(2)$
 $c(12) = SF(2)*SW(1) - SF(1)*SW(2)$

return
end

```

      subroutine ice25 ( tb,c,maxlen,idim1,idim2,ice,mask,icepar )
cccccccccccccccccccccccccccccccccccccccccccccccccccccccccccccccc
c ICE25 - Compute ice concentrations from NSIDC CD-ROM data at 25 km
c   resolution.
c
c   Software is modified from the Vince Troisi's original 50 km version by
c   W. A. Wright, Naval Postgraduate School.
c
c Algorithm
c
c   The ice concentration algorithm is an adaptation of the
c   algorithm designed by the NODS Software Group (refer to the
c   NODS User Handbook, Appendix CC, pp 22-26). The algorithm
c   uses the latest SSM/I tiepoints which were determined by Don
c   Cavalieri and Koni Steffen.
c
c   A weather filter (GR > .05) is applied to correct for false
c   concentrations computed in regions of open water.
c
c   Computed concentrations greater than 120% and less than -20%
c   are considered suspect and the corresponding cell is flagged
c   as missing (-99).
c
c Inputs
c
c   tb   : buffer of TB cell values. This buffer includes all
c         SSM/I TB parameters excluding the 85GHz channels.
c
c   idim1 : The number of parameters in a SSM/I cell (ie., 5)
c
c   idim2 : The number of cells in a SSM/I Tb grid line.
c
c   maxlen: The maximum length of tb
c
c   mask  : A line from the landmask for 25 km grid. The mask
c           line corresponds to the ice grid line to be
c           computed. (1=land; 0=water)
c
c   icepar: The ice concentration type to compute (1=total,
c           2=multiyear)
c
c Internals
c
c   c    : Array of coefficients used to compute ice concentrations.
c         Refer to NODS Handbook Volume II. Appendix CC pp 23-24.
c
c   ioff : Offset pointers used to point to Tb values used in
c         this ice algorithm (19GHz V, 19GHz H, 37GHz V).
c
c   ipos : position in tb array which is to be summed

```

```

c
c      sum  : Real register used for summing four adjacent Tb values
c
c      count : The number of Tb values not flagged as missing. A Tb value
c              of zero (0) is a missing Tb value.
c
c      fyr  : Integer register which stores the calculated first-year
c              ice concentration
c
c      myr  : Integer register which stores the calculated multi-year
c              ice concentration
c
c      tot  : Integer register which stores the calculated total ice
c              concentration
c
c      fyrb : Two - byte buffer equivalenced to fyr register. Only the
c              first byte is the significant part of the register.
c
c      myrb : Two - byte buffer equivalenced to myr register. Only the
c              first byte is the significant part of the register.
c
c      GR   : Gradient ratio
c
c      PR   : Polarization ratio
c
c  Outputs
c
c      ice  : Line of 25 km ice concentration grid. Values are
c              represented as a single byte percentage ranging
c              from 0 - 100%. Cells over land flagged with -88;
c              cells for which concentrations were suspect or
c              not computed are flagged with -99.
c
c  ccccccccccccccccccccccccccccccccccccccccccccccccccccccccccccccc
c
c      integer idim1,idim2
c      integer maxlen
c      integer*2 tb(maxlen*idim1)
c
c  c Offset from start of cell to three parameters used in ice
c  c calculations for two lines of data
c
c      integer*2 ioff(3)
c
c      integer*2 fyr,myr,tot
c      integer*1 fyrb(2),myrb(2)
c      integer*1 ice(idim2),mask(idim2),fyrice,myrice
c
c      logical GOOD
c
c  c Three TB parameters for ice concentrations

```

```

real    BT19V,BT19H,BT37V
real    c(12)
real    GR,PR,PRGR
real    ANF,ANM,DD

equivalence (fyr, fyrb(1))
equivalence (myr, myrb(1))

c Offset pointers for Brightness temperature cells used in algorithm

data ioff /0,1,3/

c Begin processing buffer

ii = 0
do 1000 i = 1, idim1*idim2, idim1

c Increment pointer for next Ice cell.

ii=ii+1

c Calculate Ice Concentration

GOOD = .true.

c Set ice pixel to land(-88) if over land

if (mask(ii).eq.1) then
    ice(ii)=-88
else

c Determine Ice Concentration of the ice pixel

do 80 l=1,3

    ipos=i+ioff(l)

    tbval = (float(tb(ipos)))/10.

    if(l.eq.1) BT19V = tbval
    if(l.eq.2) BT19H = tbval
    if(l.eq.3) BT37V = tbval
80    continue

```

c Set ice cell to missing if any TB parameters are missing

```
      if (BT19V.EQ.0.0 .or. BT19H.EQ.0.0 .or.  
*      BT37V.EQ.0.0 ) then  
        fyrice = -99  
        myrice = -99  
        ice(ii) = -99  
      else
```

c Compute open water weather filter

$$GR = (BT37V - BT19V)/(BT37V + BT19V)$$

c.....
c Set ice cell to 0% concentration if weather filter > .05
c Filter value of 0.05 may be altered at a future date!

```
c.....  
      if (GR .gt. .05) then  
        fyrice = 0  
        myrice = 0  
        ice(ii) = 0  
      else
```

c Apply noniterative ice algorithm

c Compute polarization ration PR

$$\begin{aligned} PR &= (BT19V - BT19H)/(BT19V + BT19H) \\ PRGR &= PR*GR \\ ANF &= c(1) + c(2)*PR + c(3)*GR + c(4)*PRGR \\ ANM &= c(9) + c(10)*PR + c(11)*GR + c(12)*PRGR \\ DD &= c(5) + c(6)*PR + c(7)*GR + c(8)*PRGR \end{aligned}$$

c Compute First-Year, Multi-Year, and Total Ice Concentrations

$$\begin{aligned} fyr &= ifix(100.0*(ANF/DD)) \\ myr &= ifix(100.0*(ANM/DD)) \\ tot &= fyr + myr \end{aligned}$$

c.....
c Filter out values outside the range of -20 to 120
c This filter may be altered at a future date

```
c.....  
      if (fyr .lt. -20 .or.  
*      myr .lt. -20 .or.  
*      tot .lt. -20 .or.  
*      fyr .gt. 120 .or.  
*      myr .gt. 120 .or.  
*      tot .gt. 120) then  
        fyrice = -99  
        myrice = -99  
        ice(ii) = -99
```



```

        GOOD    = .false.
    endif

c Place concentration values into byte data representations

        if (GOOD) then
            fyrice = fyrb(2)
            myrice = myrb(2)
            if (icepar.eq.1) ice(ii) = fyrice + myrice
            if (icepar.eq.2) ice(ii) = myrice
c-----
c Set concentration to 0 if computed concentration between -20 and 0
c Set concentration to 100 if computed concentration between 100 and 120
c-----
            if (ice(ii) .lt. 0) ice(ii) = 0
            if (ice(ii) .gt. 100) ice(ii) = 100
        endif
        GOOD = .true.
    endif
endif
endif
1000 continue

c Return computed ice concentration array, ice

    return
end

```

REFERENCES

- Aagaard, K. and P. J. Greisman, Towards new mass and heat budgets for the Arctic Ocean, *J. Geophys. Res.*, 80, 3821-3827, 1975.
- Aagaard, K. and Carmack, E., The role of sea ice and other fresh water in the Arctic circulation, *J. Geophys. Res.*, 94, 14485-14490, 1989.
- Carsey, F. and B. Holt, Beaufort-Chukchi ice margin data from Seasat: ice motion, *J. Geophys. Res.*, 92, 7163-7172, 1987.
- Carsey, F. D. and H. J. Zwally, Remote sensing as a research tool, in *The Geophysics of Sea Ice*, edited by N. Untersteiner, pp. 1021-1097, Plenum Press, 1986.
- Cavalieri, D. J., P. Gloerson and W. J. Campbell, Determination of sea ice parameters with the NIMBUS 5 SMMR, *J. Geophys. Res.*, 89, 5355-5369, 1984.
- Chapman, D., Enhanced subinertial diurnal tides over isolated topographic features, *Deep-Sea Res.*, 36, 815-824, 1989.
- Colony, R. and A. S. Thorndike, An estimate of the mean field of arctic sea ice motion, *J. Geophys. Res.*, 89, 10623-10629, 1984.
- Colony, R. L. and I. Rigor, Arctic Buoy Program Data Report for 1 January 1988 - 31 December 1988, APL Techmemo, APL-UW TA8-91, 1990.
- Colony, R. L. and I. Rigor, Arctic Buoy Program Data Report for 1 January 1988 - 31 December 1989, APL Techmemo, APL-UW TM9-91, 1991.
- Comiso, J. C., J. J. Zwally and J. L. Saba, Radiative transfer modeling of microwave emission and dependence on firm properties, *Ann. Glaciol.*, 3, 54-58, 1982.
- Comiso, J. C., Sea ice effective microwave emissivities from satellite passive microwave and infrared observations, *J. Geophys. Res.*, 88, 7686-7704, 1983.
- Cousins, J. D., CEAREX ambient noise data measured northeast of Svalbard, Masters Thesis, Naval Postgraduate School, Monterey, Ca., 1991.

- Emery, W. J., C. W. Fowler, J. Hawkins and R. H. Preller, Fram Strait satellite image-derived ice motions, *J. Geophys. Res.*, **96**, 4751-4768, 1991.
- Gjevik, B. and T. Straume, Model simulations of the M2 and K1 tide in the Nordic Seas and Arctic Ocean, *Tellus*, **41A**, 73-96, 1989.
- Gloersen, P., W. Nordberg, T. J. Schmugge, T. T. Wilheit and W. J. Campbell, Microwave signatures of first-year and multiyear sea ice, *J. Geophys. Res.*, **78**, 3564-3572, 1973.
- Goroch, A. K. and R. Fett, Observations of flooded ice in arctic regions, unpublished manuscript, 1990.
- Hibler, W. D., Ice dynamics, in *The Geophysics of Sea Ice*, edited by N. Untersteiner, pp. 577-640, Plenum Press, 1986.
- Hoffman, P. J., Transpolar sea ice drift in the vicinity of the Yermak Plateau as observed by ARCTEMIZ 86 buoys, Master's Thesis, Naval Postgraduate School, Monterey, Ca., 1990.
- Hollinger, J. R. Lo, G. Poe, R. Savage, and J. Peirce, Special Sensor Microwave /Imager User's Guide, Naval Research Lab, 1987.
- Hollinger, J. P., J. L. Peirce and G. A. Poe, SSM/I Instrument Evaluation, *IEEE Trans. Geosci. Remote Sensing*, **28**, 781-790, 1990.
- Hollinger, J., *DMSP Special Sensor Microwave/Imager Calibration/Validation Vol. I*, Naval Research Lab, 1989.
- Hunkins, K., Anomalous diurnal tidal currents on the Yermak Plateau, *J. Mar. Res.*, **44**, 51-69, 1986.
- Kowlik, Z., A note on the co-oscillating M2-tide in the Arctic Ocean, *Dt. Hydrogr. Z.*, **32**, 100-112, 1979.
- Morison, J. H., M. G. McPhee and G. A. Maykut, Boundary layer, upper ocean, and ice observations in the Greenland Sea marginal ice zone, *J. Geophys. Res.*, **92**, 6987-7011, 1987.
- National Snow and Ice Data Center (NSIDC), DMSP SSM/I Brightness Temperature Grids for the Polar Regions on CD-ROM User's Guide, Univ. of Colorado, Boulder, 1990.
- Ninnis, R.M., W. J. Emery and M. J. Collins, Automated extraction of pack ice motion from Advanced Very High Resolution Radiometer imagery, *J. Geophys. Res.*, **91**, 10725-10734, 1986.

- Norris, C. L. and W. J. Emery, *Imagic User's Guide* (draft), Univ. of Colorado, Boulder, 1989.
- Padman, L. and T. M. Dillon, Turbulent mixing near the Yermak Plateau during CEAREX, *J. Geophys. Res.*, *in press*, 1991.
- Parkinson, C. L., J. C. Comiso, H. J. Zwally D. J. Cavalieri, P. Gloerson, and W. J. Campbell, *Arctic Sea Ice, 1973-1976: Satellite Passive Microwave Observations*, NASA SP-489, 1987.
- Parkinson, C. L., and D. J. Cavalieri, Arctic sea ice 1973-1987: seasonal, regional and interannual variability, *J. Geophys. Res.*, *94*, 14499-14523, 1989.
- Perry, R. K., Bathymetry, in *The Nordic Seas*, edited by B. Hurdle, p 219, Springer-Verlag, 1986.
- Poe, G. A., and R. W. Conway, A study of the geolocation errors of the Special Sensor Microwave/Imager (SSM/I), *IEEE Trans. Geosci, Remote Sensing*, *28*, 791-799, 1990.
- Polarstern Scientific Party, Breakthrough in arctic deep-sea research: The R/V Polarstern expedition 1987, *EOS Trans.*, *69*, 665-678, 1988.
- Prazuck, C., Anomalous diurnal currents in the vicinity of the Yermak Plateau, Ph. D. dissertation, Naval Postgraduate School, Monterey, Ca., 1991.
- Schwiderski, E. W., Tides, in *The Nordic Seas*, edited by B. Hurdle, pp. 199-204, Springer-Verlag, 1986.
- Svendsen, E., D. Kloster, B. Farelly, O. M. Johannessen, J. A. Johanessen, W. J. Campbell, P. Gloerson, D. Cavalieri, and C. Mätzler, Norwegian remote sensing experiment: evaluation of the Nimbus 7 Scanning Multichannel Microwave Radiometer for sea ice research, *J. Geophys. Res.*, *88*, 2781-2791, 1983.
- Taylor, P., Loss of SSM/I 85H Data, *CDMS Notes*, *7*, 1990.
- Thorndike, A. S., Kinematics of sea ice, in *The Geophysics of Sea Ice*, edited by N. Untersteiner, pp. 489-549, Plenum Press, 1986.
- Thorndike, A. S. and R. Colony, Arctic Buoy Program Data Report 19 January 1979 - 31 December 1979, Polar Science Center, Univ. of Wash., 1980.
- Vant, M. R., R. O. Ramseier and V. Makios, The complex-dielectric constant of sea ice at frequencies in the range of 0.1-40 GHz, *J. Appl. Phys.*, *49*, 1264-1280, 1978.

Vinje, T. and O. Finnekasa, The Ice Transport through the Fram Strait, *Norsk Polarinstitutt, No. 186*, Oslo, 39pp., 1986.

Weeks, W. F., Sea ice: the potential of remote sensing, *Oceanus*, 24, 39-48, 1981.

Zhang, H., Parameter retrieval algorithms and data analysis system for sea ice remote sensing, *Em. Inst. Tech. U. of Denmark, LD 85*, 1991.

INITIAL DISTRIBUTION LIST

	No. Copies
1. Defense Technical Information Center Cameron Station Alexandria, VA 22304-6145	2
2. Library, Code 52 Naval Postgraduate School Monterey, CA 93943-5100	2
3. Library Scripps Institution of Oceanography University of California, San Diego La Jolla, CA 92093	1
4. Chairman (Code OC/CO) Department of Oceanography Naval Postgraduate School Monterey, CA 93943-5100	1
5. Jeffery A. Nystuen, Code OC/Ny Department of Oceanography Naval Postgraduate School Monterey, CA 93943-5100	1
6. Robert H. Bourke, Code OC/Bf Department of Oceanography Naval Postgraduate School Monterey, CA 93943-5100	1
7. Alan S. Thorndike, Code OC/To Department of Oceanography Naval Postgraduate School Monterey, CA 93943-5100	1
8. LCDR William A. Wright COMSUBLANTREP PSC 821, Box 111 FPO AE 09421-0111	1

- | | | |
|-----|--|---|
| 9. | Commanding Officer
Fleet Numerical Oceanography Center
Attn: A. Goroch
Monterey, CA 93943-5005 | 1 |
| 10. | National Snow and Ice Data Center
Attn: Claire Hansen
CIRES, Campus Box 449
University of Colorado
Boulder, CO 80309 | 1 |
| 11. | Jean-Claude Gascard
Univ. Paris 6
LODYC Tour 14-2C
4 Place Jussieu F-75252
Paris Cedex 05 FRANCE | 1 |
| 12. | Dr. Donald J. Cavalieri
NASA/Goddard SFC, Code 971
Greenbelt, MD 20771 | 1 |
| 13. | Commanding Officer
USCGC Mallow (WLB-396)
FPO San Francisco, CA 96672-3913 | 1 |